Stony Brook University

Spatial Characteristics of the Low-Latitude Atlantic Multidecadal Variability during the Past Millennium and Evaluation of CMIP5 Model Simulations

A Dissertation Presented

by

Tingyin Xiao

to

The Graduate School

in Partial Fulfillment of the

Requirements

for the Degree of

Doctor of Philosophy

in

Marine and Atmospheric Sciences

Stony Brook University

August 2016

Stony Brook University

The Graduate School

Tingyin Xiao

We, the dissertation committee for the above candidate for the

Doctor of Philosophy degree, hereby recommend

acceptance of this dissertation.

Minghua Zhang – Dissertation Advisor
Professor Dean, SoMAS

David Black - Chairperson of Defense
Associate Professor, SoMAS

Edmund Chang – Internal Committee Member
Professor, SoMAS

Hyemi Kim – Internal Committee Member
Assistant Professor, SoMAS

David McGee – External Committee Member
Assistant Professor, Department of Earth, Atmospheric and Planetary Sciences
Massachusetts Institute of Technology

This dissertation is accepted by the Graduate School

Nancy Goroff

Interim Dean of the Graduate School

Abstract of the Dissertation

Spatial Characteristics of the Low-Latitude Atlantic Multidecadal Variability during the Past Millennium and Evaluation of CMIP5 Model Simulations

by

Tingyin Xiao

Doctor of Philosophy

in

Marine and Atmospheric Sciences

Stony Brook University

2016

Atlantic multidecadal variability (AMV) influences climate of Atlantic coastal continents, including the Atlantic hurricanes, European summer rainfall, Sahelian precipitation, and African dust. Identifying corresponding climate proxies and integrating them with modern instrumental and reanalysis records are important to understand it in the context of future changes caused by human activities. In this study, we used the high-resolution and marine-based *Globigerina bulloides* abundance data from Cariaco Basin, the 20th Century reanalysis data, as well as other paleoclimate records to investigate the spatial pattern and coherence of the AMV. We then evaluated the ability of climate models in simulating the AMV.

From the analysis of modern instrument record, the variability of *G. bulloides* sediment abundance is found to have significant correlation with large-scale atmospheric and oceanic

conditions in the North Atlantic during the past century. Enhanced abundance of Cariaco Basin *G. bulloides* is associated with cooler North Atlantic sea surface temperature (SST), higher Azores High pressure, stronger tropical North Atlantic easterly trade winds, and less Intertropical Convergence Zone (ITCZ) rainfall in the African Sahel. We propose that the AMV influences the variation of zonal wind and *G. bulloides* abundance through Azores High pressure.

Consistent relationships are found from using different longer-term paleoclimate records at the multidecadal frequency. *Globigerina bulloides* sediment abundance is shown to negatively correlate with SST reconstruction at Eastern Tropical Atlantic and Puerto Rico at the same timescales, and positively correlate with a proxy of the multidecadal variabilities of the North Atlantic Oscillation (NAO). These results support that AMV exists prior to industrialization and its spatial pattern and coherence were similar in the pre-industry period to that in the 20th century.

The ability of five CMIP5 (Coupled Model Intercomparison Project Phase 5) models in simulating the AMV are evaluated from their historical and past millennium simulations. It was found that two models can capture the AMV spatial pattern shown in the reanalysis data, and the MPI-ESM (Max Planck Institute Earth System Model) performs the best in modeling the North Atlantic sea surface temperature (SST) as well as the spatial pattern and coherence of the AMV.

I dedicate this dissertation to my grandfather, Ling Yi, who inspired me to do science when I was a little girl.

His integrity, extensive knowledge, and unbelievable life stories will always be in my memories.

Table of Contents

List of Figures

List of Tables

List of Abbreviations

AMO	Atlantic multidecadal oscillation
AMOC	Atlantic Meridional Overturning Circulation
AMS	Accelerator Mass Spectrometry
AMV	Atlantic Multidecadal Variability
BCC-CSM 1.1	Beijing Climate Center, Climate System Model, version 1.1
Ca	Calcium
CCSM4	Community Climate System Model, version 4
CMIP5	Coupled Model Intercomparison Project Phase 5
DJFM	December-January-February-March
ECMWF	European Centre for Medium-Range Weather Forecasts
EOF	Empirical Orthogonal Function
ERA-20C	ECMWF's atmospheric reanalysis of the 20th century
FGOALS-s2	Flexible Global Ocean-Atmosphere-Land System Model, spectral version 2.0
G. bulloides	*Globigerina bulloides*
GPCC	Global Precipitation Climatology Centre
G. ruber	*Globigerinoides ruber*
ITCZ	Intertropical Convergence Zone
JAS	July-August-September
JFM	January-February-March
MSLP	mean sea level pressure
M. faveolata	*Montastraea faveolata*
Mg	Magnesium

MPI-ESM-MR	Max Planck Institute Earth System Model, Mixed-resolution version
MPI-ESM-P	Max Planck Institute Earth System Model, Paleo version
MRI-CGCM3	Meteorological Research Institute Coupled Atmosphere–Ocean General Circulation Model, version 3
NAO	North Atlantic Oscillation
NOAA	National Oceanic and Atmospheric Administration
NCAR	National Center for Atmospheric Research
PC	Principal Component
SLP	Sea Level Pressure
Sr	Strontium
SSS	Sea surface salinity
SST	Sea Surface Temperature
UCAR	University Corporation for Atmospheric Research

Acknowledgments

Firstly, I would like to express my greatest gratitude to my advisor Prof. Minghua Zhang, who has supported my Ph.D. study continuously and helped me in research, academic planning, and career development. I cannot thank him enough for his immense patience in building up my ability of independent thinking. Without his knowledge, instructions, or scientific insights, this thesis would not have been possible.

Besides my advisor, my sincere thanks also goes to the rest of my thesis committee: Prof. David Black, Prof. Edmund Chang, Prof. Hyemi Kim, and Prof. David McGee, for their valuable advice which helped enrich my research from many perspectives, and also for the hard questions which incented me to think deeper and improve the thesis accordingly. Their generous help is very greatly appreciated.

I would like to thank Prof. Edmund Change again, for his guidance and instructions when I was his Teaching Assistant. His highly careful and responsible attitude to the class and students is inspiring to me. I am also very grateful to Prof. Daniel Knopf, who taught me how to teach and encouraged me to get rid of the stage fright when I was the TA in his class. And my heart-felt thanks also goes to Prof. Marvin Geller, for all his encouragement when I was doing Teaching Practicum, as well as when I was taking his courses.

Assistance in the supercomputer and academic issues during my Ph.D. study provided by Dr. Ping Liu is greatly appreciated. And I would like to thank Dr. Wuyin Lin from Brookhaven

National Laboratory for his precious help when I had difficulties in my research. My deep appreciation also goes to Dr. Hao Chen from the Department of Applied Mathematics & Statistics for his professional assistance in the statistics methods applied in this thesis. I would also like to thank our group: Xin Xie, Jingyi Chen, Haiyang Yu, Xiaoxi Zhu, and Jia Wang, and the group members that have graduated: Dr. Jun Huang, Dr. Parama Mukherjee, and Dr. Shuaiqi Tang.

My special thanks are given to Carol Dovi for her incredible patience and efforts in helping me understand the rules and fulfill the requirements. I also want to thank Christina Fink, Steve Otega, and Gina Gartin for their assistance in many aspects. Without the helpful staffs, it would have been impossible for me to finish the study smoothly.

I am particularly grateful to Prof. Oleg Smirnov from the Department of Political Science, who gave me support and encouragement during all the time that I worked for him in the interdisciplinary study. I would like to thank him for his constant trust and understanding, and for his selfless help in my job searching process.

Finally, my deepest appreciation goes to my family for their unconditional love and support. I want to thank my parents for always having faith on me. And I wish to thank my husband and best friend, Ming-Tao Chuan, for his company and help throughout my study.

Vita

2010-2016	Ph.D. in Atmospheric Sciences, Stony Brook University, Stony Brook, NY, USA
2007-2010	M.S. in Meteorology, Institute of Atmospheric Physics, Chinese Academy of Sciences, Beijing, China
2003-2007	B.S. in Atmospheric Sciences, Nanjing University of Information Science and Technology, Nanjing, Jiangsu, China

Publications

Oleg Smirnov, Minghua Zhang, **Tingyin Xiao**, John Orbell, Amy Lobben, Josef Gordon 2016: The relative importance of climate change and population growth for exposure to future extreme droughts. *Climatic Change*, 1–13, doi:10.1007/s10584-016-1716-z.

Ridley, Harriet E., Yemane Asmerom, James U.L. Baldini, Sebastian F.M. Breitenbach, Valorie V. Aquino, Keith M. Prufer, Brendan J. Culleton, Victor Polyak, Fraziska A. Lechleitner, Douglas J. Kennett, Minghua Zhang, Norbert Marwan, Colin G. Macpherson, Lisa M. Baldini, **Tingyin Xiao**, Jaime Awe, and Gerald H. Haug, 2015: Aerosol forcing of intertropical convergence zone position. *Nature Geoscience* 8: 195-200.

Jiping Liu, **Tingyin Xiao**, and Liqi Chen, 2011: Intercomparisons of air–sea heat fluxes over the southern ocean. *J. Climate*, **24**, 1198–1211. doi: http://dx.doi.org/10.1175/2010JCLI3699.1

Chapter 1. Introduction

Variations in North Atlantic sea surface temperature (SST), the Intertropical Convergence Zone (ITCZ), Azores High, and easterly trade winds all play crucial roles in circum-Atlantic weather and climate [*Rodwell et al.*, 1999; *Enfield et al.*, 2001; *Zhang and Delworth*, 2006; *Yoon and Zeng*, 2010]. The behavior of such variations and their relationships with each other in the last several decades is relatively well-known, but modern meteorological records are still too short to understand low-frequency climate variability in the region on time scales of decades and longer.

The Atlantic Multidecadal Variability (AMV), also referred to as the Atlantic multidecadal oscillation (AMO), accounts for large variability in the North Atlantic Ocean SST [*Enfield et al.*, 2001; *Knight et al.*, 2005]. One of the most concerned questions about the low-frequency Atlantic climate variabilities is whether the AMO is really oscillatory in the pre-industrial era. And if yes, what is its spatial structure and what is its mechanism? Answering these questions can aid the future prediction of Atlantic coastal climate, including the Atlantic hurricanes, European summer rainfall, Sahelian precipitation, and African dust [*Sutton and Hodson*, 2005; *Knight et al.*, 2006; *Zhang and Delworth*, 2006; *Wang et al.*, 2012]. This study will primarily focus on answering the first question and examining the spatial characteristics.

Identifying corresponding climate proxies is important to understand the natural climate variability of the Atlantic region in the context of future changes caused by human activities. In

the previous studies, various kinds of paleoclimate proxies of North Atlantic climate were constructed. However, the paleoclimate data are still sparse in space. Furthermore, some of them do not have high enough time resolution, contain too large uncertainties, or do not have signals of multidecadal variabilities. There are more SST reconstructions than other variables, but most of which are terrestrial based or in the higher latitudes [*Delworth and Mann*, 2000; *Gray et al.*, 2004; *Miettinen et al.*, 2012]. High-resolution and marine based proxies in the tropical latitudes that envelop multidecadal signals are ideal to form a clearer picture of Atlantic multidecadal variability in the past.

The abundance of the planktic foraminifera *Globigerina bulloides* from sediment cores recovered from the Cariaco Basin (Venezuela) is one of the proxies that can provide information about North Atlantic paleoclimate variability [*Black et al.*, 1999]. Located at the northern extent of the annual mean ITCZ position over the tropical Atlantic, the Cariaco Basin (~10°N, 64°W) is an anoxic basin highly sensitive to regional climate variabilities (Fig. 1-1) [*Haug et al.*, 2003; *Tedesco et al.*, 2007]. Varved marine sediments with high deposition rates in the basin register the impact of meteorological and oceanic conditions that reflect Atlantic climate variability and change.

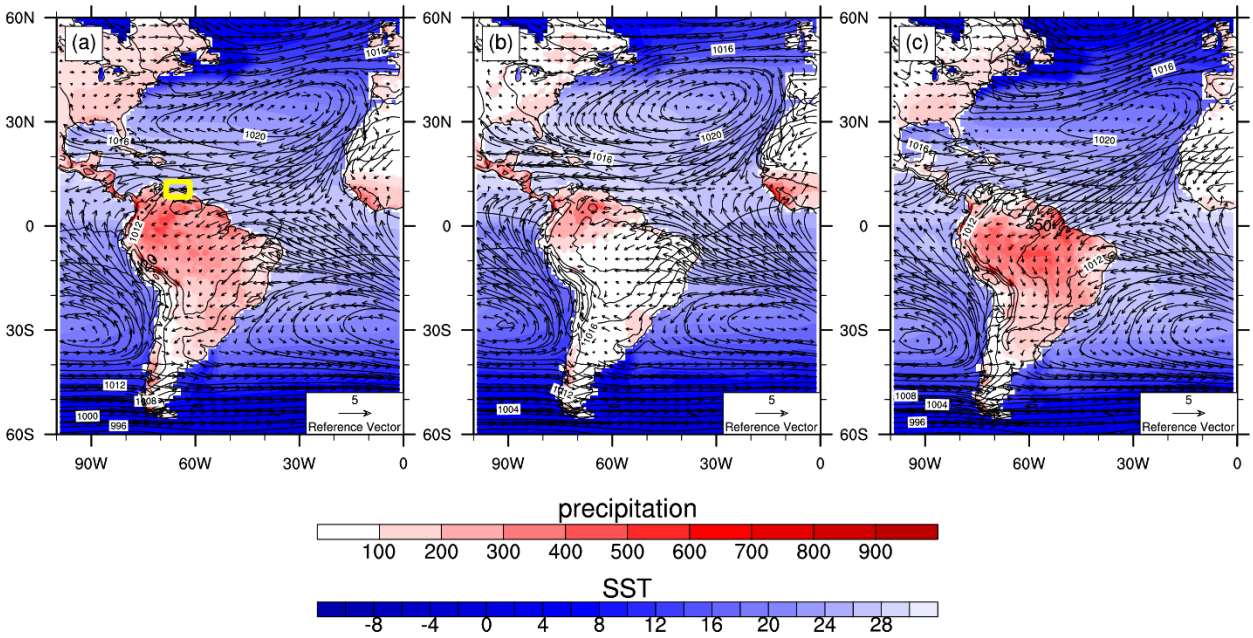

Figure 1-1. 1901-2010 (a) annual mean, (b) JAS mean, and (c) JFM mean SST (ocean color shade, °C), precipitation (land color shade, mm/month), mean sea level pressure (contours, hpa), and wind vector (vectors, m/s) over 60°S-60°N, 0°-100°W; Cariaco Basin approximate location denoted by yellow rectangular in (a). (Data description in Section 2.2., ERA-20C reanalysis SST, SLP, near-surface wind, and GPCC precipitation)

Previous studies have suggested that the *G. bulloides* abundance reflects the intensity of trade winds and upwelling as well as the movement of ITCZ [*Peterson et al.*, 1991; *Black et al.*, 1999]. However, due to limited availability of observational data, neither of these studies demonstrated the detailed spatial distribution of atmospheric circulation systems that are associated with variations in *G. bulloides* abundance.

In *Black et al.* [1999], an eight-century long *G. bulloides* abundance data is constructed and used to study the North Atlantic climate. Although the spectral analysis of *G. bulloides* abundance data does not indicate significant multidecadal variability, the comparisons between the proxy data and instrumental North Atlantic SST anomalies and interhemispheric SST

anomalies show concurrent multiple-decades-long positive and negative phases in the past 100-150 years, with large *G. bulloides* abundance corresponds to colder North Atlantic SSTs [*Black et al.,* 1999; Fig. 3].

This tropical marine proxy data has near annual time resolution with a tight age model. It also has a relatively long overlapping period with available modern observation and reanalysis data. These conditions make it ideal to be used together with the better documented modern data, which also has better spatial coverage. Using the paleoclimate and modern data together, we can find the spatial characteristics of the paleoclimate data associated climate variability in the instrumental data period, as well as the past variability of the modern-data-documented spatial pattern through the paleoclimate data. If this data is able to reflect multidecadal signals of SSTs, its past variation can add valuable information of how Atlantic SST evolved and interacted with other climate variables at this timescale in the past centuries. Moreover, establishing a detailed relationship between *G. bulloides* abundance and Atlantic low-frequency climate variability is also meaningful to other research fields, such as the ecosystem predictability involving this species [*Nye et al.,* 2014].

The first objective of this thesis research is to extend the results in *Black et al.* [1999] to investigate the spatial pattern and coherence of the AMV. We will first analyze the relationship between the *G. bulloides* sediment abundance data with large-scale atmospheric and oceanic climate variations in the North Atlantic by using atmospheric and oceanic observation and reanalysis data sets for the last century. We will then use other paleoclimate proxies and reconstructions of North Atlantic variables to examine whether available paleoclimate proxy data

display the same coherence on a much longer period to infer AMV before industrializations. In addition to the *G. bulloides* data, other proxies include North Atlantic SST proxies in the Eastern Atlantic and near Puerto Rico[*Kilbourne et al.*, 2008; *Kuhnert and Mulitza*, 2011], and two NAO (North Atlantic Oscillation) proxies [*Luterbacher*, 2002; *Goodkin et al.*, 2008a].

The second objective of this study is to evaluate the ability of the CMIP5 (Coupled Model Intercomparison Project Phase 5) models to simulate the spatial and temporal variation of the AMV. We will first examine the North Atlantic SST patterns and temporal variabilities in the past century simulation by using the 20th Century reanalysis data. We then use the proxy records to evaluate the AMV and its spatial coherence in the past 1000 year simulations.

The outline of this dissertation is as follows: In Chapter 2, the paleoclimate proxies, reanalysis data, and model simulation outputs used in this study are described. Then, the results are organized in three chapters. In Chapter 3, relationships between Cariaco Basin *G. bulloides* abundance data and several Atlantic climate variabilities are established based on observation and reanalysis data in the past century. These relationships and their spatial pattern serve as a basis for the consistency check of the paleoclimate data in Chapter 4. In Chapter 5, simulations from CMIP5 models are evaluated to examine whether the models can capture the AMV inferred from the 20th Century reanalysis and the paleoclimate data. This chapter also investigates which model has the best performance. Finally, the conclusion and discussion are given in Chapter 6.

Chapter 2. Description of the proxy, reanalysis, and model data

This chapter describes the proxy data, reanalysis data, and model simulation outputs used in this study.

2.1. Paleoclimate data

Paleoclimate proxy and reconstruction data used in the analysis includes Cariaco Basin *Globigerina bulloides* abundance data [*Black et al.*, 1999], an Eastern Tropical North Atlantic SST reconstruction [*Kuhnert and Mulitza*, 2011], Puerto Rico SST index [*Kilbourne et al.*, 2008], a Bermuda NAO reconstruction [*Goodkin et al.*, 2008a], and a statistical NAO reconstruction based on station data and paleoclimate proxies [*Luterbacher*, 2002]. In addition, the Cariaco Basin SST reconstructions [*Wurtzel et al.*, 2013] and Cariaco Basin sediment Titanium % rainfall proxy [*Haug et al.*, 2001; *Kennett et al.*, 2012a] are also discussed. The locations of data sources of each proxy data are denoted in Fig. 2-1.

These proxies carry information of essential aspects of Atlantic atmospheric and oceanic circulation. Before we apply them in the climate research, the construction methods and the uncertainties involved in their age model, measurement, and calculation are described and discussed.

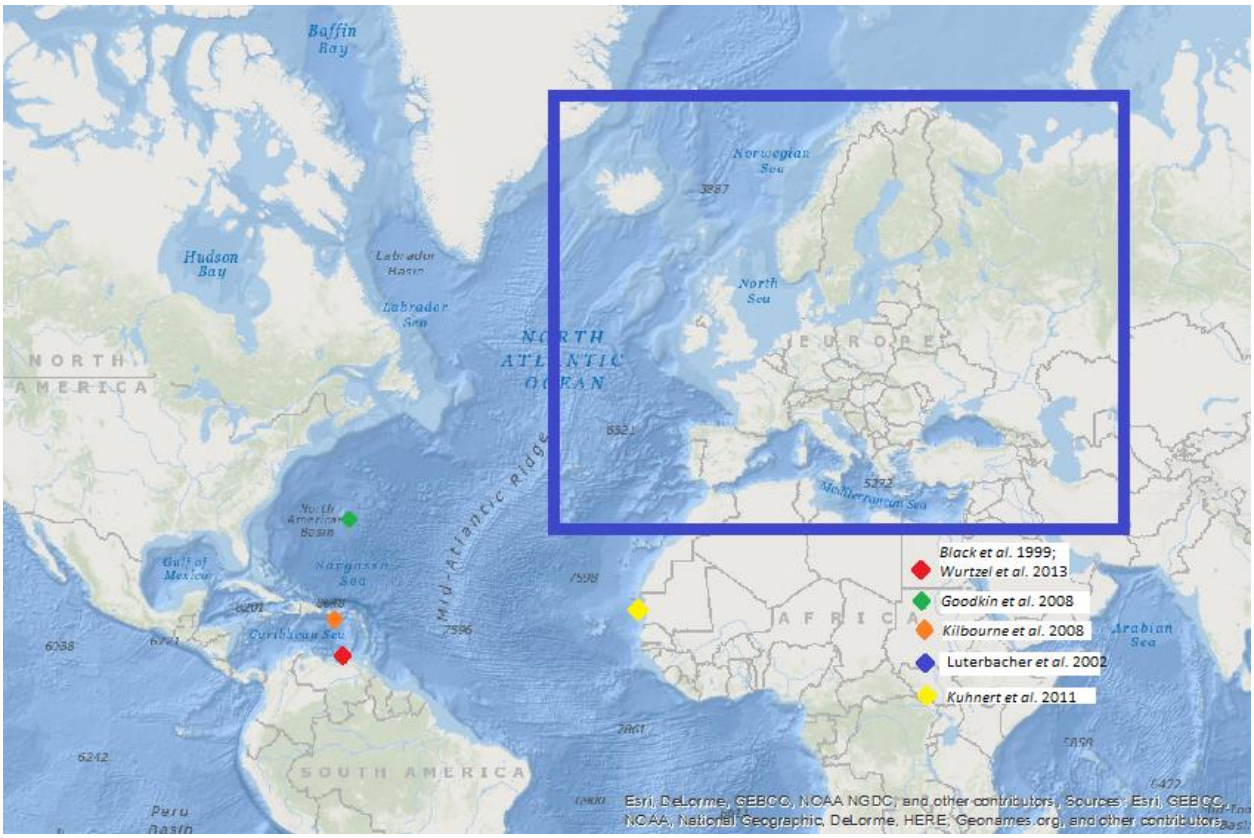

Figure 2-1. Distribution of paleoclimate data. Marine sediment data are shown with color diamonds; Luterbatcher et al. [2002] NAO index station and proxy data sites are in the range of the blue rectangular.

2.1.1. *Globigerina bulloides* abundance data

Globigerina bulloides is a planktic foraminifera species that lives in the upper part of the water column, and while typically a sub-polar species, is also commonly found in tropical and subtropical upwelling environments [*Peterson et al.*, 1991]. The abundance of *G. bulloides* in the Cariaco Basin is driven by food availability, which in turn is driven by local trade wind-induced upwelling and the fluvial delivery of nutrients [*Black et al.*, 1999; *Peterson et al.*, 2000].

Globigerina bulloides abundance proxy data (unit: number of *G. bulloides* per gram) is available for the interval spanning 1165 to 1990 C.E. [*Black et al.*, 1999; data are archived at the World Data Center for Paleoclimatology] (shown in Fig. 2-2). The proxy data is derived from sediments of box core PL07-71 BC (10°45.46' N, 64°41.68' W, 395 water depth) collected on the gentle northern slope of the eastern Cariaco Basin. The core had an intact and well-defined sediment-water interface upon recovery.

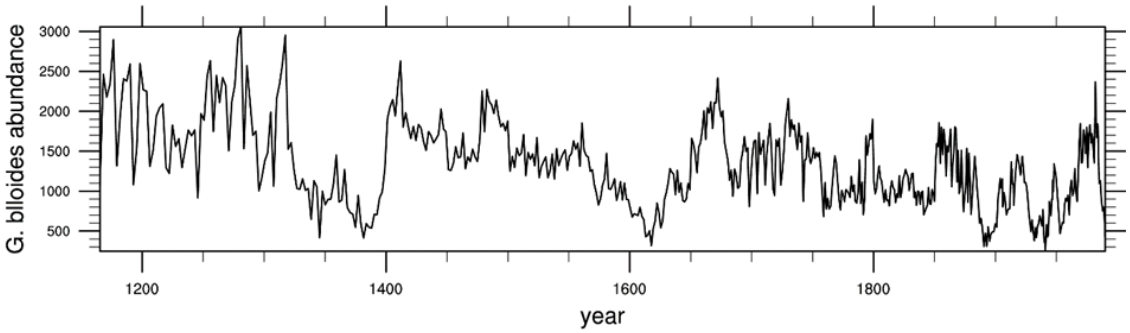

Figure 2-2. G. bulloides abundance (# of G. bulloides/gram) during 1165-1990 [*Black et al.*, 1999].

The sediments were sampled from this box core at continuous 1 mm intervals. Age model for core PL07-71 BC combines ^{210}Pb, varve, and accelerator mass spectrometry (AMS) ^{14}C chronologies, and is described in detail in *Black et al.* [1999]. For the upper 12.6 cm of the core (1880 to 1990 A.D.), the age model for the samples is based on millimeter-scale faunal correlations to a nearby box core whose age model is tightly constrained by a combination of varve and ^{210}Pb dating. Temporal resolution of the data is near annual over this interval, and age model uncertainty is estimated to be ± 1 year. For the depth between 12.6 and 56.4 cm (1165 to 1879 A.D.), laminae were not clear to count. The age model of this section is based on twelve ^{14}C dates dated on monospecific samples of *G. bulloides*. The sample resolution decreases to one sample per 2.5 years at the base, and the errors (1σ) of the lower part of the core could be up to 60 years.

2.1.2 SST proxies and reconstructions

2.1.2.1. Eastern Tropical North Atlantic SST reconstruction

In *Kuhnert and Mulitza* [2011], a *Globigerinoides. ruber* (pink) magnesium-to-calcium ratio (Mg/Ca) SST data is reconstructed for the past 3 millennia. This *G. ruber* (pink) Mg/Ca SST data is considered bearing summer/fall SST signals, attributed to the enhanced productivity of *G. ruber* (pink) during summer, corresponding to the West African Monsoon season.

The sediment site of this data is located off southern Mauritania at 16°50´N, 16°44´W at 323 m water depth. The location is characterized by high terrestrial sediment input and sedimentation rates [*Mulitza et al.,* 2010]. Both of the smoothed SST proxy and local instrumental measurements of SST positively correlate with AMO temperature anomalies [*Kuhnert and Mulitza*, 2011, Figs. 1b and 2b].

Gravity core GeoB 9501-5 and multicore GeoB 9501-4 were recovered during Meteor cruise M65/1. The average internal precision is 0.28% for Mg and 0.22% for Ca concentrations. The age model of the cores is based on a combination of ^{210}Pb and ^{14}C ages [*Mulitza et al.*, 2010]. The errors (±2σ) of the age model are ±11 years for AD 1800, ±44 years for AD 1400, and ±170 years for AD 250. From the gravity core, the average temporal resolution of the Mg/Ca record is 11 years over the younger 1700 years (Fig. 2-3). In this study we only use the data

section younger than AD 1165, which overlaps the time period of *G. bulloides* abundance data and has better time resolution than previous parts.

The calibration for the 250–350 mm fraction of *G. ruber* (pink) from [*Anand et al.*, 2003] is used to calculate SST from Mg/Ca. The overall calibration uncertainty in reconstructed SSTs is equivalent to a ±0.3°C uncertainty. The calibration error is systematic. Based on the above mentioned sources of uncertainty in reconstructed SST, the progressed overall SST error would be ±0.4°C. However, other error sources also exist. Thus, a typical overall SST error of ±1°C is assumed [*Rohling*, 2007].

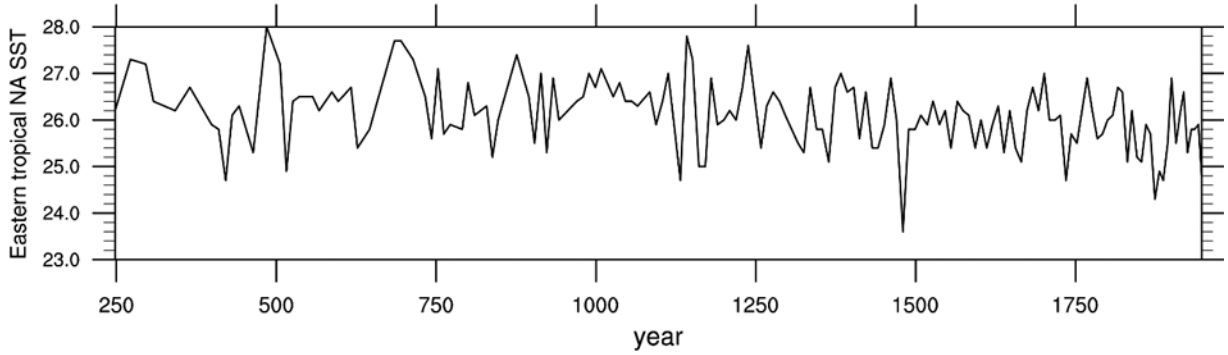

Figure 2-3. Younger 1700 year of SST (°C) reconstruction of Eastern tropical North Atlantic based on G. ruber (pink) [Kuhnert et al. 2011]

2.1.2.2. Puerto Rico SST and Sea surface salinity (SSS) index

Annual time series of coral strontium-to-calcium ratio (Sr/Ca) and $\delta^{18}O$ were constructed to reflect SST and Sea surface salinity (SSS) variations southwest to Puerto Rico in *Kilbourne et al.* [2008] (shown in Fig. 2-4). Larger values of Sr/Ca indicate lower SST, and larger values

(less negative) of $\delta^{18}O$ correspond to lower SST and higher SSS. These time series were constructed on a 245-cm-long core of *Montastraea faveolata*, collected at Turrumote Reef (17.933°N, 67.001°W) offshore from La Parguera, Puerto Rico in August 2004.

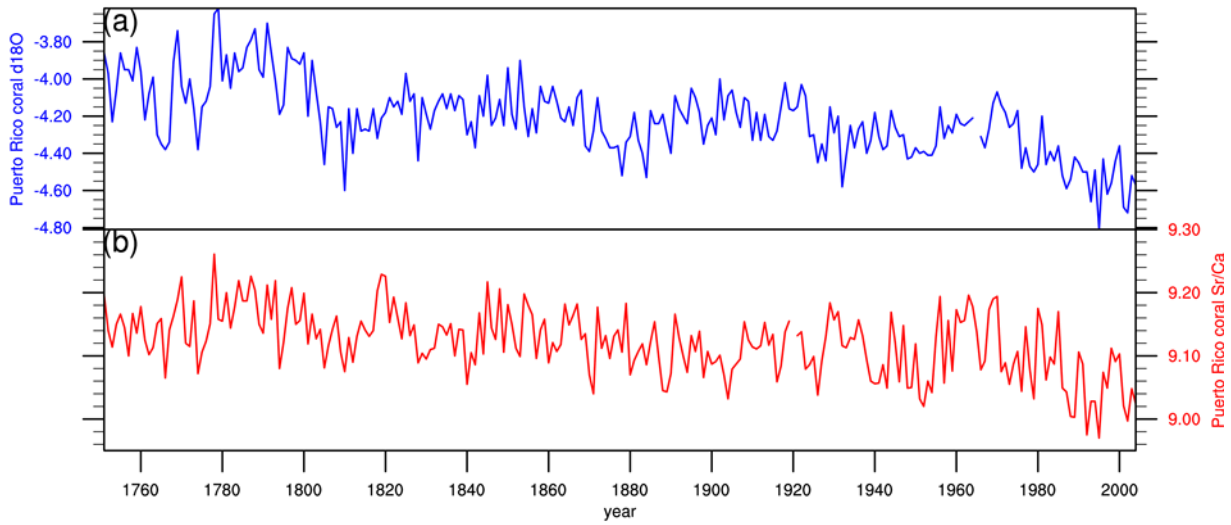

Figure 2-4. Annual variations in $\delta^{18}O$ (‰, blue) and Sr/Ca (mmol/mol, red) based on a coral collected from southwestern Puerto Rico, 1751-2004 [*Kilbourne et al.*, 2008].

Along the axis of maximum growth of the coral core, 5-mm-wide slabs were cut. The X-radiographs of these slabs were used as a guide to ensure that each sample contains one density band. Counting annual density bands provided an age model for these samples. An error of ±1 year was estimated at the bottom of the core.

High-density bands of *M. faveolata* tend to be laid down in the early summer in southwestern Puerto Rico. Thus, the annual samples are approximately centered on January. Based on these annual density bands that centered on the winter season, they took annual subsamples from the entire length of the core and approximately monthly subsamples from the top of the coral. These subsamples were analyzed for Sr/Ca and $\delta^{18}O$.

Long-term analytical precision on $\delta^{18}O$ analyses is 0.06‰ (1σ). And the precision of the Sr/Ca measurements is 0.15% or 0.013 mmol (1σ). Sample heterogeneity may add to the analytical error of Sr/Ca. Averages of multiple replicates are used as the reported Sr/Ca ratios. They have an error of 0.05 mmol/mol (2σ).

2.1.2.3. Cariaco Basin seasonal SST reconstruction

Two annual time series of Mg/Ca SSTs based on *G. ruber* (pink) and *G. bulloides*, respectively, were constructed at Cariaco Basin for the past 2000 year [*Wurtzel et al.*, 2013]. The *G. ruber* (p) Mg/Ca can reflect summer/fall SST, while *G. bulloides* Mg/Ca ratio indicates winter/spring SST (Fig. 2-5). They are also considered to reveal water temperature at different depth, but this indication will not be discussed in this work.

Age models for these two Mg/Ca SSTs were created primary by faunal correlation to nearby core with published age models [*Black et al.*, 1999, 2007]. Based on proxy-instrumental correlations, the dating error for the period of overlapping period with instrumental data (1990-1870 C.E.) is about ± 1 year. The AMS ^{14}C date errors at the base is up to about ± 40-50 years. The in-sample estimate of predictive error for the *G. bulloides* and *G. ruber* (pink) Mg/Ca SSTs are 0.35°C and 0.45°C, respectively [*Wurtzel et al.*, 2013].

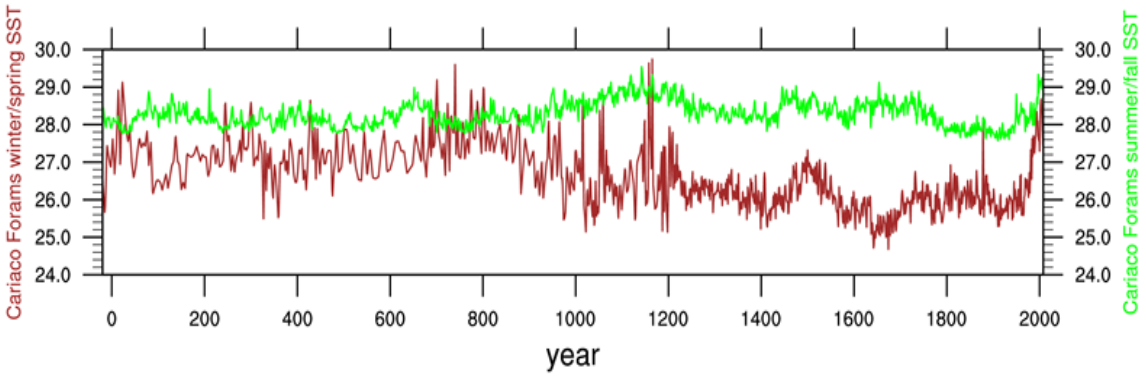

Figure 2-5. -20-2008 G. bulloides Mg/Ca SST (brown), G. ruber (p) Mg/Ca SST (green) [*Wurtzel et al.*, 2013].

2.1.3. North Atlantic Oscillation Mode (NAO) reconstructions

2.1.3.1. Bermuda coral NAO reconstruction

Winter (December-March) SST and coral Sr/Ca at Bermuda show positive correlation with the NAO index on inter-annual frequencies and display negative correlation with it on multidecadal frequencies [*Eden and Willebrand*, 2001; *Kuhnert et al.*, 2005]. Based on this relationship, an 218-year long SST-based reconstruction of NAO index with multi-frequency is constructed [*Goodkin et al.*, 2008a].

The reconstruction uses a brain coral (*Diploria labyrinthiformis*) collected live from the sourtheastern edge of the Bermuda platform (64°W, 32°N), at depth of 16m. Along the axis of maximum growth of the brain coral, 5-mm-thick slabs were cut. The X-radiographs of these slabs reveal well-defined summer–winter seasonal growth bands. Samples were drilled down at 0.33mm intervals to obtain approximately monthly resolution from 1781 to 1999, using the x-

radiographs as a guide. Sr and Ca measurement methods are described in detail in their previous studies [*Goodkin et al.*, 2005, 2008b].

An annual age model is constructed using density banding from X-rays. The age model is refined by maximizing the correlation of monthly averaged SSTs, measured at nearby ocean at Hydrostation S, to monthly Sr/Ca. For the earlier period than the instrumental record, they assign the months by correlating Sr/Ca to Hydrostation S average seasonal climatology data.

To identify winter months, the coral data are re-sampled at monthly intervals with even spaces. Noise in the Sr/Ca record and in the X-radiographs may cause some age model error. The coral age model is more likely to bias by skipping years rather than adding years, because of little or no growth years of the coral. This bias is possible to reach a maximum when growth rates were lowest between 1830 and 1865. Age model bias in the following reconstruction is expected to be less than 15 years.

According to [*Goodkin et al.*, 2008a], cross-spectral analysis of negative winter Sr/Ca record and instrumental data and other proxy NAO reconstructions show significant coherence over periodicities greater than 15 years and between about 3 to 5 years. Also, low frequencies (<0.1 cycles per year) are not considered driven by the NAO, but rather by the northern hemisphere average surface temperature. Thus, the NAO index at frequencies of 3-5 years per cycle and 20-100 years per cycle are generated by applying the Hanning window band-pass

filters (Figs 2-5a, 2-5b). Adding the two filtered time-series together, by inverting the 20-100 year frequency band first, the combined NAO index is formed (Fig 2-5c).

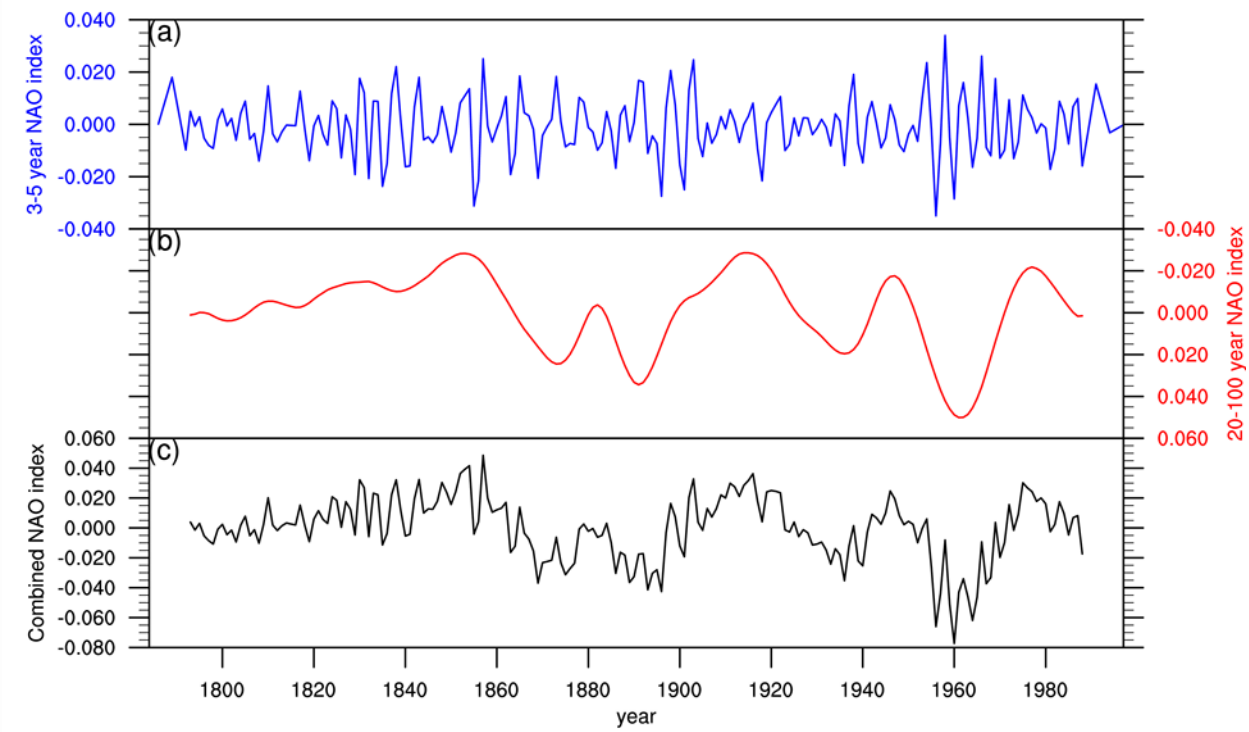

Figure 2-6. (a) 3-5 year NAO index, (b) 20-100 year NAO index (Y-axis reversed), and (c) combined NAO index from Bermuda coral Sr/Ca SST reconstruction [Goodkin et al. 2008]

2.1.3.2. NAO reconstruction based on station data and paleoclimate proxies

A reconstruction of NAO index back to 1500 was statistically constructed based on available station data and paleoclimate proxies [*Luterbacher*, 2002]. The data has seasonal resolution before AD 1658 and monthly resolution afterwards. Fig. 2-6 shows the annual average (Fig. 2-6a) and winter average (Fig. 2-6b) of NAO index based on this data.

Instrumental data series of pressure, temperature, and precipitation and high resolution documentary proxy data (predictors) are used together to form this index. Locations of the data sources are within the area of blue rectangular in Fig. 2-1, and specific locations with corresponding data types are shown in Fig. 1 of [*Luterbacher,* 2002]. The description of data sources can be found in a previous study [*Luterbacher et al.*, 2002].

The NAO index is derived from the regression models built upon all of the predictors. As the database used in the construction varies with time, 328 regression models were developed. The skills of these models are assessed over 1961-1995 (verification period) by the reduction of error (RE) statistic. RE is the expected proportion of the variance of the predictand, given by the predictor. After the assessments recalibration, the NAO index is formed. The detailed method is described in *Jones et al.* [1999] and *Luterbacher et al.* [2002].

Based on the time varying RE for each season, the best model performance was shown for winter. As for spring, summer, and autumn, meaningful estimates of NAO start in the 1720s. The RE values are generally higher than 0.3 for winter, while the ones for other seasons are lower than 0.2 before 1720s.

The results also showed that the quality of the reconstructions of the NAO index increases as more predictors with wider spatial coverage are included. For the monthly data, the performance increases dramatically when the station pressure data is used since 1821. The time-

varying ±2 SE of the winter NAO reconstruction was shown In Fig. 3 of [*Luterbacher*, 2002], and the range of the absolute values is about 1 to 1.5.

Although they have limitations, these reconstructions of past NAO were considered the best guess estimates by 2002, compared to other NAO proxies [*Appenzeller et al.*, 1998; *Cook et al.*, 1998, 2002; *Proctor et al.*, 2000; *Cullen et al.*, 2001; *Glueck and Stockton*, 2001; *Rodrigo et al.*, 2001].

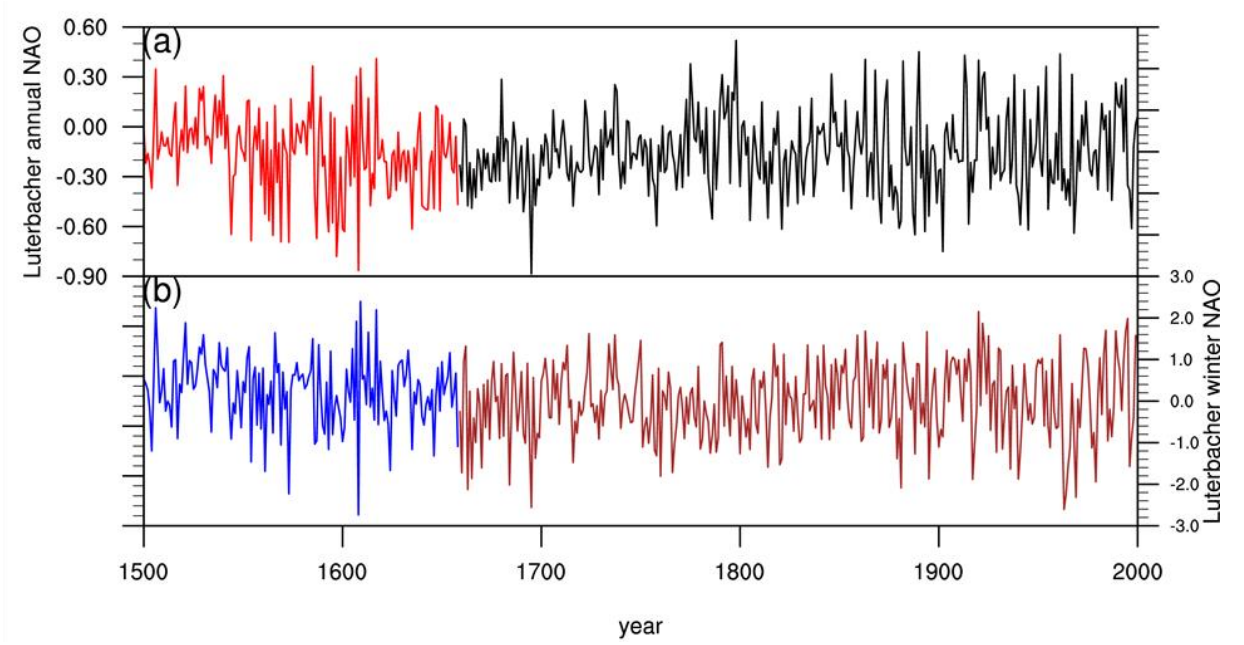

Figure 2-7. (a) annual NAO index (red for 1500-1658, black for 1659-2000); (b) winter NAO index (blue for 1500-1658, brown for 1659-2000) based on seasonal (1500-1658) and monthly (1659-2000) NAO reconstructions in [*Luterbacher*, 2002].

2.1.4. Cariaco Basin titanium concentration data

As a terrigenous material, titanium (Ti) sediment comes from riverine input. Titanium is also not sensitive to redox changes in the environment. Considering Cariaco is an anoxic basin

and the alteration between rainy and upwelling season can be recorded by the sediments lamination in the basin., sediment Ti concentration at this location can reflect time-varying terrigenous input, which are influenced by changes of rainfall and runoff from local watersheds [*Haug et al.*, 2001; *Haug et al.*, 2003].

Titanium concentration (%) data [*Haug et al.*, 2001] is recovered at Ocean Drilling Program (ODP) site 1002 locates at 10°42.739N, 65°10.189W, which was drilled at water depth of 893m. The top 5.5 m of the whole 170 m sediment covers the last 14 ky and is what reported in *Haug et al.*, 2001. Titanium concentration values were measured with a profiling x-ray fluorescence scanner at 2 mm intervals in the sediments, which corresponds to sample intervals of 4 to 5 years.

Age model of this data was based on a series of ten accelerator mass spectrometry (AMS) ^{14}C dates of *G. bulloides*. These dates were transferred to calendar years using the calibration of *Stuiver et al.*, 1998. However, the wiggle-matched titanium record with updated age model is provided in the Supplementary Material (Table S5-6) in *Kennett et al.*, 2012. Based on the conventional ^{14}C ages and depth information for the Holocene Cariaco record in *Hughen et al.*, 2006, these ^{14}C dates calibrated assuming a local reservoir correction. Then, the Cariaco curve is manually adjusted to the YOK-I δ^{18}O record within the error margins of each radiocarbon date [*Kennett et al.*, 2012]. The error of the tuned age model is about ± 90yr for the recent millennium.

The whole tuned time series spans from 9480 B.C. to 1735 C.E. In this study, we will only use the section that overlaps the *G. bulloides* abundance data. The time series of the Ti concentration (%) data during 1110- 1735 is shown in Fig. 2-8.

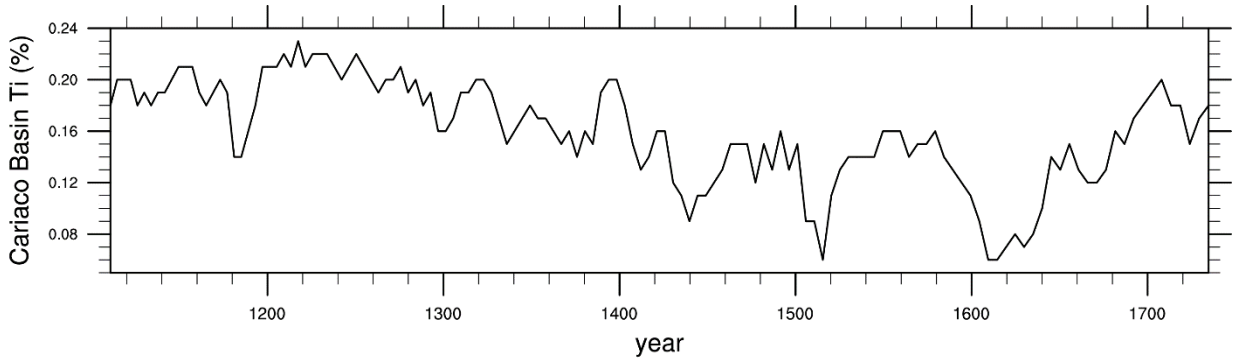

Figure 2-8. 1110-1735 Cariaco Basin Ti (%) rainfall reconstruction [*Haug et al.*, 2001; *Kennett et al.*, 2012b].

2.2. Observation and reanalysis data

For the atmospheric data, we used the newly-released European Centre for Medium-Range Weather Forecasts (ECMWF)'s ERA-20C reanalysis of sub-daily SST, mean sea level pressure (MSLP), and near-surface zonal and meridional wind (10 meter U and V wind component) from 1900 to 2010 [*European Centre for Medium-Range Weather*, 2014]. Horizontal resolution is spectral truncation T159, approximately 125km. ERA-20C reanalysis uses an assimilation methodology of 24-hour 4D-Var analysis, with variational bias correction of surface pressure observations. Surface and mean sea level pressures in ISPDv3.2.6 and ICOADSv2.5.1, and surface marine winds from ICOADSv2.5.1 are the observations assimilated in ERA-20C.

To cross-validate the results, we also applied another longer than 100 year data, National Oceanic and Atmospheric Administration (NOAA)'s 20th Century Reanalysis (version 2) data (NOAA 20CRv2), in the analysis. Variables used in this study are monthly values of mean sea level pressure, and near-surface zonal and meridional wind (U and V wind component at sigma level 0.995) for 1871-2012 [*Compo et al.*, 2011]. The analysis is performed with the Ensemble Kalman Filter (EKF) and generated by assimilating observations of surface pressure and sea level pressure from the International Surface Pressure Databank station component version2, ICOADS, and the International Best Track Archive for Climatic Stewardship (IBTrACS). The model has a horizontal spatial resolution of nearly 200-km on an irregular Gaussian (T62). Monthly SST and sea ice concentration fields from the Hadley Centre Sea Ice and Sea Surface Temperature data set (HadISST1.1) [*Rayner et al.*, 2003] are used as boundary conditions. The monthly values of SST from HadISST1.1 dataset from 1870-present, which has resolution of 1°x 1°, are also used in this study, together with the variables from NOAA 20CRv2 dataset. The NOAA 20CRv2 data is available at NOAA/OAR/ESRL PSD. And the HadISST1.1 dataset can be achieved at Met Office Hadley Center website.

The Japanese 55-year Reanalysis (JRA-55) is also used to verify the results based on the long data sets due to potentially large uncertainty of wind representation. JRA-55 is the longest third-generation reanalysis with improvements such as in assimilation scheme (4D-Var) and model resolution (T319L60), and it also uses full observing system compared to the limited observation assimilation in the long data products like ERA-20C and NOAA 2-CRv2. Fifty-five years of wind and mean sea level pressure from 1958-2013 are used in this study. Its horizontal

spatial resolution is 1.25°x 1.25° [*Kobayashi et al.*, 2015]. The JRA-55 data is downloaded from NCAR's Research Data Archive.

Monthly precipitation data spanning 1901 to 2010 from the Global Precipitation Climatology Centre (GPCC) is used in this study for proxy-modern data comparisons. The precipitation data was constructed from quality-controlled rain gauge measurements at 67,200 stations world-wide with a 10-year or longer record, and a 0.5°x 0.5° spatial resolution [Schneider et al., 2011]. The data is provided by the NOAA/OAR/ESRL PSD, Boulder, Colorado, USA and can be accessed from http://www.esrl.noaa.gov/psd/.

Comparisons in this study to the Atlantic Multidecadal Oscillation (AMO) Index are based on monthly AMO index data spanning 1856 to 2014 from NOAA/OAR/ESRL PSD. The AMO index is calculated by de-trending the time series of area-weighted averaged North Atlantic (between 0°-70°N) SST [*Enfield et al.*, 2001].

The instrumental North Atlantic Oscillation (NAO) Index used in this study is the annual station-based NAO index covering 1965-2014 [*Hurrell*, 1995]. It is based on the difference of sea level pressure (SLP) between Lisbon, Portugal and Stykkisholmur/Reykjavik, Iceland, after normalizing the time series. The data is available at NCAR/UCAR Climate Data Guide.

2.3. Model Simulation Output

Model simulations analyzed in this study are from CMIP5 (Coupled Model Intercomparison Project Phase 5) models. The historical simulations (1850-2005) and past millennium simulations (850-1850) are used in the evaluations in Chapter 5. Due to the availability of the past millennium simulation output data, we only include five models in this study and select one ensemble member for each model. The models, their original atmospheric and oceanic resolution, simulations, and attributes are summarized in Table 2-1.

Table 2-1. CMIP5 models, original resolution, simulations, and attributes.

Models	Modeling Center (or Group)	Institute ID	Resolution	Simulations	Reference
1. Beijing Climate Center, Climate System Model, version 1.1 (BCC-CSM1.1)	Beijing Climate Center, China Meteorological Administration, China	BCC	Air: T42/2.8° Ocean: tri-polar grid (1° lon x 4/3° lat)	Historical Past millennium	[*Wu et al.*, 2013]
2. Community Climate System Model, version 4 (CCSM4)	National Center for Atmospheric Research	NCAR	Air: 0.94° lat x 1.25° lon Ocean: ~1° lon x 0.5° lat	Historical Past millennium	[*Gent et al.*, 2011]
3. Flexible Global Ocean-Atmosphere-Land System Model, spectral version 2.0 (FGOALS-s2)	LASG, Institute of Atmospheric Physics, Chinese Academy of Sciences	LASG	Air: 1.7° lat x 2.8° lon Ocean: 1° lon x 0.5° lat	Historical Past millennium	[*Bao et al.*, 2013]
4. Max Planck Institute Earth System Model, Mixed-resolution version (MPI-ESM-MR) Paleo version (MPI-ESM-P)	Max Planck Institute for Meteorology, Germany	MPI-M	Air: T63/1.9° Ocean: tri-polar grid, 0.4° Air: T63/1.9° Ocean: bi-polar grid 1.5°	Historical Historical Past millennium	[*Giorgetta et al.*, 2013] [*Zanchettin et al.*, 2013]
5. Meteorological Research Institute Coupled Atmosphere–Ocean General Circulation Model, version 3 (MRI-CGCM3)	Meteorological Research Institute, Japan	MRI	Air: T159/1.125° Ocean: 1° lon x 0.5° lat	Historical Past millennium	[*Yukimoto et al.*, 2012]

Chapter 3. Relationship of Cariaco Basin *Globigerina bulloides* Abundance with Atlantic Climate Variability in the Past Century

3.1. Establishing the relationship based on reanalysis data

The *G. bulloides* abundance record (Fig. 3-1a) is characterized by multidecadal variability superimposed on a longer, century-scale pattern, with abundance minima occurring in 1930-40, 1950-60, and after 1985 C. E. Abundance maxima are observed circa 1920 and 1970-80 C. E. There is a weak maximum between 1940 and 1950. Based on spectral analysis of the long term record of *G. bulloides* abundance data, we applied a 15-point low pass Lanczos filtering on the annual data to form the low frequency time series [*Duchon,* 1979]. The same filtering method will be used throughout this section to generate filtered data. In addition to the multidecadal variation, interannual variation at time scales are also observed (Fig. 3-1a).

In this study, we applied the Monte Carlo technique in doing the significance tests of the correlation (and regression) coefficients. For the unsmoothed data, we firstly calculate the correlation of a pair of the detrended and standardized time series (x and y), and then permutated 10000 times of one of the two time series. After detrending and standardizing them, we computed the correlation for each new pair of data, and find the critical value for 95% significance by finding the 95th percentile absolute value of the 10000 correlation values. The p-value is calculated by finding the percentile absolute value of the 10000 correlation values that corresponds to the correlation of the original pair of data (x and y), with $p = 0.05$ corresponding to 95th percentile.

Similarly, the correlation and p-value calculation of the filtered low frequency data are detailed as follows: Firstly, calculate the correlation of the pair of filtered data (detrended and standardized) in interest. Secondly, generate 10000 pairs of random time series with same length by performing 10000 permutations of one time series of the pair, before filtering. Thirdly, apply same time filter to all of these generated random time series, also detrended and standardized. Fourthly, compute the correlation between each pair of the filtered random time series. Finally, find the p-value by finding the 95th percentile absolute value of the correlation values. The p-value is also calculated by finding the percentile which corresponds to the original pair of filtered data. The same technique will be used throughout this study.

The AMO index describes the variability of detrended SST in the North Atlantic (Fig. 3-1b). Low-frequency variability of the negative AMO index is in phase with the *G. bulloides* data. The correlation of the two filtered time series is -0.95, p-value < 0.0001, which strongly suggests that low-frequency variation of *G. bulloides* abundance is caused by climate variability at large spatial scales.

To further illustrate the AMO-*G. bulloides* connection, we show a measure of the large-scale surface air pressure distribution in North Atlantic by using the Azores High index (Fig. 3-1c) [*Hameed and Riemer*, 2012]. The pressure index is defined as a monthly area-weighted pressure departure from a threshold value over the domain (I, J):

$$I_p = \frac{\sum_{ij=1}^{IJ}(P_{ij} - P_t)\cos \emptyset_{ij}\,(-1)^M \delta_{ij}}{\sum_{ij=1}^{IJ}\cos \emptyset_{ij}\,\delta_{ij}}, \quad (3.1)$$

where P_{ij} is the SLP value at grid point (i, j), P_t is the threshold SLP value ($P_t = 1014\ hPa$ for Azores High), and $\emptyset_{ij}$ is the latitude of grid point (i, j). M = 0 for the Azores High. $\delta = 1$ if $(-1)^M(P_{ij} - P_t) > 0$ and $\delta = 0$ if $(-1)^M(P_{ij} - P_t) < 0$. The pressure index measures the anomaly of an air mass over the chosen sector (I, J), which is (20°N-50°N, 70°W-10°E) [*Hameed and Riemer*, 2012]. In our study, we also defined another low-latitude Azores High index over the domain of (0°-30°N, 0°-80°W) to track the highest North Atlantic pressure south to 30°N (based on Fig. 3-2a, which will be discussed immediately). It will be specified when the low-latitude index is used. There is good correlation in the Azores High with both the AMO and *G. bulloides* abundance (r = -0.87, p-value = 0.0008 with AMO index and r = 0.92, p-value = 0.0002 with *G. bulloides*, using filtered time series; Table 3-1).

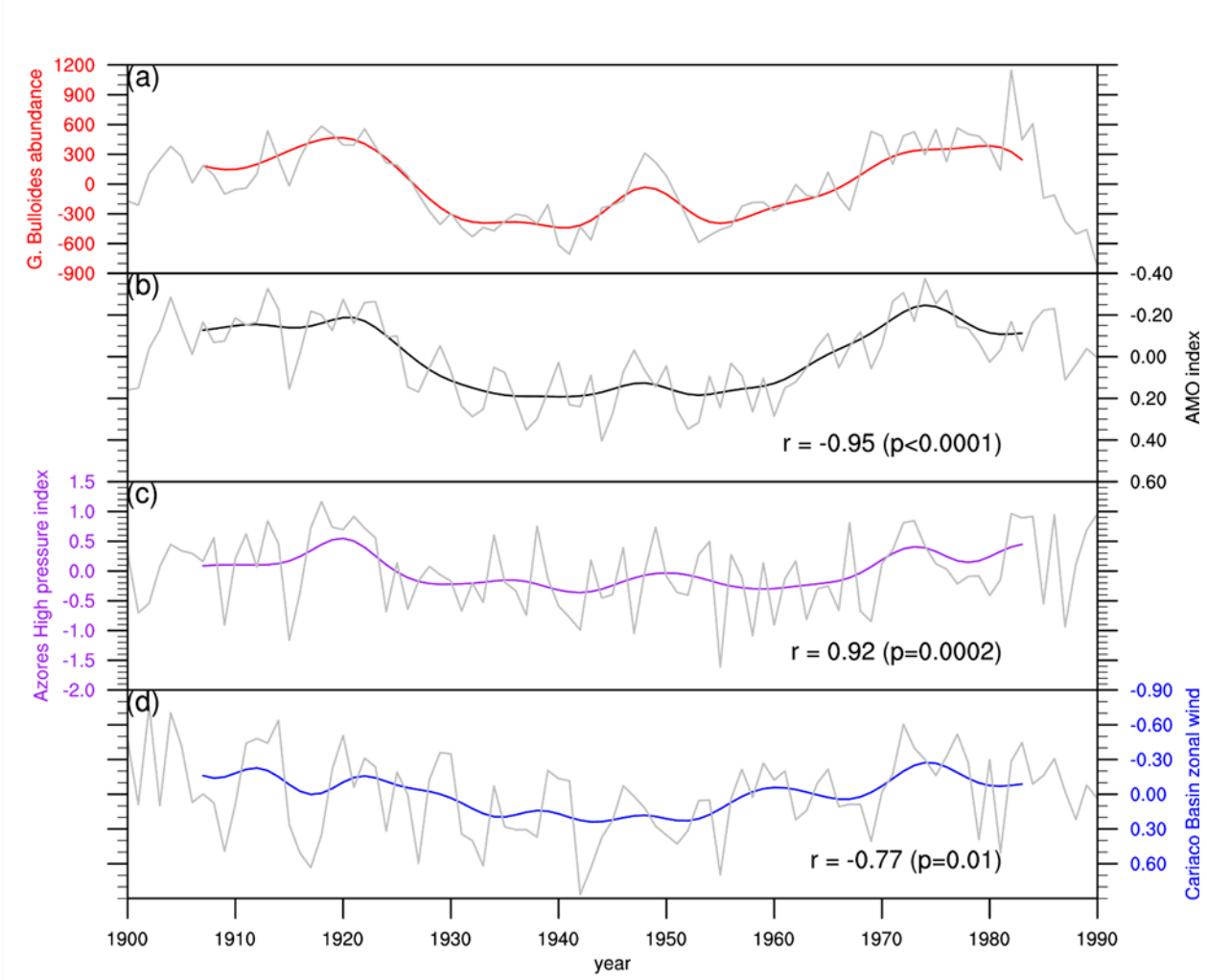

Figure 3-1. 1900-1990 de-trended annual mean (grey lines) and filtered time series (other color lines) of (a) G. bulloides abundance; (b) AMO index; (c) Azores High pressure index; and (d) Cariaco Basin surface zonal wind. Y-axes of (b) and (d) are reversed. A 15-point Lanczos low pass filter is applied to generate the low-frequency data. Correlation coefficients (r) and p-values (p) of G. bulloides abundance data and climate variables in (b), (c), and (d) are shown in the figure. Data source: ERA-20C.

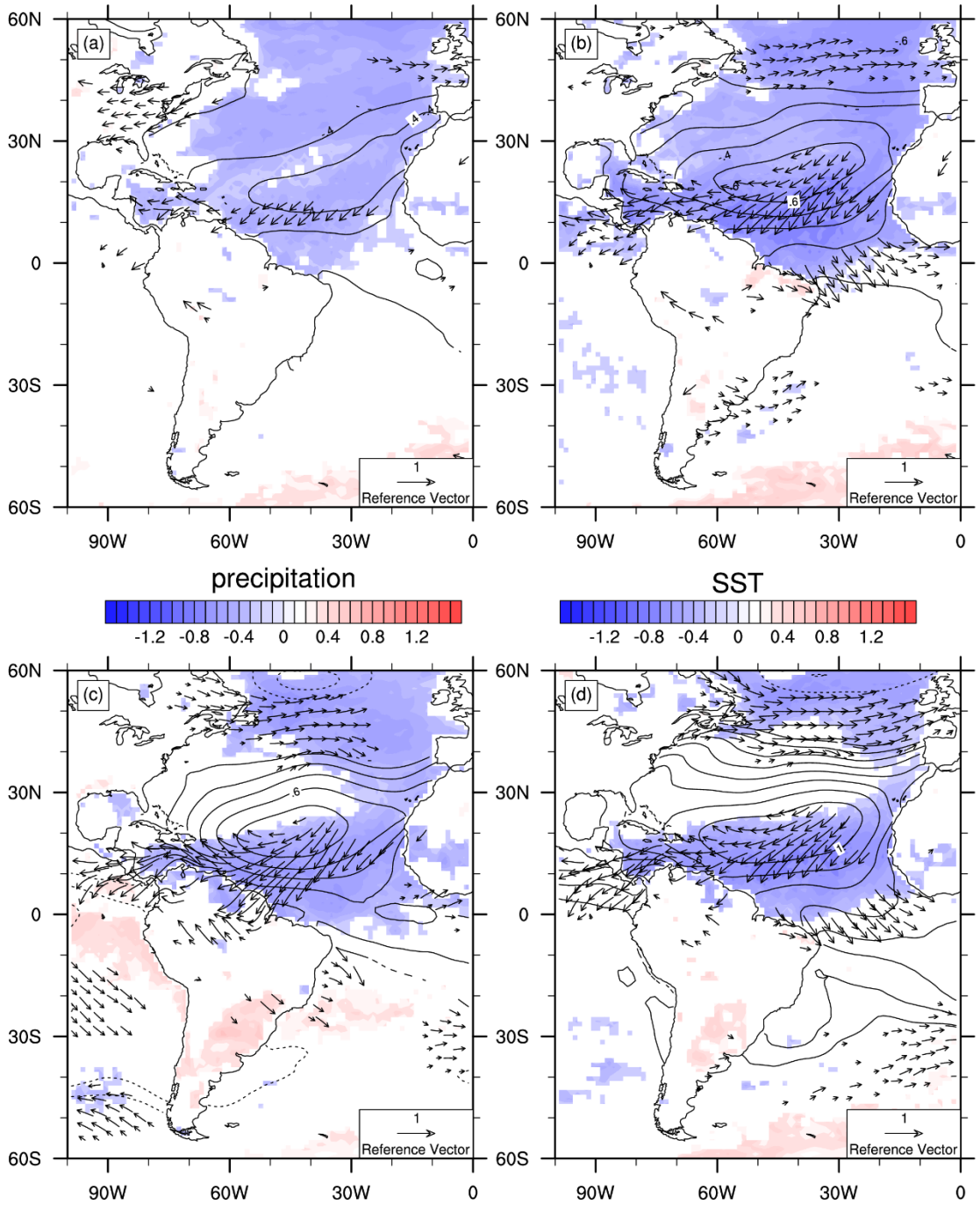

Figure 3-2. 1901-1990 de-trended standardized annual mean precipitation (color shades over land), SST (color shades over ocean), Sea level pressure (contours over ocean), and Surface wind (vectors) regression against de-trended standardized annual mean (a) G. bulloides abundance; (b) negative AMO index; (c) negative Cariaco Basin surface zonal wind (easterly wind); and (d) Azores High pressure index. Displayed values passed 95% significance level. Vectors are shown when regression of U-component passed 95% significance level. Contours with dashed lines. Data source: ERA-20C.

Table 3-1. Cross-correlation coefficient between Globigerina bulloides abundance and low-frequent Atlantic climate variabilities (r: correlation coefficient; p: p-value. Data are annual mean data filtered by 15-point Lanczos filter). Data source: ERA-20C.

	AMO	Azores High pressure	Zonal wind
G. bulloides	r = -0.95, p < 0.0001	r = 0.92, p = 0.0002	r = -0.77, p = 0.01
AMO		r = -0.87, p = 0.0008	r = 0.88, p = 0.0002
Azores High pressure			r = -0.66, p = 0.03

The connection between *G. bulloides* and large-scale ocean-atmospheric climate variability is clearly seen in a regression of SST and sea-level pressure against the *G. bulloides* data (Fig. 3-2a). The distributions of the regression coefficients are spatially coherent with high *G. bulloides* abundance associated with colder SST in the North Atlantic and a stronger Azores High. Similar relationship between *G. bulloides* abundance with North Atlantic SST and Azores High is demonstrated in the same regression map derived from filtered time series (Fig. 3-3a).

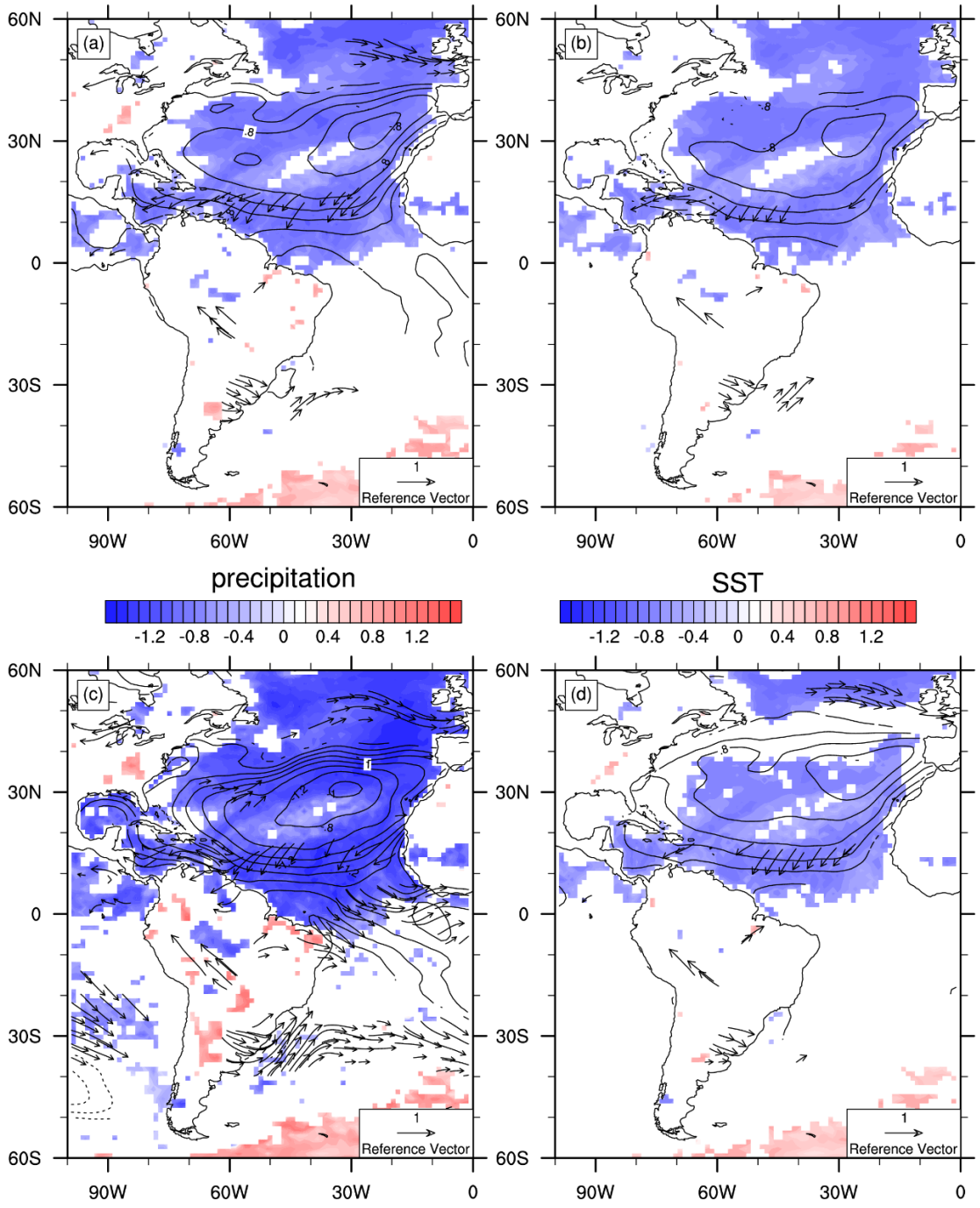

Figure 3-3. The same as Fig. 3-2, except for low-frequency data (filtered by 15-point Lanczos low pass filtering). Displayed values passed 95% significance level. Data source: ERA-20C.

Colder North Atlantic SSTs are associated with a stronger subtropical high as colder SST corresponds to greater atmospheric subsidence [*Hastenrath and Greischar*, 1993]. This association is shown in Fig. 3-2b in which SST and sea level pressure are regressed against an inversed AMO index. The inversed index is used to make the regression map have the same positive/negative sign as other regressions presented in this study. As this study revolves around *G. bulloides* abundance, the time series that has negative correlation with *G. bulloides* abundance needs to flip sign (i.e. AMO index and local zonal wind time series). Using these two sign-flipped time series and regressing all other variables on them, we can get regression maps (Fig. 3-2b, 3-2c) that easily compare to the other two (Fig. 3-2a, 3-2d). As a result, the spatial pattern in Fig. 3-2b is very similar to the one observed in Fig. 3-2a. The same plot with filtered time series (Fig. 3-3b) also shows a pattern highly resembling Fig. 3-3a. However, unlike in Fig. 3-2a (3-2b), Fig. 3-3a (3-3b) shows that connection between *G. bulloides* (AMO index) and SLP are covering higher latitudes in the eastern North Atlantic.

Why then is *G. bulloides* concentration related to the large-scale SST and air pressure distributions? In Figs. 3-2a and 3-2b, we included the regression of surface winds against the *G. bulloides* data and the negative AMO index respectively. As expected, a stronger Azores High is associated with anomalous anti-cyclonic surface flow, which registers a larger easterly wind anomaly in the tropical North Atlantic and in the region of the Cariaco Basin. The regression of surface winds on the *G. bulloides* data (Fig. 3-3a) and the negative AMO index (Fig. 3-3b) with filtered time series gives similar relationship. It is evident that the largest correlation between low-frequency *G. bulloides* data and tropical zonal wind are along the southern flank of the large correlation zone of *G. bulloides* data and SLP.

We used the averaged zonal winds over the coastal region in (9.5°N-14.5°N, 60°W-70°W) to represent the along-coast winds in the Cariaco Basin (Fig. 3-1d). There is a weaker but still significant correlation between zonal wind in the local coastal region and *G. bulloides* abundance (r = -0.77, p-value = 0.01, using filtered time series). It is consistent with the fact that a high easterly wind anomaly induces offshore surface currents in the Cariaco Basin and therefore causes upwelling, and increases *G. bulloides* production. The lower correlation between the Cariaco Basin zonal winds and *G. bulloides* abundance could be due to the large synoptic variability of the winds at small scales as compared to smoother large-scale circulation measurements like the AMO and Azores High pressure index.

When we regressed the spatially distributed winds, SST and surface pressure against the local surface easterly wind over the Cariaco Basin (Fig. 3-2c), we observe very similar patterns in these fields in the Atlantic to those regressed against the *G. bulloides* and the inversed AMO index (Figs. 3-2a and 3-2b). The similarity strongly suggests that the variability of the local easterly wind over the basin is part of the large-scale climate variability in the North Atlantic, which are all correlated with the *G. bulloides* data. While the same plot with low-frequency data (Fig. 3-3c) displays similar patterns as in Fig. 3-2c and its counterparts regressed on *G. bulloides* and the inversed AMO index (Figs. 3-3a and 3-3b). Again, they are all consistent in the association between cold North Atlantic SST, intense subtropical high pressure, and large easterly wind in the tropical North Atlantic and near Cariaco Basin.

To further confirm the relevant climate variability induced by the Azores High pressure anomaly, Fig. 3-2d shows the same regressions against the low-latitude Azores High index based

on annual data. Again, the spatial patterns of the variables are consistent with those in the other plots (Figs. 3-2a, 3-2b, and 3-2c). In the other hand, Fig. 3-3d gives the same regressions on the original Azores High index based on filtered time series. The choice of Azores High pressure index is determined by the regression pattern of SLP on *G. bulloides,* (e.g. Fig. 3-2a for annual data and 3-3a for filtered data). In Fig. 3-3d, the regression map of the variables are also quite consistent with their counterparts in other plots (Figs. 3-3a, 3-3b, and 3-3c). The relationship between these climate variables are also shown as correlation coefficients in Table 3-1.

In addition to local easterly wind-induced upwelling, regional precipitation over land is another meteorological factor that can potentially impact *G. bulloides* abundances in the basin. Greater precipitation over northern Venezuela leads to increased fluvial input of nutrients to the Cariaco Basin, in turn spurring local primary productivity and increased foraminiferal abundance [*Peterson et al.*, 2000]. However, *G. bulloides* abundance's correlations with terrestrial precipitation (Fig. 3-2a) do not show significant correlation in local precipitation and even display a negative correlation in Sahelian precipitation at Africa, especially in the summer-fall season (Fig. 3-4a in the next section). Moreover, lower North Atlantic SST (Fig. 3-2b), stronger local easterly winds (Fig. 3-2c), and a higher Azores High south to 30°N (Fig. 3-2d) correspond to less precipitation over the Cariaco Basin watershed and Sahel region, which indicates an association with southward shift of ITCZ (Intertropical Convergence Zone). The potential connection between these variables with ITCZ rainfall is not clear based on low-frequency time series (Fig. 3-3), except for local zonal wind (Fig. 3-3c). The spatial patterns suggest that continental precipitation near the Cariaco Basin is not positively correlated to *G. bulloides* for

the interval of this study. Nevertheless, the precipitation factor may play crucial roles in the *G. bulloides* abundance variation at longer time scales, which will be discussed in Section 3.4.

Other than easterly trade wind and local watershed rainfall, aeolian dust transport can also contribute to Cariaco Basin sea surface nutrients variability and thus influence the *G. bulloides* production. Negative phase of AMO is connected to reduced Sahelian rainfall and anomalously more dust in the atmosphere, and the tropical Atlantic low-level easterly wind anomalies can also contribute to bringing African dust to as far as Carribean seas [*Prospero and Lamb*, 2003; *Wang et al.*, 2012]. Moreover, previous studies have looked at the connections between Cariaco Basin nutrients to Sahel dust [*Yarincik et al.*, 2000; *Martinez et al.*, 2007].

In this section, we showed that colder North Atlantic SST and stronger low-latitude Azores High anomalies relate to higher local coastal and tropical Atlantic easterly wind, as well as to less Sahel rainfall (in the summer-fall season, which will be shown in Fig. 3-4). Stronger local easterly wind will enhance the upwelling, reduced summer-fall rainfall at Sahel can induce more atmospheric dust, and the stronger cross-Atlantic tropical easterly wind may bring the dust to the location of Cariaco Basin. All of these factors can increase the Cariaco Basin surface nutrients and *G. bulloides* production. This may be the reason that the collective effect of the large circulation variability of AMO and Azores High pressure can have better relationship with Cariaco Basin *G. bulloides* abundance data.

Finally, we have also examined the lag correlations between the de-trended low-frequency time series of *G. bulloides* abundance, the AMO index, Cariaco Basin surface zonal winds, and the Azores High index, and found that the almost concurrent correlations near zero lag have the largest magnitudes. More specifically, when *G. bulloides* abundance leads for one year, its correlations with Cariaco Basin surface zonal winds, and the Azores High index reach largest magnitude; and when *G. bulloides* abundance lags for one year, its correlation with the AMO index is the largest. However, this may not be revealing of specific lead-lag mechanism, considering the age model uncertainty of *G. bulloides* abundance data (± 1 year in this interval).

3.2. Seasonal Analysis

Seasonal analysis found that the AMO index, Cariaco Basin surface zonal wind, and the Azores High index in the season of July-August-September (JAS) has better relationship with *G. bulloides* abundance with a more similar spatial distribution of corresponding regression coefficients based on annual data (Fig. 3-4).

This result is surprising at first, as the JAS season is a non-upwelling season. However, based on the analysis of seasonal cycle and monthly extreme of surface zonal wind, we found that the most evident relationship between these variables and *G. bulloides* abundance can occur in the weak-upwelling season.

Although Cariaco Basin zonal wind peaks in winter/spring (Fig 3-5a, black line) when the primary peak of *G. bulloides* production happens due to high wind driven coastal upwelling, similar regression maps applying winter/spring climate variabilities (e.g., Fig. 3-6a) do not show resembling patterns as in Fig.. 3-2a, while the ones using summer/fall variables (e.g., Fig. 3-6b) show closely similar patterns.

To find out the reason behind this phenomenon, we grouped the years to four quartiles by *G. bulloides* abundance and compared the seasonal cycle of mean zonal wind during the years in the upper quartile and in the lower quartile (Fig. 3-5a, red line and blue line, note that stronger easterly wind is indicated by larger negative values). The difference of zonal wind between the years in the upper quartile and lower quartile turns out to be largest in summer/fall season instead of winter/spring (Fig. 3-5b).

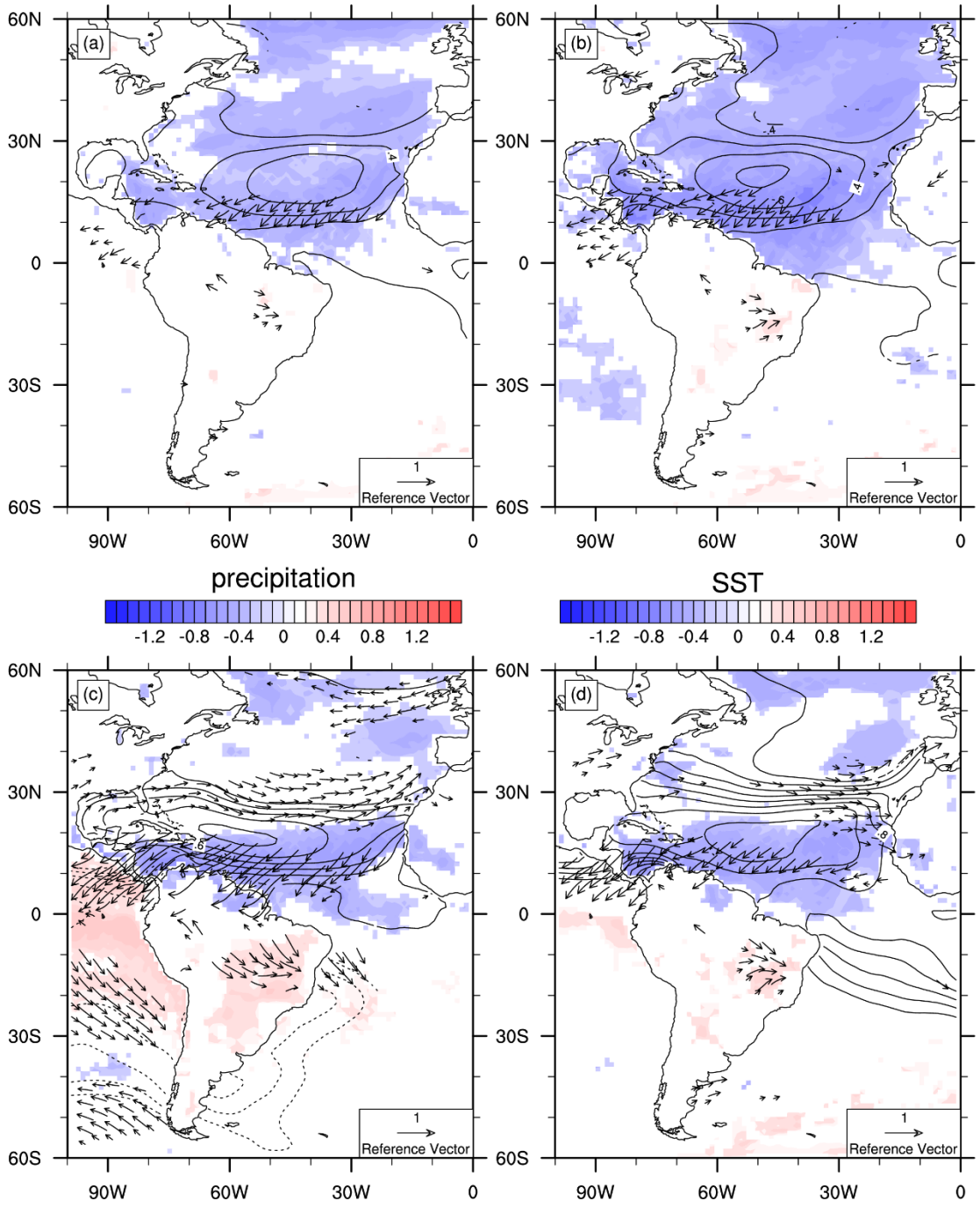

Figure 3-4. 1901-1990 de-trended standardized JAS mean precipitation (color shades over land), SST (color shades over ocean), Sea level pressure (contours over ocean), and Surface wind (vectors) regression against de-trended standardized annual mean (a) G. bulloides abundance; (b) negative AMO index; (c) negative Cariaco Basin surface zonal wind (easterly wind); and (d) Azores High pressure index. Displayed values passed 95% significance level. Vectors are shown when regression of U-component passed 95% significance level. Contours with dashed lines indicate negative values. Line labels on white background are for contours, others are for color shades. Data source: ERA-20C.

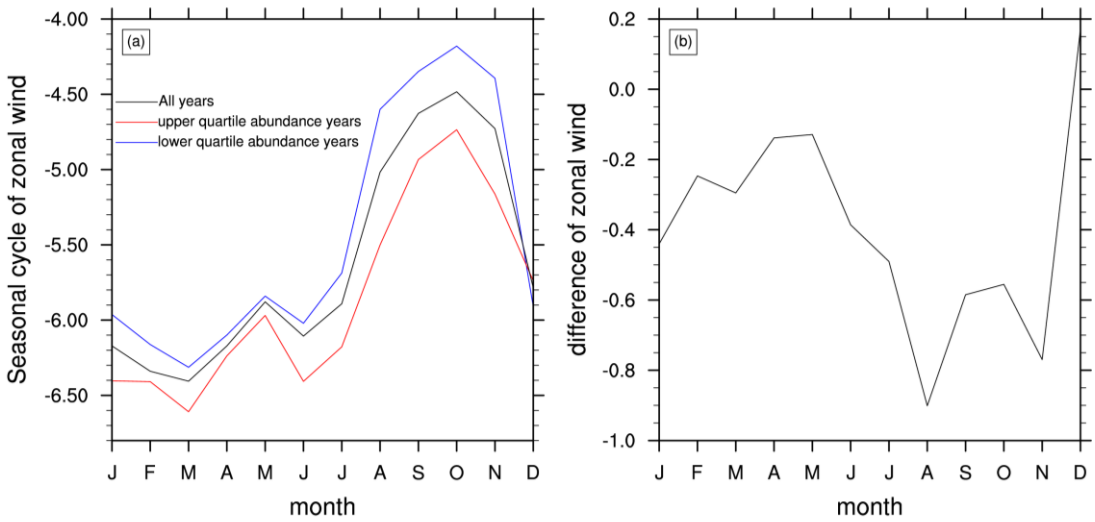

Figure 3-5. 1900-1990 seasonal variation of Cariaco Basin (a) mean zonal wind in all years (black line), in the years with upper quartile of G. bulloides abundance (red line), and in the years with lower quartile of G. bulloides abundance (blue line); (b) zonal wind difference between the years with upper quartile and lower quartile of G. bulloides abundance. Data source: ERA-20C.

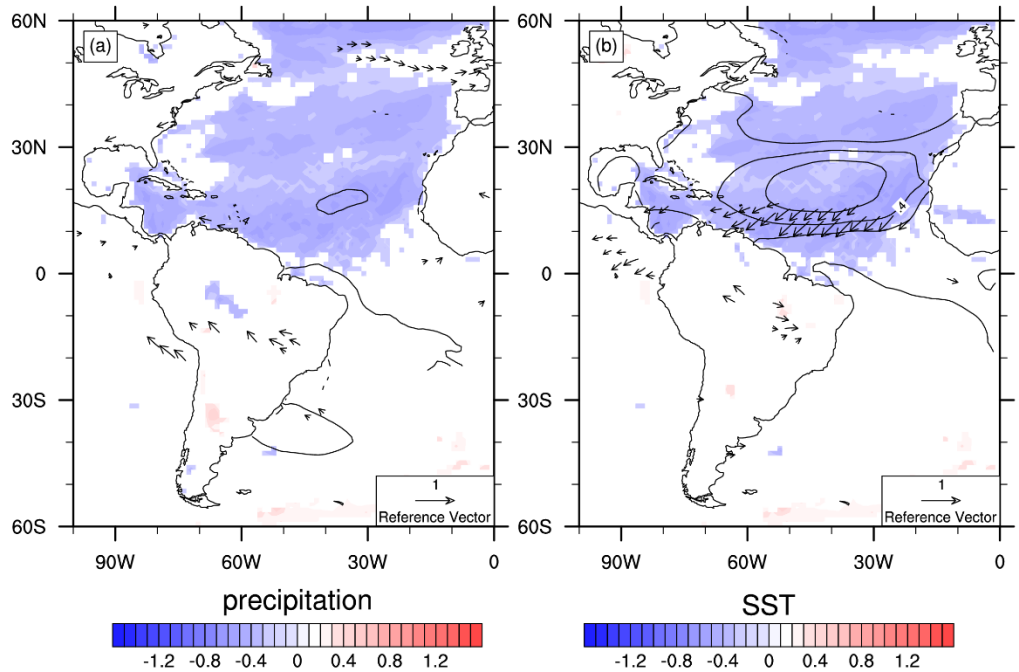

Figure 3-6. 1901-1990 de-trended standardized (a)JFM mean precipitation (color shades over land), SST (color shades over ocean), Sea level pressure (contours over ocean), and Surface wind (vectors) regression against de-trended standardized annual mean G. bulloides abundance; (b) the same as (a) except using JAS mean precipitation, SST, Sea level pressure, and Surface wind. Displayed values passed 95% significance level. Vectors are shown when regression of U-component passed 95% significance level. Contours with dashed lines indicate negative values. Line labels on white background are for contours, others are for color shades. Data source: ERA-20C.

In addition, to examine whether summer/fall zonal wind speed can also reach magnitude that comparable to winter/spring, a monthly extreme wind index is constructed. The zonal wind index is calculated using daily zonal wind data from ERA-20C reanalysis during 1900-2010. The index is defined as average daily zonal wind (U) speed in a month that exceeds the threshold of one standard deviation of zonal wind during 1900-2010. As the mean zonal wind is negative, the monthly zonal wind index can be calculated as:

$$U\ wind\ index = \frac{\sum_{i=0}^{N} U_i \times n_i}{N_e},$$

$$N_e = \sum_{i=0}^{N} n_i\ , \begin{cases} n_i = 1, when\ U_i < U_t \\ n_i = 0, when\ U_i \geq U_t \end{cases}, \quad (3.2)$$

where N is the number of the days in the month, U_i is the zonal wind in the ith day of the month, N_e is number of days that daily zonal wind speed exceeds the threshold, U_t is the threshold of zonal wind, $U_t = long\ term\ mean\ (U) - standard\ deviation(U)$ during 1900-2010.

Here, we present a zoomed in section of the extreme wind index (U wind index) in Fig. 3-7 for a 10-year period, along with corresponding monthly extreme zonal wind days (N_e). We can see that summer/fall zonal wind speed can also reach magnitude that comparable to winter/spring, but with less occurrences. These results indicate that inter-annual variation of *G. bulloides* abundance is possible to be largely impacted by change of summer/fall zonal wind and upwelling, while the value of *G. bulloides* abundance being largest in winter/spring.

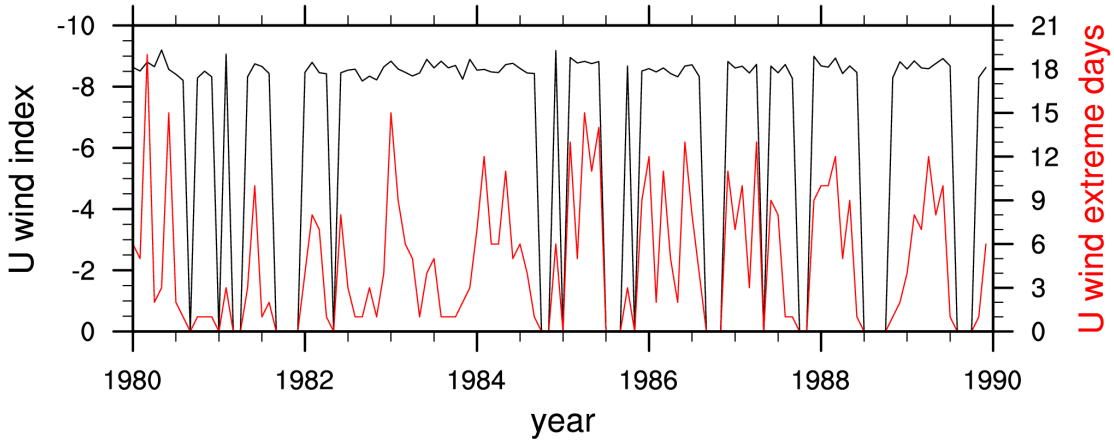

Figure 3-7. 1980-1989 section of monthly zonal wind index (black line; see Index Definition 2) and number of days in a month that daily zonal wind speed exceeds threshold of one standard deviation (Ne) (red line). Data source: ERA-20C.

To see whether the low-frequent summer/fall variables have similar relationship with *G. bulloides* abundance and AMO, we also regressed them on filtered time series of the *G. bulloides* data and AMO index (Figs. 3-8a and 3-8b). It demonstrates that larger *G. bulloides* abundance is related to colder North Atlantic SST and more intense North Tropical Atlantic SLP and zonal wind, stronger easterly wind along the Cariaco Basin, and less Sahel rainfall in JAS.

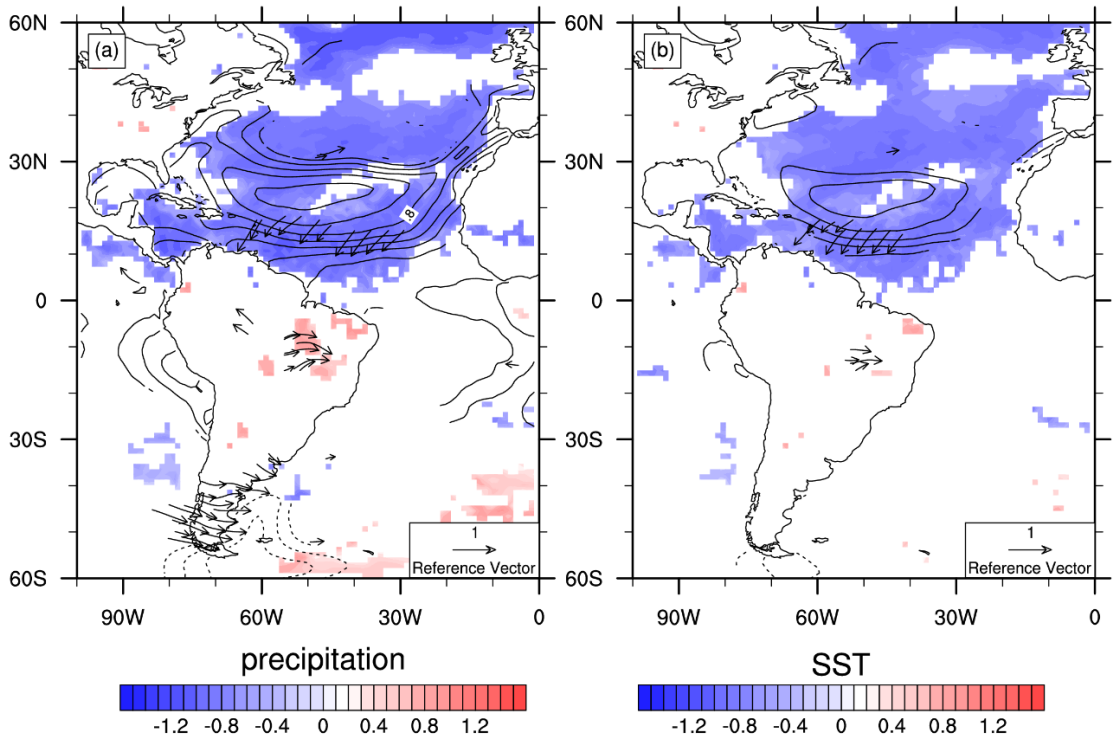

Figure 3-8. The same as Fig. 3-4a and 3-4b, except for low-frequency data (filtered by 15-point Lanczos low pass filtering). Data source: ERA-20C.

3.3. Cross-validation of the results using other reanalysis data

Above shown results are only based on one data set. In this section, we will cross-validate these results with NOAA 20CRv2 data during 1871-2010, as well as with JRA-55 data during 1958-2013.

Firstly, same multiple time series comparison is done among *G. bulloides* abundance data, AMO index, Azores High pressure index, and Cariaco Basin zonal wind based on NOAA 20CRv2 data during the common time period, 1871-1990 (Fig. 3-9). Comparing the correlation

coefficients in this Figure to the ones in Fig. 3-1, we found that the correlation between *G. bulloides* abundance data and Cariaco Basin zonal wind are not significant (Fig. 3-9d). The *G. bulloides* abundance's correlation with the Azores High pressure index is still significant using this data set (Fig. 3-9c).

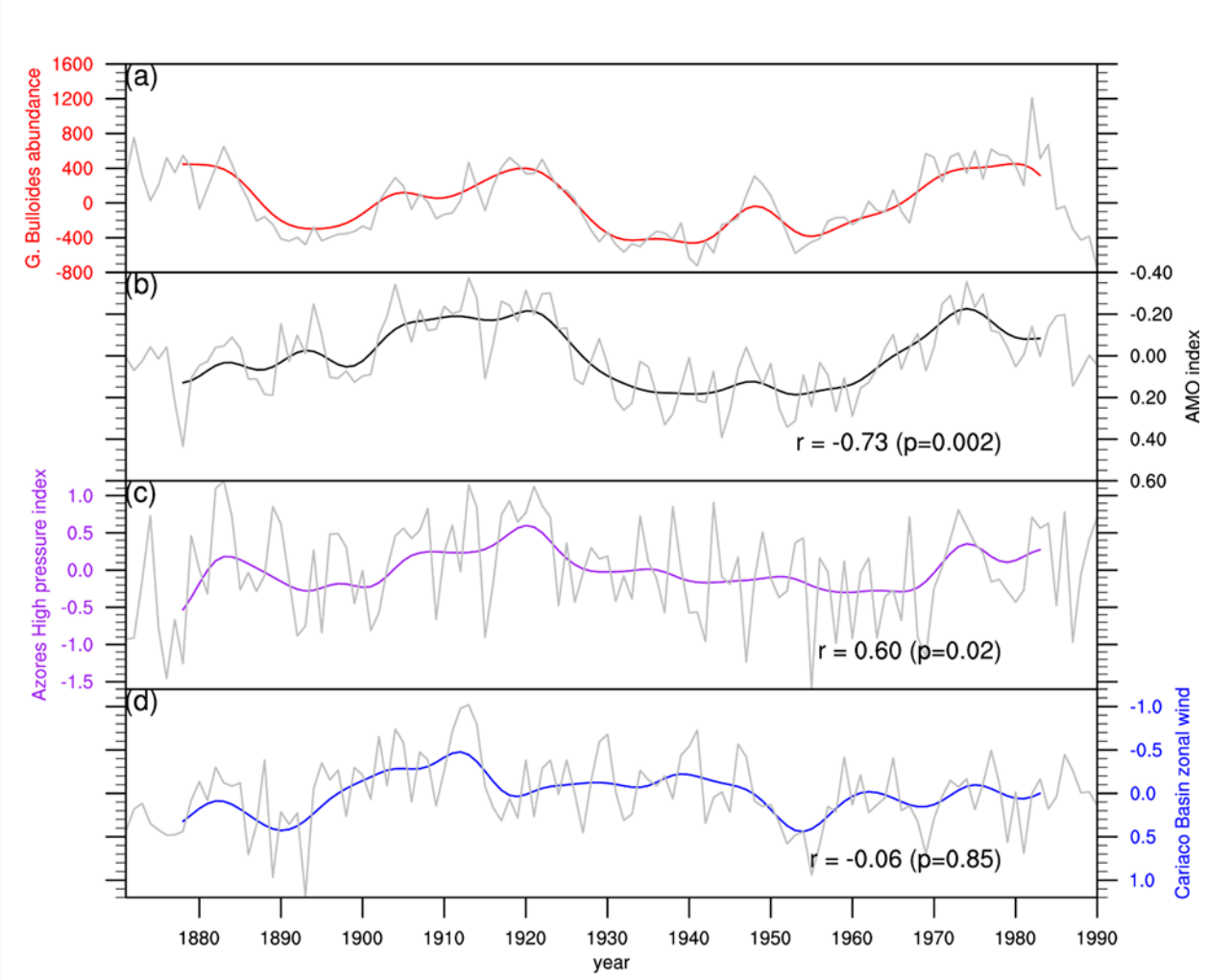

Figure 3-9. 1871-1990 de-trended annual mean (grey lines) and filtered time series (other color lines) of (a) G. bulloides abundance; (b) AMO index; (c) Azores High pressure index; and (d) Cariaco Basin surface zonal wind. Y-axes of (b) and (d) are reversed. A 15-point Lanczos low pass filter is applied to generate the low-frequency data. Correlation coefficients (r) and p-values (p) of G. bulloides abundance data and climate variables in (b), (c), and (d) are shown in the figure. Data source: NOAA 20CRv2.

Replicating Fig. 3-2 with the surface wind and SLP data from NOAA 20CRv2 and SST data from HadISST1.1, Fig. 3-10 is produced. Regression spatial distribution of each panel in Fig. 3-10 is similar to Fig. 3-2, except for Fig. 4-10a. In Fig. 4-10a, the larger *G. bulloides* abundance data does not significantly relate to local coastal zonal wind, but rather to zonal wind in the band over the North Tropical Atlantic.

Moreover, the cross-correlation between each pair of the low-frequency time series in Fig. 3-9 reveals that Cariaco Basin zonal wind does not significantly correlate to any of the other three variables. The correlation coefficient and p-value for each pair are listed in Table 3-2.

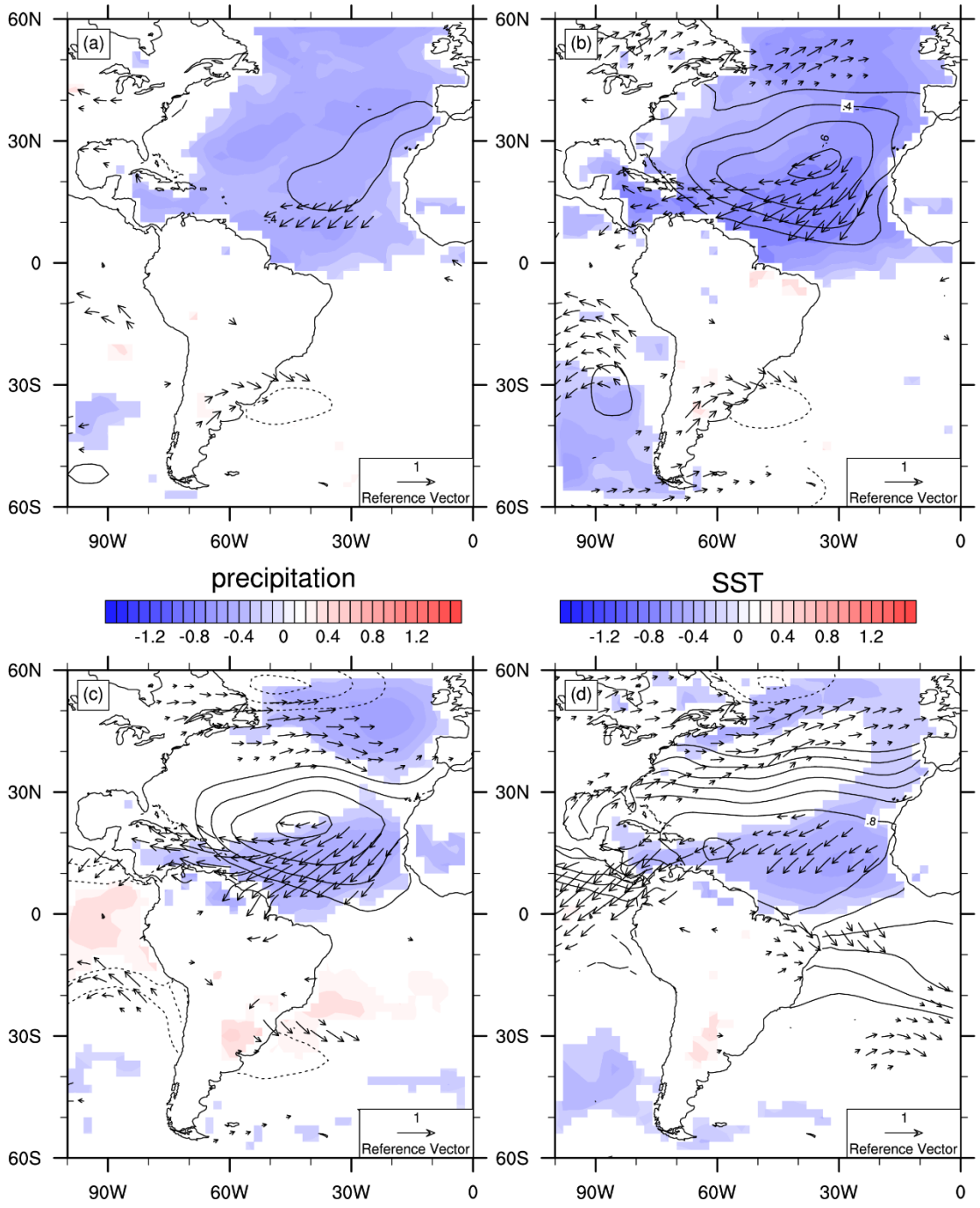

Figure 3-10. The same as Fig. 3-2 except for Data source: NOAA 20CRv2.

Table 3-2. The same as Table. 3-1 except for during 1871-1990, Data source: NOAA 20CRv2.

	AMO	Azores High pressure	Zonal wind
G. bulloides	r = -0.73, p = 0.002	r = 0.60, p = 0.02	r = -0.06, p = 0.85
AMO		r = -0.73, p = 0.001	r = 0.38, p = 0.19
Azores High pressure			r = -0.40, p =0.15

This phenomena is also exemplified in the regression maps based on the low-frequency data. Fig. 3-11 is generated by reproducing Fig. 3-3 with the surface wind and SLP data from NOAA 20CRv2 and SST data from HadISST1.1. The relationship indicated by this plot is also largely consistent with Fig. 3-3, except for the connections involving Cariaco Basin zonal wind. In Fig. 3-11c, the regression coefficients of Cariaco Basin coastal zonal wind do not display much relationship with other fields or zonal wind over other locations other than local area. Applying shorter time span in the calculation also results in similar pattern (not shown). This result is dubious. As NOAA 20CRv2 does not assimilate wind fields, we suspect this inconsistency may come from the uncertainty of surface wind in this data set. To investigate if this is the case, we will include another reanalysis data to do the verification.

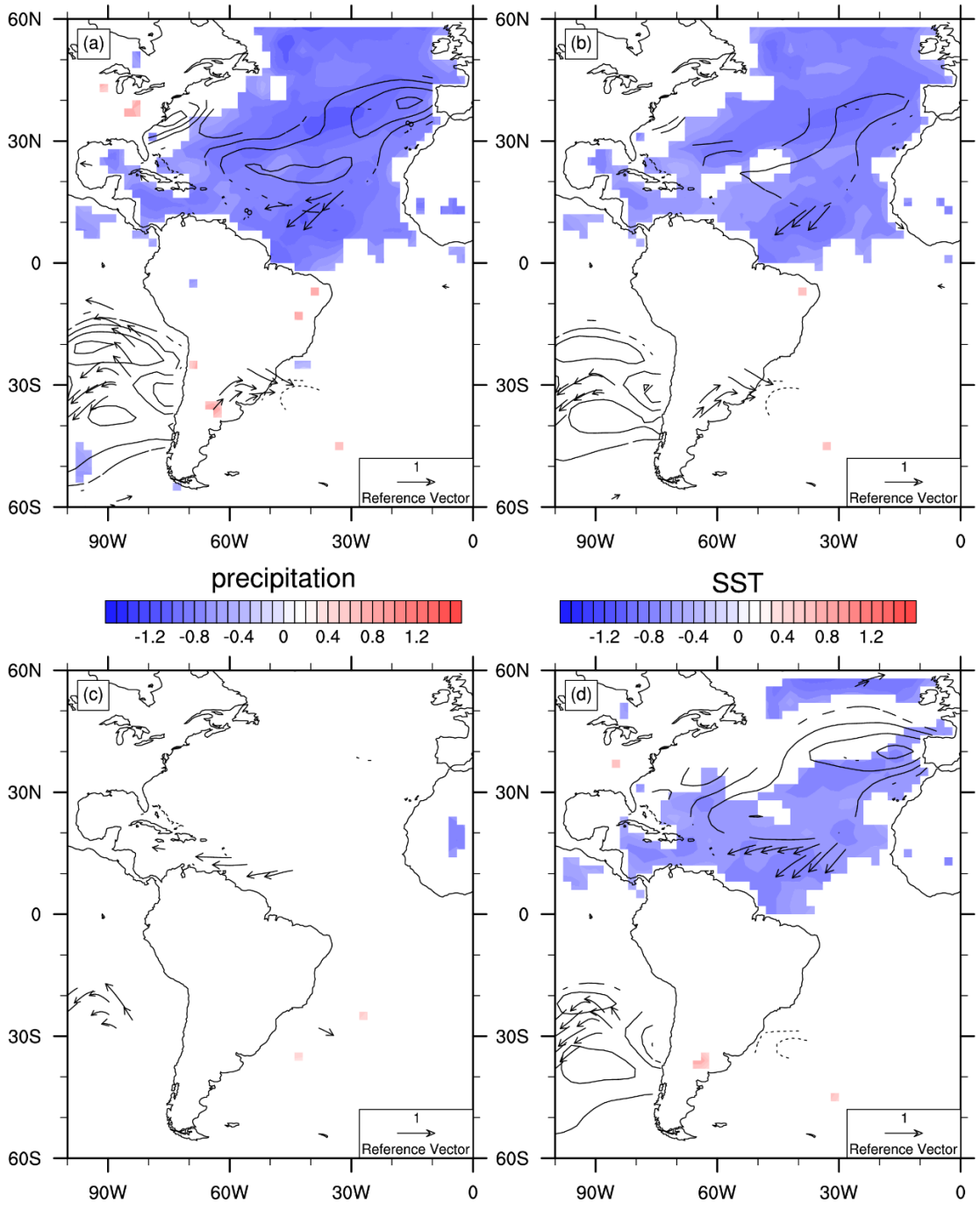

Figure 3-11. The same as Fig. 3-3 except for Data source: NOAA 20CRv2.

Before the verification with the other reanalysis data, the same replication of regression maps based on NOAA 20CRv2 and HadISST1.1 data are also done for seasonal analysis (Fig. 3-12 to Fig. 3-14). The spatial patterns of the regression coefficients are mostly consistent with their counterparts based on ERA-20C data. But the regression of the NOAA 20CRv2 surface zonal wind in JAS against *G. bulloides* data does not show as significant relationship as using ERA-20C data.

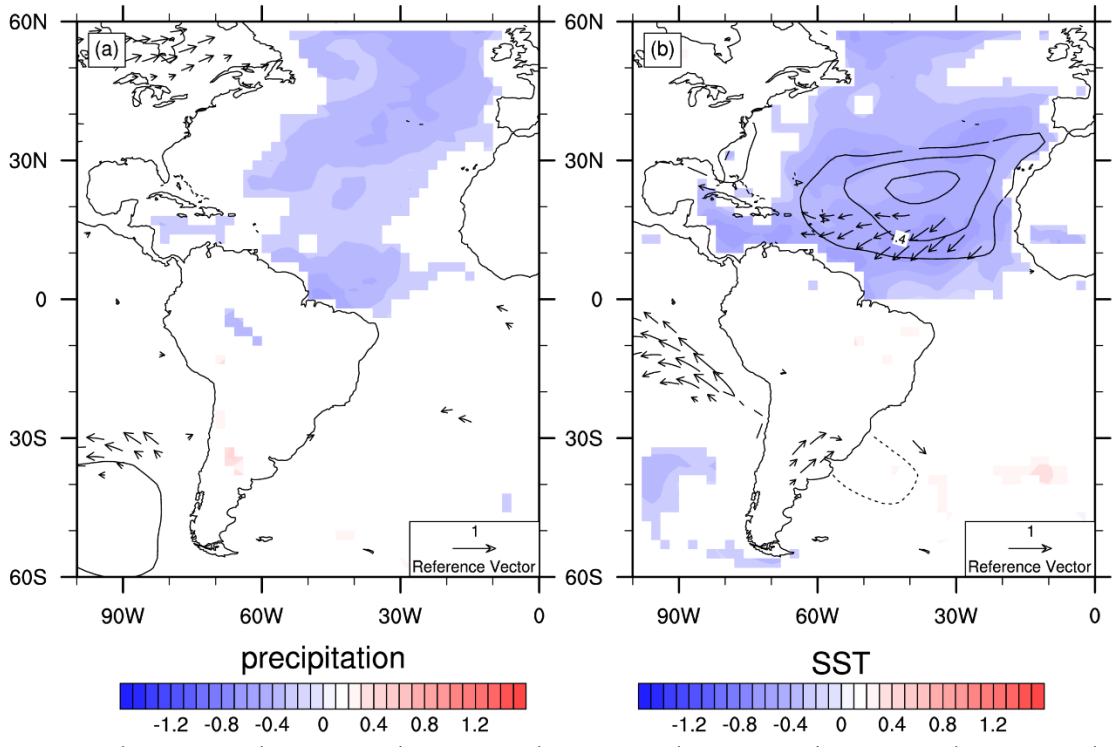

Figure 3-12. The same as Fig. 3-6 except for Data source: NOAA 20CRv2.

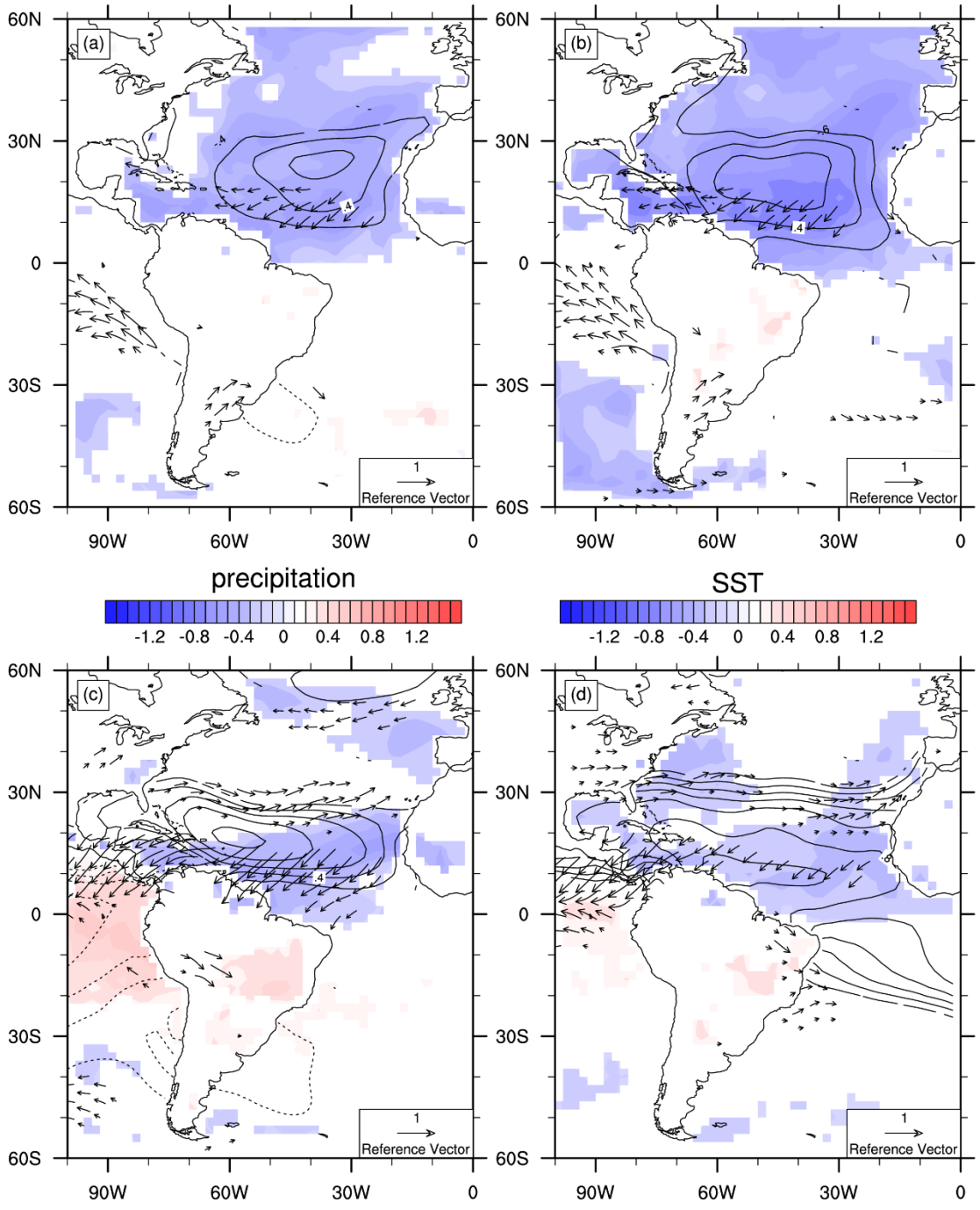

Figure 3-13. The same as Fig. 3-4 except for Data source: NOAA 20CRv2.

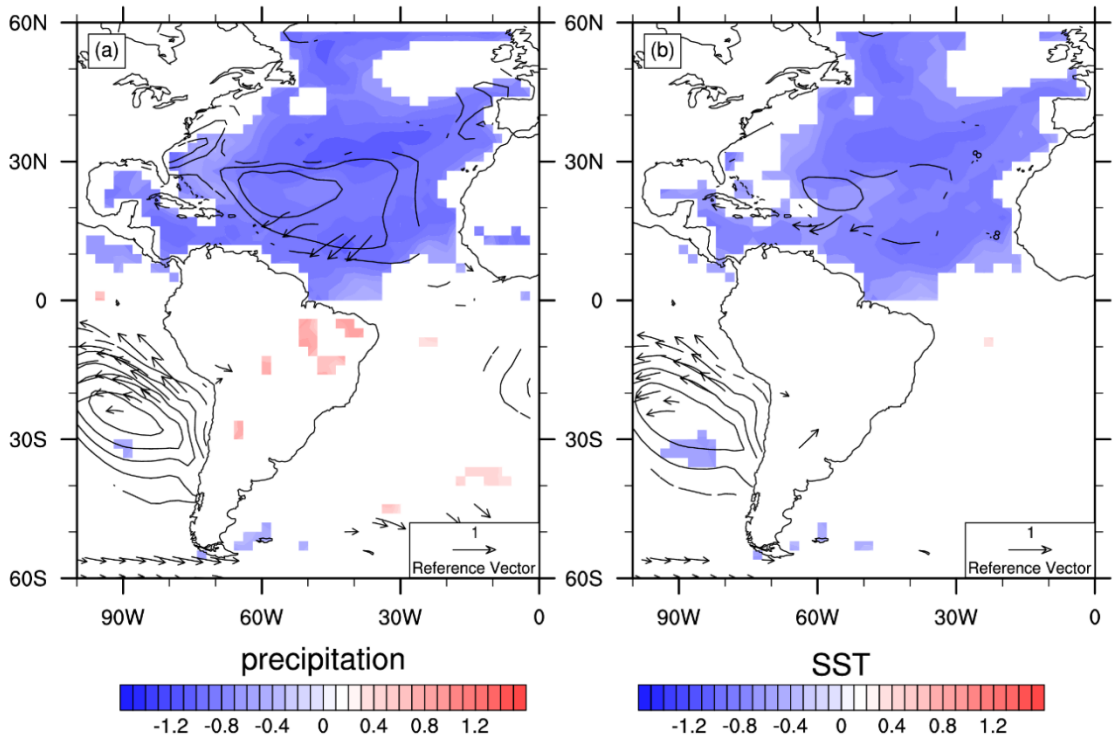

Figure 3-14. The same as Fig.3-8 except for Data source: NOAA 20CRv2.

To explore whether the discrepancy between the results based on ERA-20C and NOAA 20CRv2 surface wind data are from wind field uncertainty, and to find out which data is more reliable, a new generation reanalysis data, JRA-55, is applied to do the verification. This reanalysis is shorter than the previous two reanalysis data sets (55 year time coverage from 1958-2013) and has little overlap with the *G. bulloides* abundance data (33 years from 1958-1990). It is not suitable for the direct comparison with this proxy data, especially not for the low-frequency time series analyses. However, its advancement in observation assimilation can benefit the verification of the relationship between Cariaco Basin zonal wind and other variables, such as North Atlantic SST and SLP.

The largest difference between the two data sets shown above involves the relationship between low-frequency Cariaco Basin zonal wind with other variables. Firstly, we calculated the cross-correlation between this low-frequency local wind time series with filtered AMO index and Azores High pressure index, respectively, based on JRA-55 reanalysis data from 1958-2013. The results indicate that Cariaco Basin zonal wind is significantly correlated with both of these two variables.

Table 3-3. Cross-correlation coefficient between Cariaco Basin Coastal zonal wind and low frequent variabilities of annual mean AMO index (1958-2013), and Azores High pressure index (1958-2013) (r: correlation coefficient; p: p-value. Data are filtered by 15-point Lanczos filter). Data source: JRA-55.

	AMO	Azores High pressure
Zonal wind	r = 0.94, p = 0.008	r = -0.82, p = 0.03

As the JRA-55 data has too short common period with *G. bulloides* data, we reproduce Fig. 3-3 using JRA-55 data during 1958-2013, except for Fig. 3-3a. Comparing Fig. 3-16 (using JRA-55) to Fig. 3-3 (using ERA-20C), and Fig. 3-11 (using NOAA 20CRv2), we can see more resemblance between the results based on JRA-55 and ERA-20C. Especially for the regressions maps against Cariaco Basin zonal wind, both the Figures using JRA-55 (Fig. 3-15b) and using ERA-20C (Fig. 3-3c) indicate that stronger Cariaco coastal easterly wind is connected to colder North Atlantic SST, enhanced Azores High pressure, more intense easterly trade wind at Tropical North Atlantic, and decreased precipitation at Sahel region in Africa. In the meanwhile, the same plot using NOAA 20CRv2 does not show much information about this relationship (Fig. 3-11c). Based on these comparisons, we consider that above results based on ERA-20C data are validated and can be concluded upon.

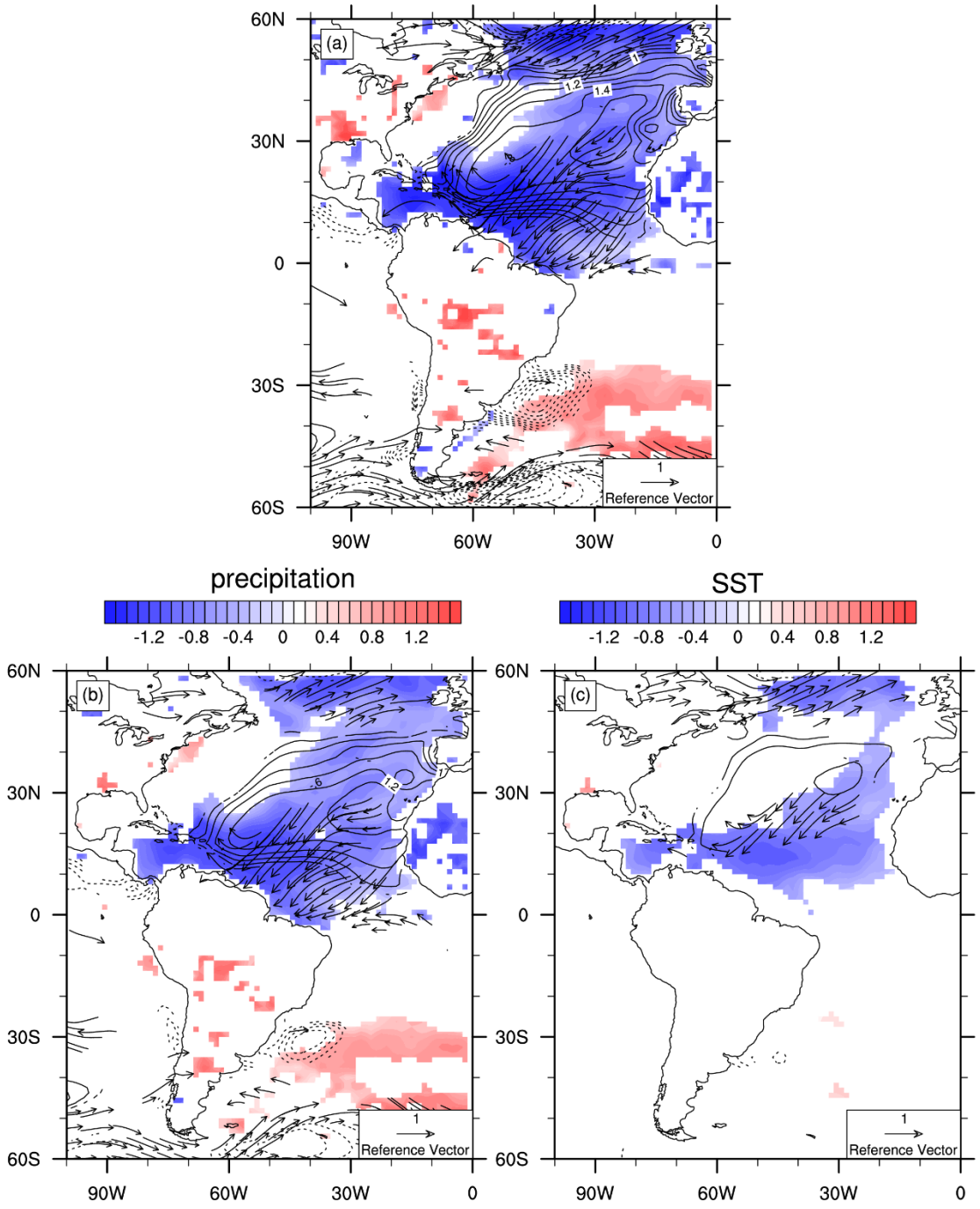

Figure 3-15. 1901-1990 de-trended standardized low-frequency (filtered by 15-point Lanczos filter) annual mean precipitation (color shades over land), SST (color shades over ocean), Sea level pressure (contours over ocean), and Surface wind (vectors) regression against de-trended standardized low-frequency annual mean (a) negative AMO index; (b) negative Cariaco Basin surface zonal wind (easterly wind); and (c) Azores High pressure index. Displayed values passed 95% significance level. Vectors are shown when regression of U-component passed 95% significance level. Contours with dashed lines. Data source: JRA-55.

3.4. Summary

We have shown that enhanced abundance of annual and low-frequency Cariaco Basin *G. bulloides* is associated with cooler North Atlantic SST, higher Azores High pressure south to 30°N, stronger tropical North Atlantic easterly trade winds and local easterlies over the Cariaco Basin, and less ITCZ rainfall in the Sahel. The local rainfall is not in favor of increasing Cariaco Basin *G. bulloides,* at the discussed time scales.

The relationships between these climate variables with AMO index bares large similarity with their counterparts with *G. bulloides* data, at both of the interannual and multidecadal time scales. Colder North Atlantic SST is associated to stronger low-latitude Azores High pressure, more intense Cariaco coastal surface easterly wind, less Sahel rainfall and more dust, and enhanced Tropical North Atlantic low level easterly winds which can bring dust from Africa to Cariaco Basin. Other than local watershed rainfall-impacted riverine inputs, both of the nutrients brought up by trade wind driven upwelling and Sahel dust transported by easterly wind are food sources for Cariaco Basin *G. bulloides* production. Thus, we conclude that the collective effect of the large circulation at North Atlantic can better explain the low-frequency variation of Cariaco Basin *G. bulloides*, and the *G. bulloides* abundance data can reflect the AMO variability during the past century.

Counterintuitively, the easterly wind variation in the summer/fall season shows large impacts on changes of *G. bulloides* abundance, despite the fact that both local trade winds and *G.*

bulloides production reach their peaks in winter/spring. The seasonal analysis is not to dwarf the effect of winter atmospheric circulation influence on Cariaco Basin *G. bulloides* abundance, but rather to highlight this proxy's connection with Sahel summer/fall rainfall and to suggest a possibility to compare this proxy with other summer/fall paleoclimate data, especially for SST reconstructions.

Thus, the strong association of the *G. bulloides* data with large-scale climate variability in the North Atlantic provides a basis for using the longer record of the *G. bulloides* data to study past climate change in the region. Our results also offer the spatial patterns of climate variability with which other proxy data of the North Atlantic SST or SLP can be compared and interpreted. The results of our paleoclimate data comparisons are shown in Chapter 4.

Chapter 4. Examine past millennium Atlantic Multidecadal Variabilities by putting Cariaco Basin *Globigerina bulloides* Abundance in the context of other paleoclimate data

4.1. Characteristics of the long-term *Globigerina bulloides* abundance data

In Chapter 3, we have found that *G. bulloides* abundance data can reflect multidecadal Atlantic variability (AMO) in the past century. However, in Black et al. [1999], spectral analysis of the whole eight century time series does not show significant variance corresponding to the frequencies associated multidecadal timescales. Before we study its multidecadal variability in the past in the context of other Atlantic proxy data, the characteristics of the *G. bulloides* abundance data is revisited.

Fig. 4-1 shows the wavelet analysis [*Torrence and Compo*, 1998] of annual *G. bulloides* abundance data. We can see multidecadal and lower frequency periods are active during most of the 800 years, though the 50-100 year periodicities are not considered significant. The longer periodicities around 250 year are persistent and significant. But we also need to treat them with caution, because they are largely out of the cone of influence. The variance of 50-100 year periodicities varies between 0.1-0.3, with three peaks around 1450, 1700, and 1900.

The spectral analysis of annual *G. bulloides* abundance data (Fig. 4-2) shows that its variance at low frequencies ($f < 0.07$ cycles/year, period > 14 years/cycle) is not significant.

Based on this analysis, we used 15-point low pass filter to filter out the high frequencies of the annual time series. This approach was used to highlight the multidecadal variabilities in the short observation and reanalysis data (in Chapter 3). However, in this chapter, long time series of proxy data are discussed and compared. Both of the annual and 10 year running mean time series will be presented for each paleoclimate data. And the Lanczos band pass filters will be applied on the low frequency time series comparisons [*Duchon*, 1979].

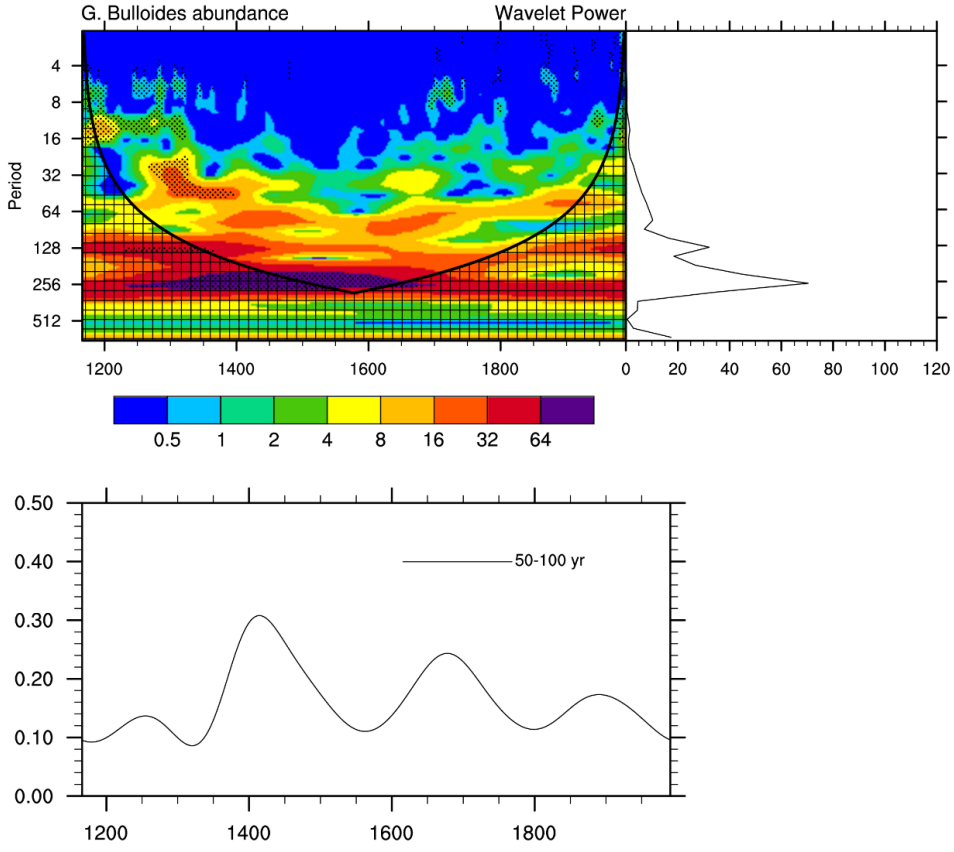

Figure 4-1. 1165-1990 (top) Morlet Wavelet analysis of G. bulloides abundance,(a) wavelet spectrum, x-axis is year, y-axis is period, (b) x-axis is wavelet spectrum, y is the same as (a); (bottom) year-variance plot of 50-100 year band pass filtered time series. Data are standardized before wavelet analyses. 95% significance regions are hatched.

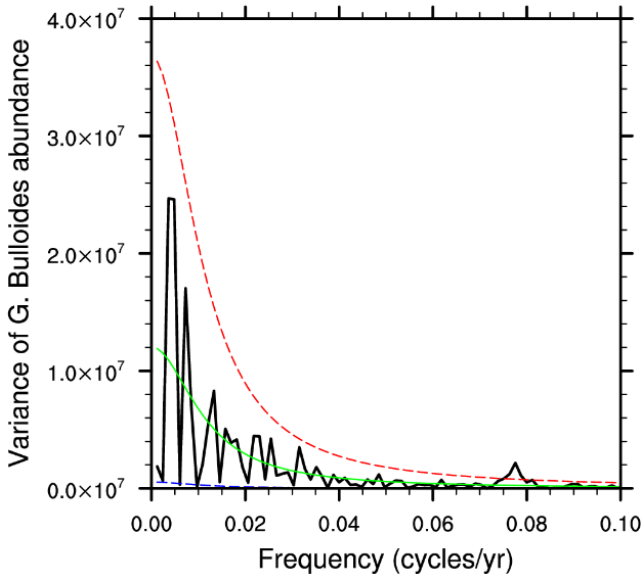

Figure 4-2. Spectral analysis of annual G. bulloides abundance data during 1165-1990; the green dashed line is the "red noise" curve, and the blue and red lines are the lower (p = 0.05) and upper (p = 0.95) confidence bounds, respectively.

4.2. Comparison of Cariaco Basin *Globigerina bulloides* Abundance with SST Reconstructions

As we are focusing on finding out the low-latitude AMV spatial characteristics in the past millennium, other North Atlantic SST proxies that recovered at a low-latitude location are needed. Based on the analyses in the previous chapter, our location choice can be as far east as to the coast of Western Africa. Thus, we chose a paleoclimate data that can expand our spatial coverage there. In Fig. 4-3, we compare the original and filtered time series of *G. bulloides* abundance, Eastern Tropical Atlantic SST reconstruction based on *G. ruber* (p) Mg/Ca ratio [*Kuhnert and Mulitza*, 2011], and instrumental AMO index. As in the previous chapter we find

that multidecadal variability of *G. bulloides* abundance is able to reflect the AMO in the past century, with larger *G. bulloides* abundance corresponding to cooler North Atlantic SST. Thus, in this comparison, we reversed the Y axes of the SST proxy and AMO index.

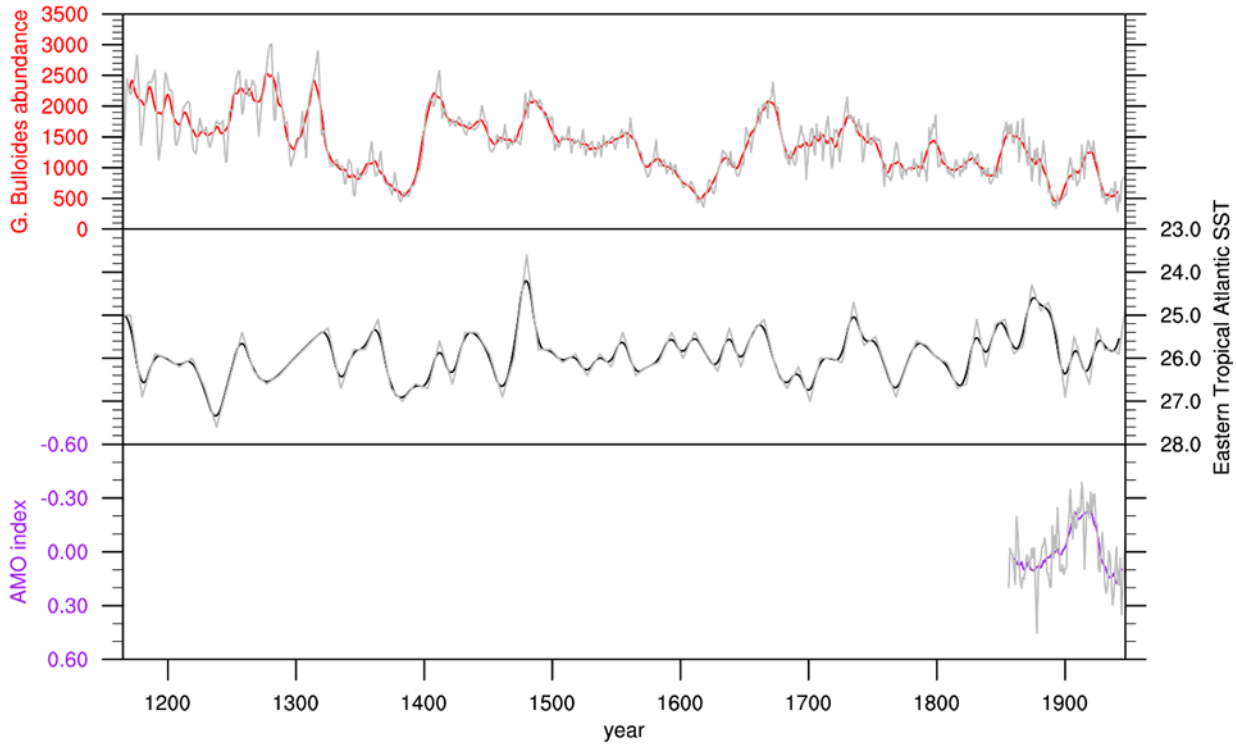

Figure 4-3. 1165-1990 original data (gray) and 10 year running averages of interpolated annual mean data (other colors) of G. bulloides abundance (red), Eastern Tropical Atlantic G. ruber (pink) Mg/Ca SST (black, Y axis reversed, unit °C), and 1856-1990 instrumental AMO index (purple, Y axis reversed).

The spectral analysis of this proxy during 1165-1990, the common period with *G. bulloides* abundance data, display significant multidecadal variance (Fig. 4-4 left). The spectral coherence between it and *G. bulloides* abundance also show significant peak at frequencies that associated with multidecadal timescales (Fig 4-4 right).

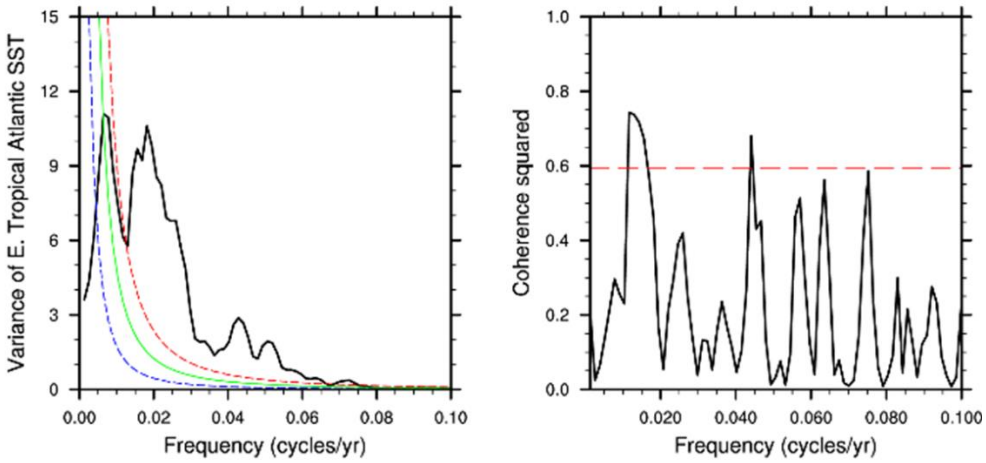

Figure 4-4. (Left) Spectral analysis of Easter Tropical Atlantic G. ruber (pink) SST during 1165-1990; the green dashed line is the "red noise" curve, and the blue and red lines are the lower (p = 0.05) and upper (p = 0.95) confidence bounds, respectively. (Right) The coherence-squared value between this SST proxy and G. bulloides abundance data during the same period; the red line indicates the critical coherence squared-value corresponding to the 95% significance level.

The wavelet analysis shows that spectral power in the multidecadal band is significant over several time intervals during the past centuries (Fig. 4-5). It may imply the AMO's signal in the local SST. The variance of 50-100 year periodicities varies between 0.1-0.4, also with three peaks around 1450, 1700, and 1900, which is similar to the analysis of *G. bulloides* abundance in Fig. 4-1.

Comparison of *G. bulloides* abundance and Eastern Tropical Atlantic Mg/Ca SST proxy indicates they have significant correlation at multidecadal timescales, shown by the 50-100 year band pass filtered time series (Fig. 4-6). The correlation coefficient is -0.53 and p-value is 0.001. In Fig. 4-6 (bottom), we can see that the two time series closely covariate with each other, except

for short periods during 1400-1450 and 1800-1900. The lag-correlation between these two filtered data (Fig. 4-7) shows that when the SST reconstruction data leads for three years, the correlation reaches its maximum absolute value. Considering age model uncertainties, these two times series are considered to be almost concurrent.

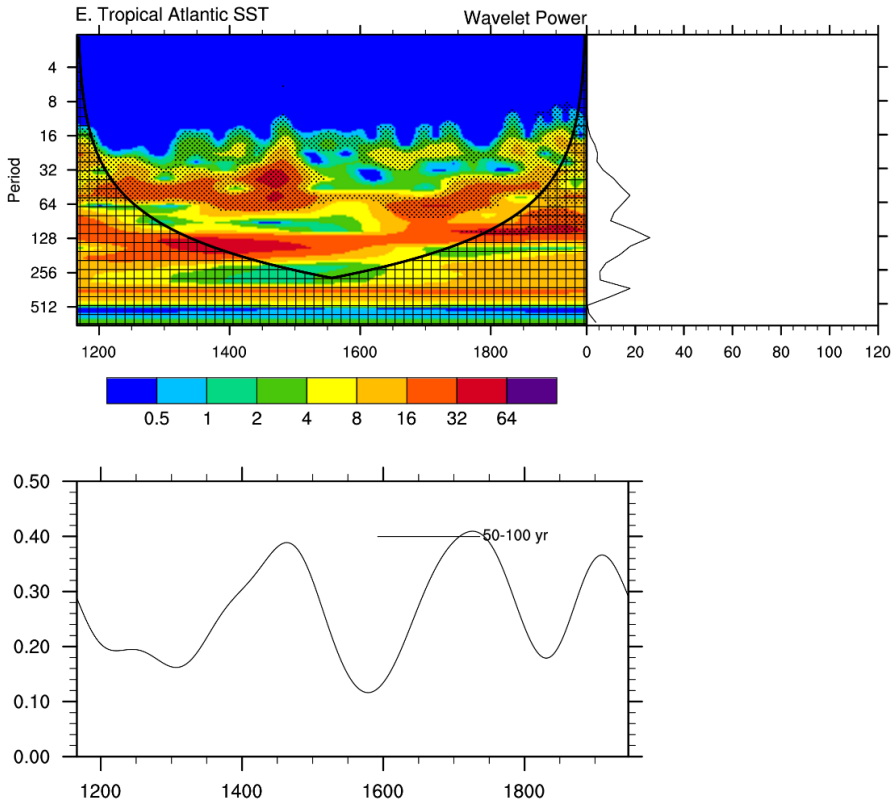

Figure 4-5. Same as Fig. 4-1 except using 1165-1947 Easter Tropical Atlantic G. ruber (pink) SST

These two proxies are based on different locations, species (with peak production at different seasons), and are developed independently using different marine sediments and method. In addition, the average uncertainty of the age model of the SST proxy is ± 11 year during this period, and age model uncertainty can reach 60 years at the oldest part of *G. bulloides*

abundance data. Considering these factors, the multidecadal variability of these two time series are showing surprising consistency with each other, and strongly suggests that they are influenced by similar process at this timescale. It is possible the relationship of *G. bulloides* abundance and AMO we see in the past century is persistent during the past eight centuries, thus it contains the AMO signal in its whole time series; and the SST proxy recorded the AMO variations during this period of time at a tropical latitude.

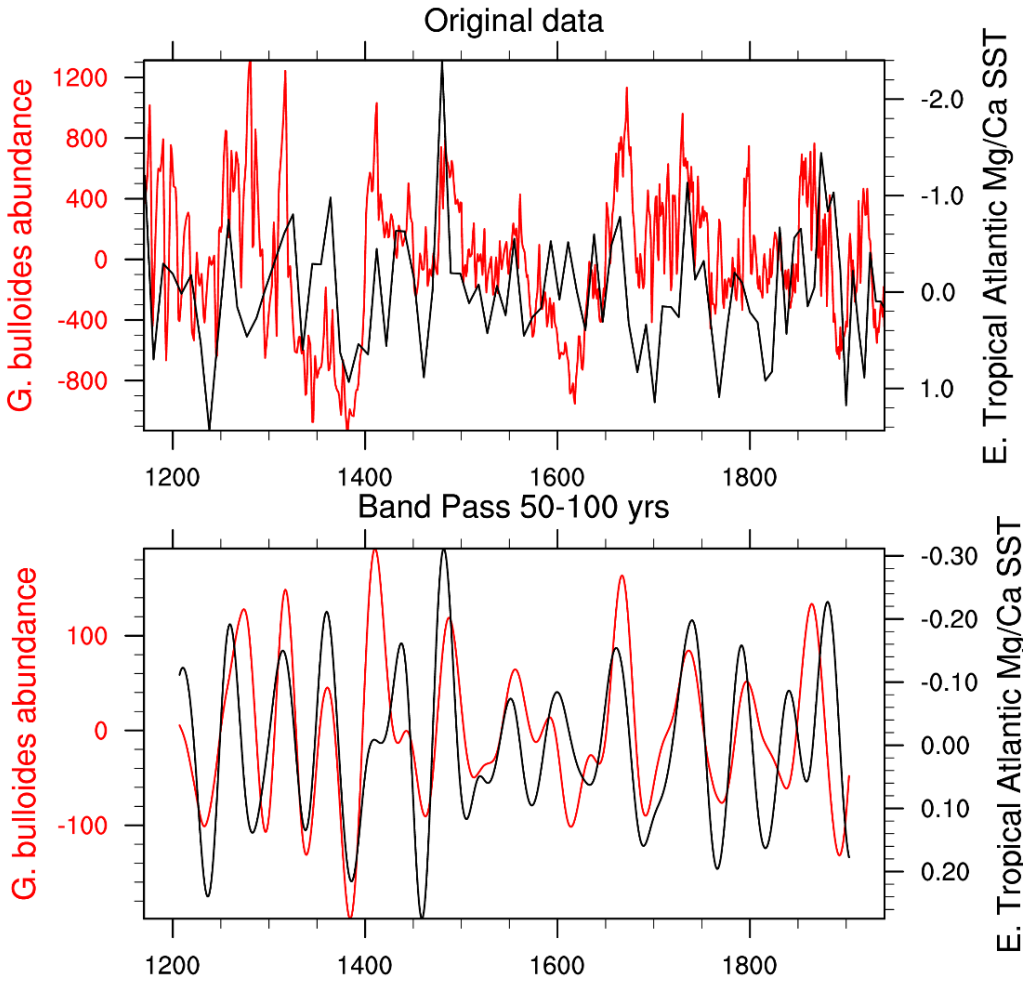

Figure 4-6. Comparison of G. bulloides abundance (red) and Eastern Tropical Atlantic Mg/Ca SST (black, Y-axis reversed) with (upper) original time series, (lower) time series filtered by 50-100 years band pass filter.

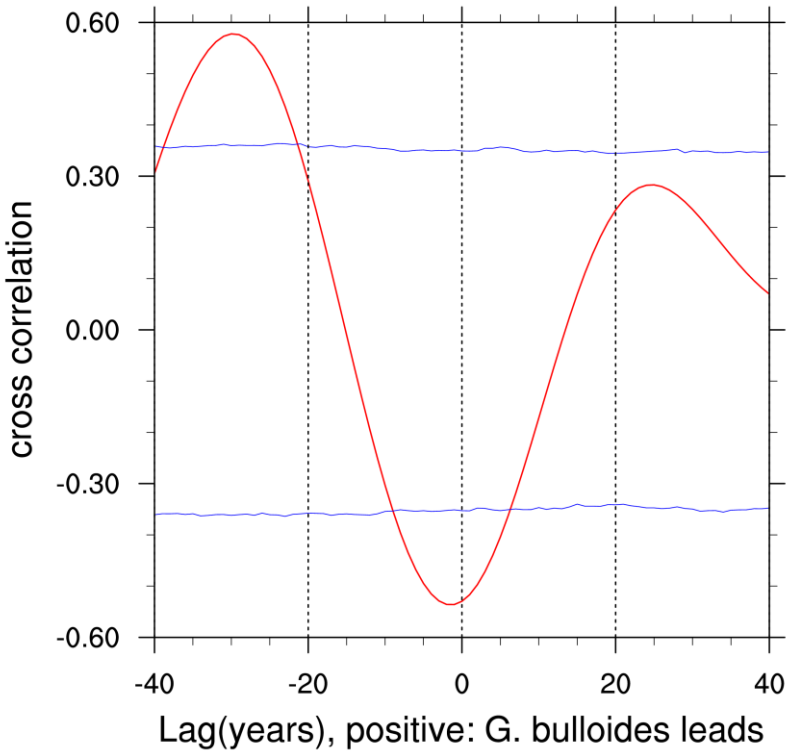

Figure 4-7. Lag-correlation of filtered G. bulloides abundance and Eastern Tropical Atlantic Mg/Ca SST (red). Data filtered by 50-100 years band pass filter. Positive value of X-axis indicates that G. bulloides abundance leads the SST reconstruction data. Blue lines indicate the interval of the 95% significance level.

We have also selected another SST proxy data, which located to the north of Cariaco Basin, to the south shore of Puerto Rico. Hence, the three proxy data together cover a large area of tropical North Atlantic both zonally and meridionally. In Fig. 4-8, we compare the original (annual) and filtered time series of *G. bulloides* abundance, Puerto Rico coral Sr/Ca ratio (SST index) and $\delta^{18}O$ (SST-SSS index) [*Kilbourne et al.*, 2008], and instrumental AMO index. As mentioned in the data description, larger values of Sr/Ca indicate lower SST, and larger values (less negative) of $\delta^{18}O$ corresponds to lower SST and higher SSS.

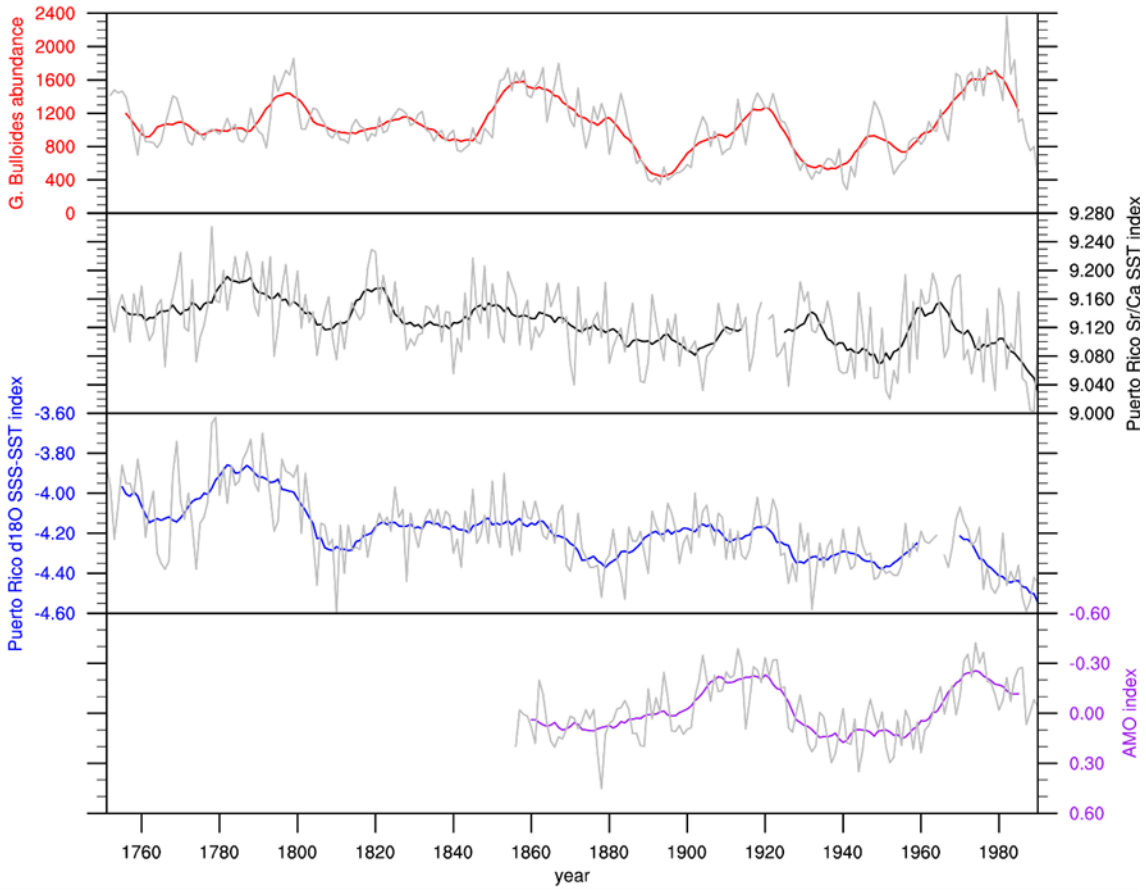

Figure 4-8. 1751-1990 original data (gray) and 10 year running averages (other colors) of G. bulloides abundance (red), Puerto Rico Sr/Ca SST (black), Puerto Rico $\delta^{18}O$ SST-SSS index (blue), and 1856-1990 instrumental AMO index (purple, Y axis reversed)

The wavelet analysis of annual Sr/Ca time series shows that spectral power in the multidecadal band (50-100 years period) is not significant inside the cone of influence (Fig. 4-9). The variance of 50-100 year periodicities is consistently below 0.15.

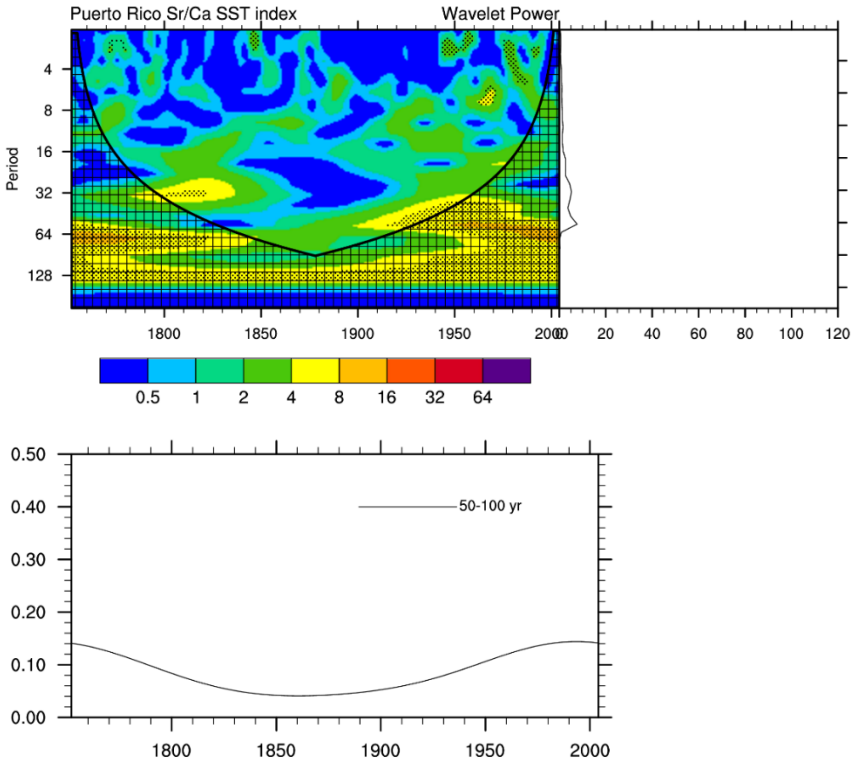

Figure 4-9. Same as Fig. 4-1 except using 1751-2004 Puerto Rico Sr/Ca SST index

Nevertheless, the same analysis of annual $\delta^{18}O$ time series indicates that spectral power in its multidecadal band (50-100 years period) is persistently significant through the whole study period (Fig. 4-10). The variance of 50-100 year periodicities is around 0.15-0.27.

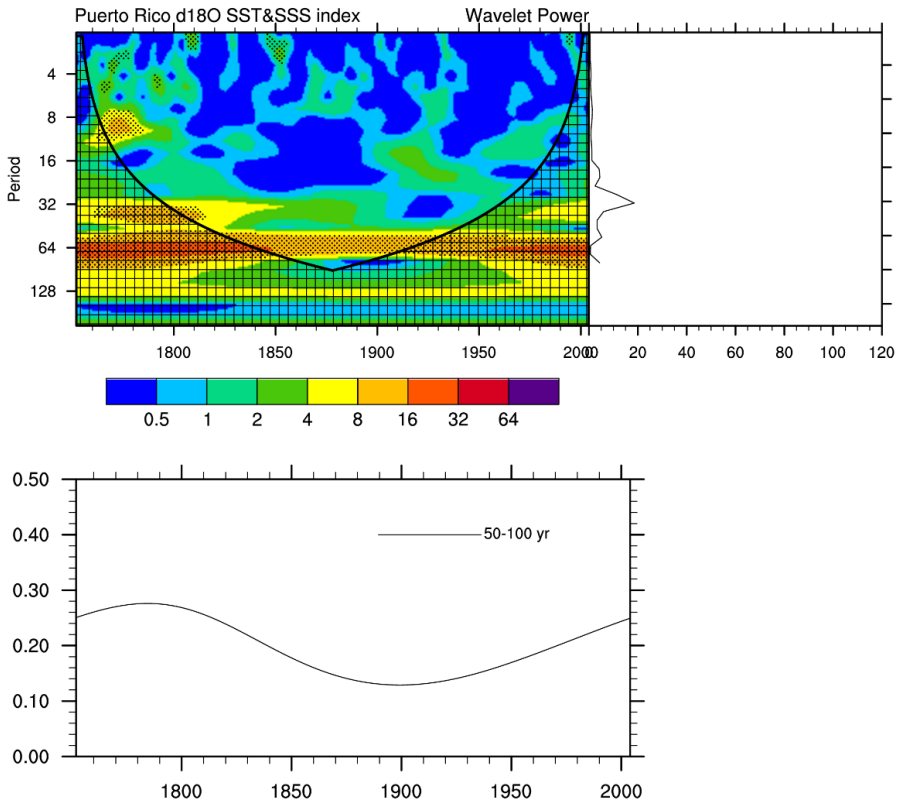

Figure 4-10. Same as Fig. 4-1 except using 1751-2004 Puerto Rico $\delta^{18}O$ SST-SSS index

Comparison of *G. bulloides* abundance and annual Sr/Ca time series indicates they have significant correlation at multidecadal timescales, shown by the 50-100 year band pass filtered time series (Fig. 4-11). In Fig. 4-11 (bottom), we can see that larger *G. bulloides* abundance associates with larger Sr/Ca ratio, which represents lower Puerto Rico SST ($r = -0.77$, $p = 0.04$). This is consistent with the relationship we find between *G. bulloides* abundance with AMO index. The lag-correlation between these two filtered data (Fig. 4-12) indicates that when the *G. bulloides* abundance data leads for two years, the correlation reaches its maximum value near the zero-lag. The age model uncertainty of Sr/Ca SST index is ± 1 year at most. The two filtered time series are also considered almost concurrent based on the age model uncertainties of both of the two data.

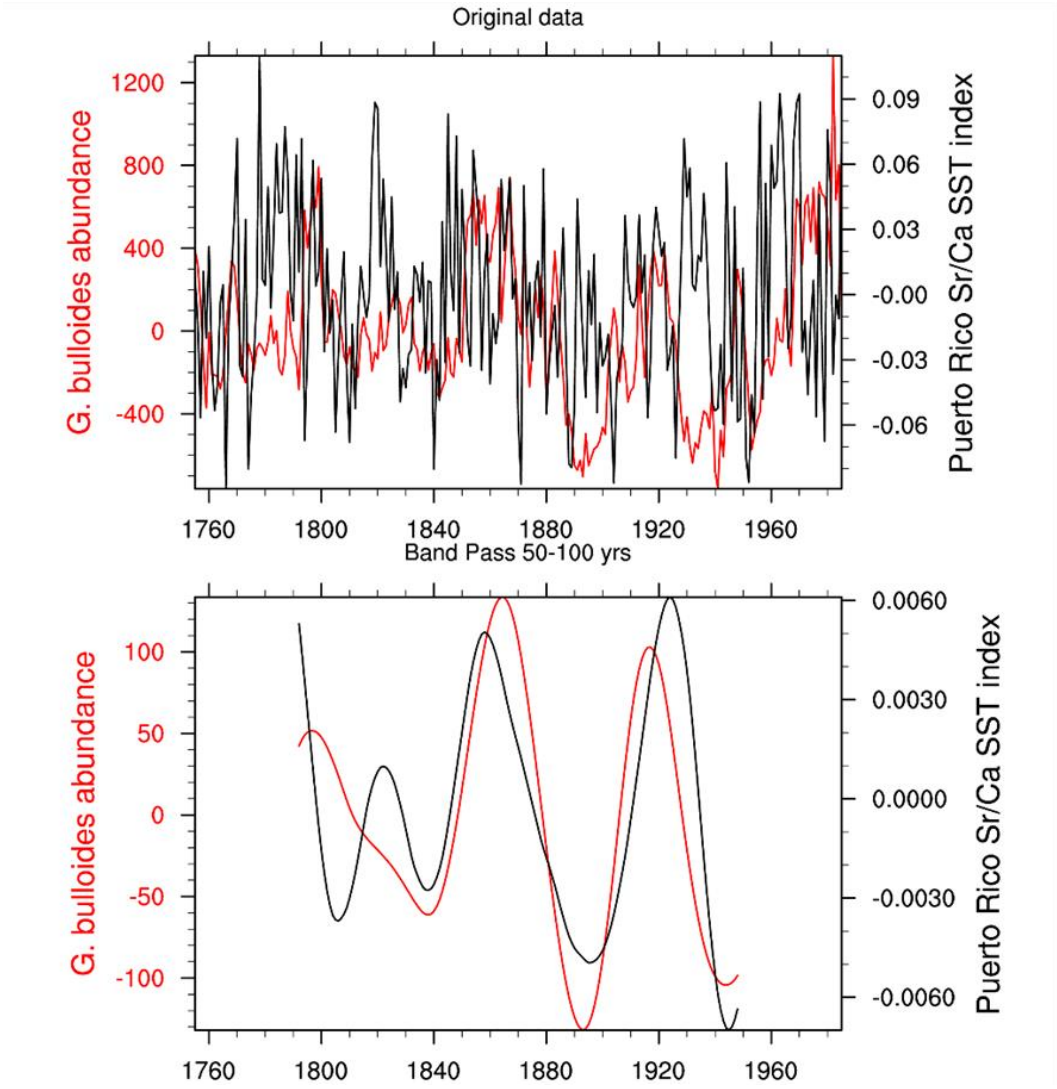

Figure 4-11. Comparison of G. bulloides abundance (red) and Puerto Rico Sr/Ca SST index (black) with (upper) original time series, (lower) time series filtered by 50-100 years band pass filter.

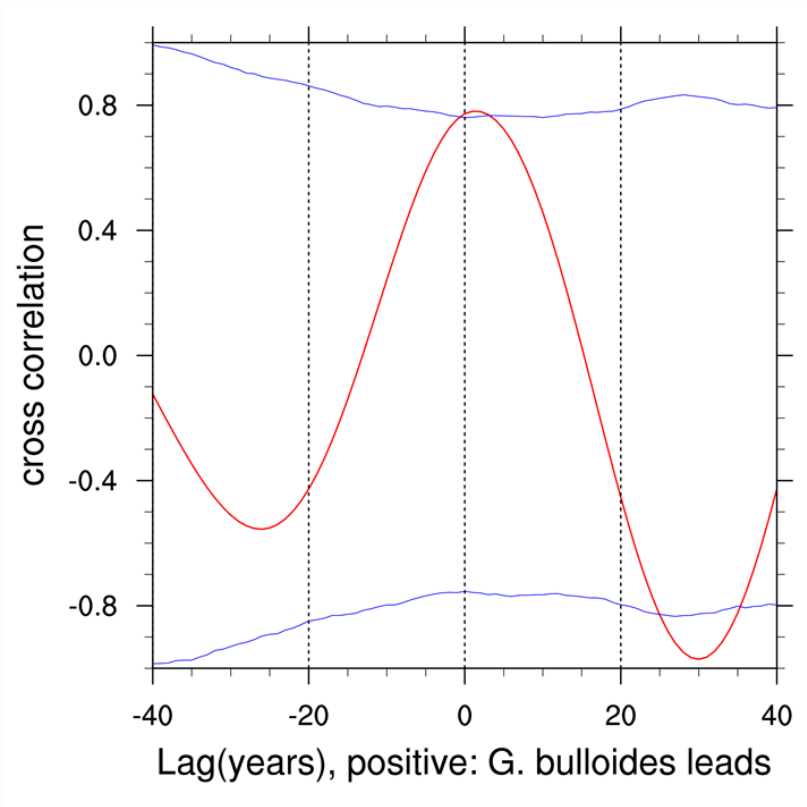

Figure 4-12. Same as Figure 4-7, except between 50-100 years band pass filtered G. bulloides abundance and Puerto Rico Sr/Ca SST index.

However, the same comparison of *G. bulloides* abundance and annual $\delta^{18}O$ time series does not show this relationship (Fig. 4-13). Fig. 4-13 (bottom) indicates a shift between the two low-frequency time series. As $\delta^{18}O$ does not only contain SST signal, but also SSS information, the relationship *G. bulloides* abundance data and SST at this timescale may not be easily separated using this proxy. In *Kilbourne et al.* [2008], these two time series are compared under the proposed mechanism that stronger trade wind drives more fresh water to Puerto Rico and larger $\delta^{18}O$. Thus, peaks of $\delta^{18}O$ are associated with increasing periods of *G. bulloides* abundance. This relationship is also confirmed by the lag-correlation analysis of the filtered data (Fig. 4-14). When *G. bulloides* abundance data leads for 17 years, their correlation reaches the

maximum absolute value but is still not significant. Based on our analysis in Chapter 3, higher *G. bulloides* abundance corresponds to cooler North Atlantic SST (including SST south to Puerto Rico), and thus lower $\delta^{18}O$. Thus, *G. bulloides* abundance has potential to reflect the Peurto Rico SST and SSS in opposite directions in terms of contributing to $\delta^{18}O$ values. This is why the relationship between *G. bulloides* abundance and $\delta^{18}O$ is hard to interpret only by the influence of trade wind on SSS.

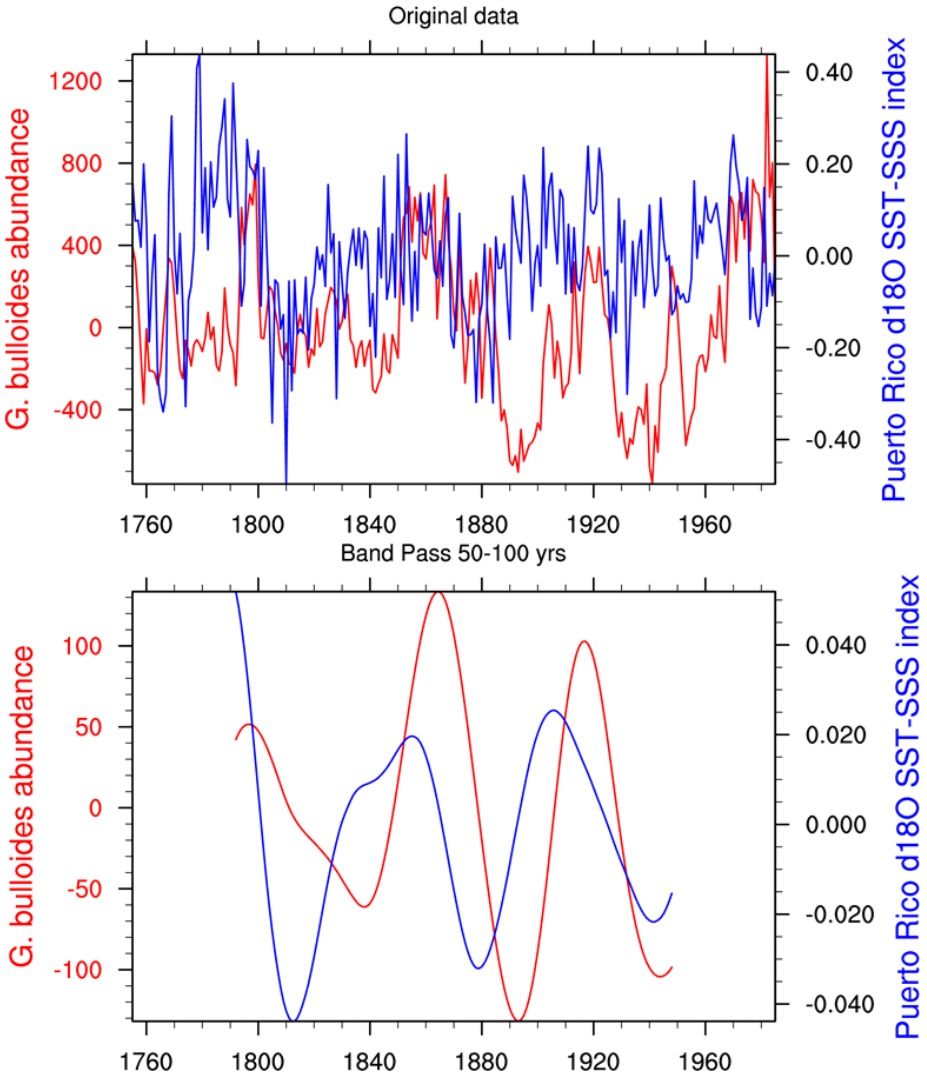

Figure 4-13. Comparison of G. bulloides abundance (red) and Puerto Rico $\delta^{18}O$ SST-SSS index (black) with (upper) original time series, (lower) time series filtered by 50-100 years band pass filter.

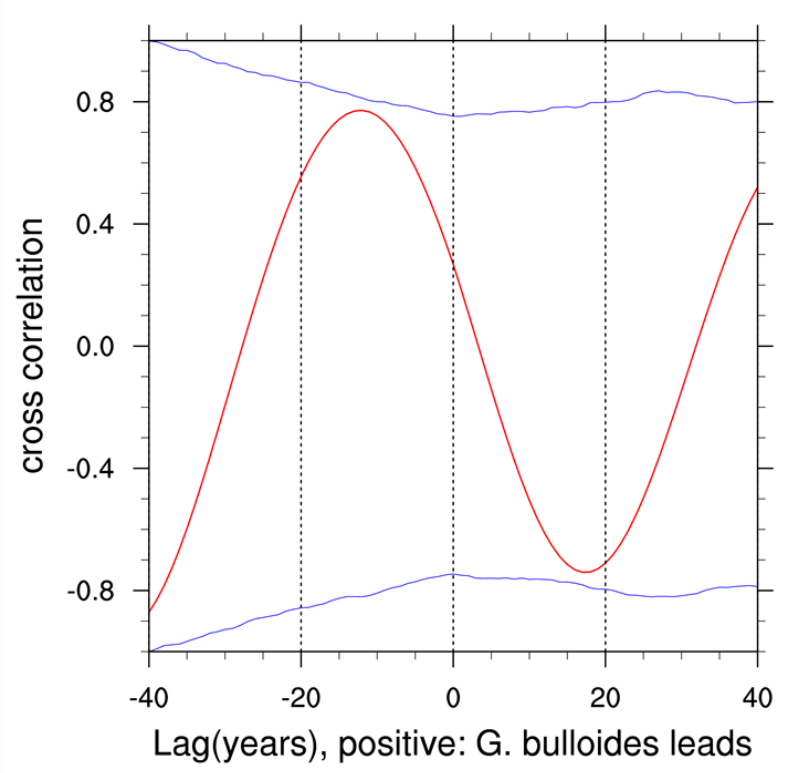

Figure 4-14. Same as Figure 4-7, except between 50-100 years band pass filtered G. bulloides abundance and Puerto Rico $\delta^{18}O$ SST-SSS index.

4.3. Compare *Globigerina bulloides* abundance with North Atlantic Oscillation Reconstructions

4.3.1. Mechanism of AMO and Multidecadal NAO-AMO relationship

The AMO is a basin-wide North Atlantic SST variability characterized by an alteration of prolonged warm phases and cold phases on multidecadal timescales [*Schlesinger and Ramankutty*, 1994; *Enfield et al.*, 2001]. The mechanisms of the persistence and switch of the warm and cold phases in AMO have been studied in previous studies. One of the most important

mechanism is that the AMO is associated with variations of the Atlantic Meridional Overturning Circulation (AMOC), the North Atlantic branch of the Thermohaline Circulation (THC) [*Delworth and Mann*, 2000; *Knight et al.*, 2005]. Anomalous meridional heat transport by a stronger AMOC to North Atlantic surface and subsurface will build up the heat there and warm up the North Atlantic SST, leading to warm phase of the AMO. Warm SST anomalies also reduces the strength of the trade winds in the tropics and North Atlantic westerlies in the mid-latitudes, surpresses surface evaporative cooling, and thus sustain the warm phase through a positive feedback (WES: Wind-Evaporation-SST feedback) [*Xie*, 1999].

The North Atlantic Oscillation (NAO) is the dominant North Atlantic variability characterized by the fluctuations of the winter SLP difference between the Azores High and Icelandic Low [*Hurrell*, 1995]. The positive phase of NAO is associated with a larger pressure difference between the two pressure centers and stronger westerlies in the mid-latitude. And during the negative phase of NAO, westerlies are reduced.

Previous studies suggest that multidecadal variabilities of NAO has close association with AMO [*Marshall*, 2001]. The positive phases of the NAO coincide with the negative phases of the AMO, with several years of lag-lead [*Robertson et al.*, 2000; *Li et al.*, 2013].

The NAO structure depends on meridional SLP and SST gradient on the North Atlantic Ocean. In the warm phase of AMO, the horseshoe pattern of SST anomalies warms higher latitude and eastern North Atlantic, but cool the SST in the mid-latitude western North Atlantic.

Thus, the SLP and SST gradient weakens and the NAO will switch to negtive phase [*Robertson et al.*, 2000; *Zhang and Vallis*, 2006].

In the other hand, low-frequency NAO is also found to have significant impacts on the AMOC and AMO. The AMOC is driven by the sinking of dense water in the higher latitudes of the North Atlantic, forming North Atlantic Deep Water (NADW). The NAO can alter convection at Labrador Sea, which is critical in NADW formation, and in turn influece the AMOC and lead the AMO [*Latif et al.*, 2006a, 2006b; *Li et al.*, 2013].

Although the lead-lag years and/or mechanisms are not consistent among the previous studies, the opposite-sign relationship between the multidecadal variabilities of NAO and AMO are agreed upon. As we have established the relationship between Cariaco Basin *G. bulloides* abundance and the AMO, we would like to compare this paleoclimate data with NAO reconstructions based on the NAO-AMO antiphase relationship.

4.3.2. Relationship between *G. bulloides* abundance and NAO reconstructions

Firstly, we investigated the relationship between *G. bulloides* and NAO using the reconstruction of NAO index derived from Bermuda winter SST based on coral Sr/Ca [*Goodkin et al.*, 2008a]. This NAO reconstruction covers 1793-1988, largely overlapped the *G. bulloides* abundance data and instrumental climate indices. This data set is recovered at a relatively low latitude as an NAO index. However, as it is partly constructed based on the relationship between multidecadal variability of NAO and Bermuda winter SST, this data is considered ideal in a study of multidecadal variabilities.

In Fig. 4-15, we compare the original (annual) and filtered time series of *G. bulloides* abundance, reconstruction of NAO in *Goodkin et al.* [2008a], AMO index, and Hurrell's NAO index. Hurrell's NAO index is defined as difference of normalized annual SLP between two stations, one near the Azores and another near Iceland [Hurrell, 1995]. The NAO reconstruction is shown to be able to capture the low-frequency variability of instrumental NAO index. And this proxy bears large resemblance with the *G. bulloides* abundance data. The two time series will be compared to show if they can reflect the relationship between multidecadal NAO and AMO variabilities.

The wavelet analysis of annual NAO reconstruction time series shows that spectral power in the multidecadal band (50-100 years period) is significant through the whole period. However,

due to the shortness of the data, most of it is outside of the cone of influence (Fig. 4-16). The variance of 50-100 year periodicities is between 0.2-0.35, with the largest value being near 1890.

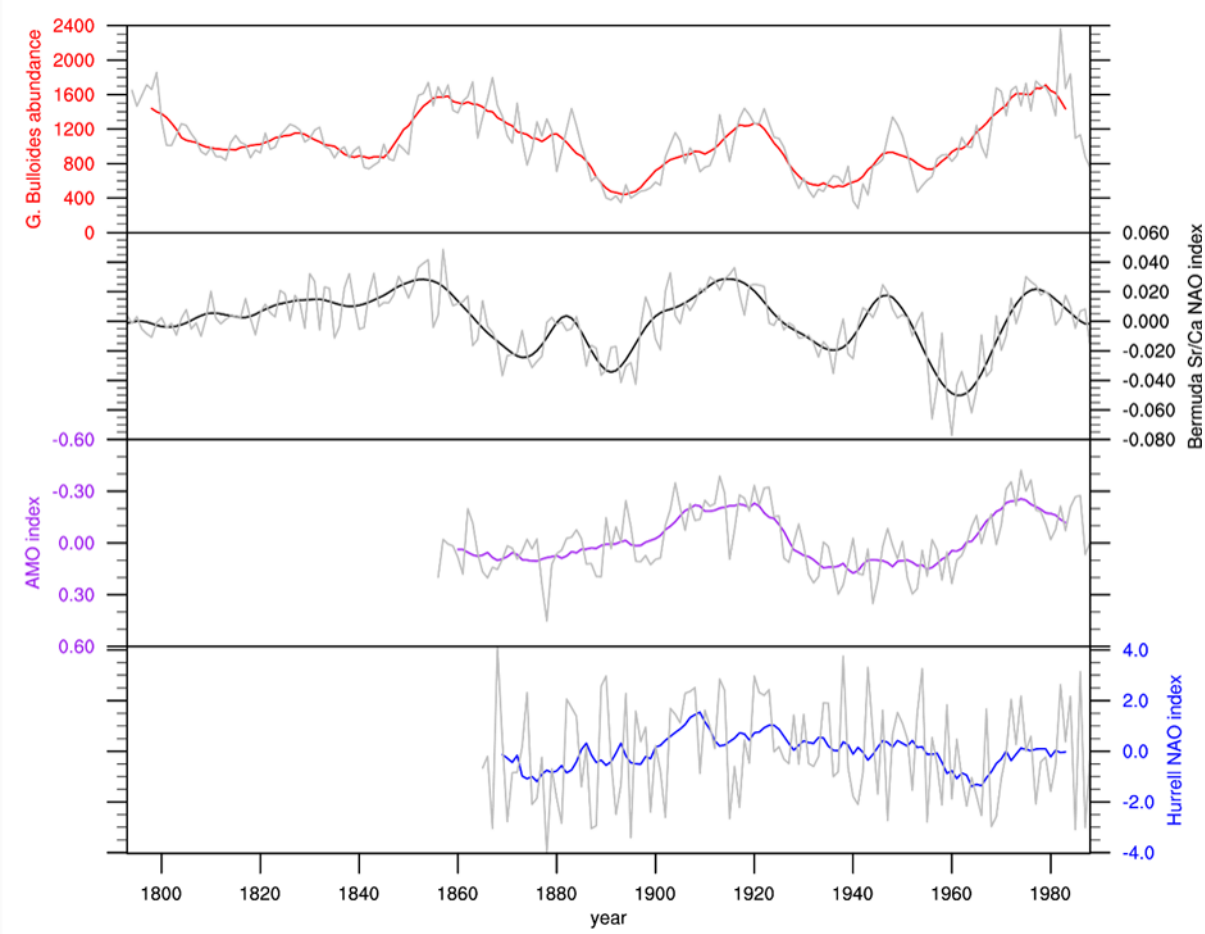

Figure 4-15. Original data (gray) and 10 year running averages (purple and blue) of 1751-1990 G. bulloides abundance (red), 1856-1990 instrumental AMO index (purple, Y axis reversed), and 1865-1990 instrumental Hurrell NAO index (blue). Black line is the 20-100 year Bermuda Sr/Ca NAO index (flipped sign), overlaid by the combined NAO index (gray) during 1751-1990.

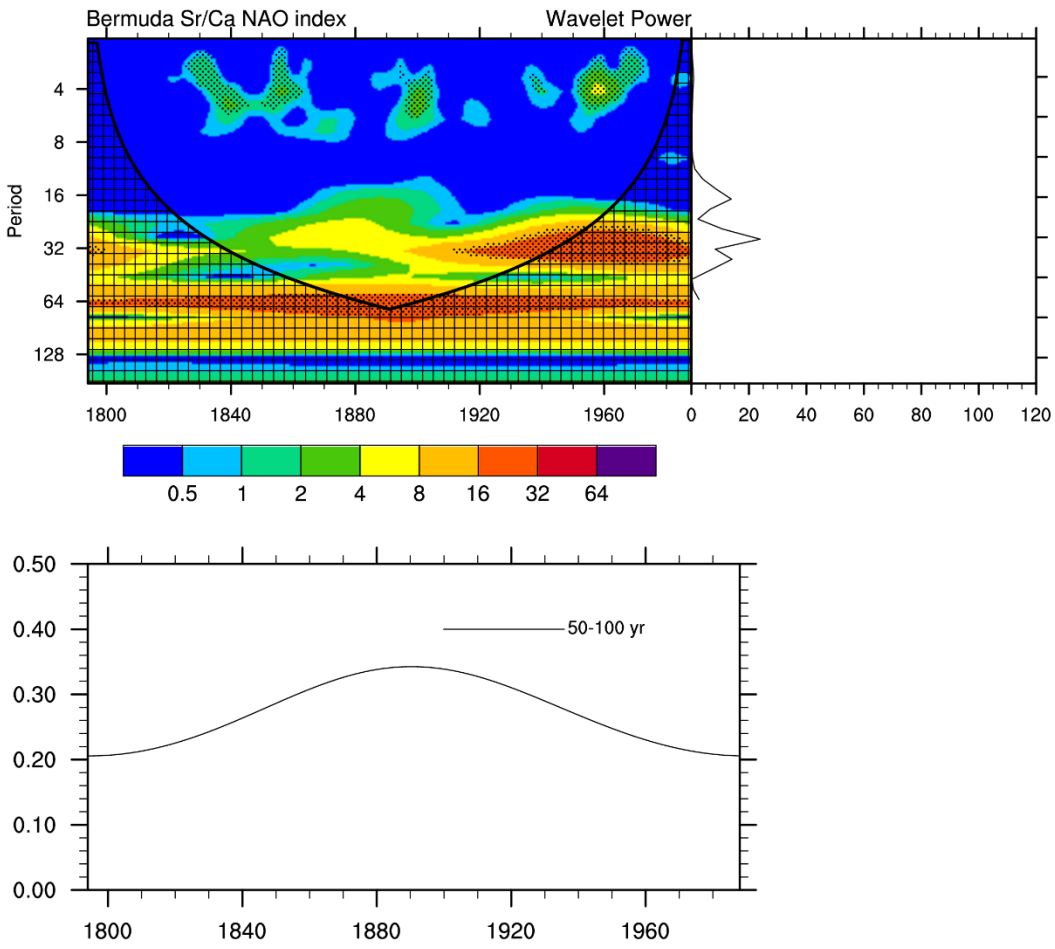

Figure 4-16. Same as Fig. 4-1 except using 1793-1988 Bermuda Sr/Ca winter SST proxy of NAO index

Comparison of *G. bulloides* abundance and NAO reconstruction time series indicates they have barely significant correlation at multidecadal timescales, with slight shift (Figs. 4-17, 4-18). We can see that the two time series in Fig. 4-17 (bottom) demonstrate a seemingly in-phase relationship between the two filtered time series, consistent with the antiphase relationship between multidecadal NAO and AMO. However, the lag-correlation analysis between them (Fig. 4-18) shows that when the NAO reconstruction leads for 9 years, the correlation between them reaches maximum value (r = 0.86), which implies that positive NAO leads negative AMO for

about a decade. To further investigate the relationship displayed in paleoclimate data, we included the comparison with Luterbacher's NAO reconstruction *Luterbacher* [2002].

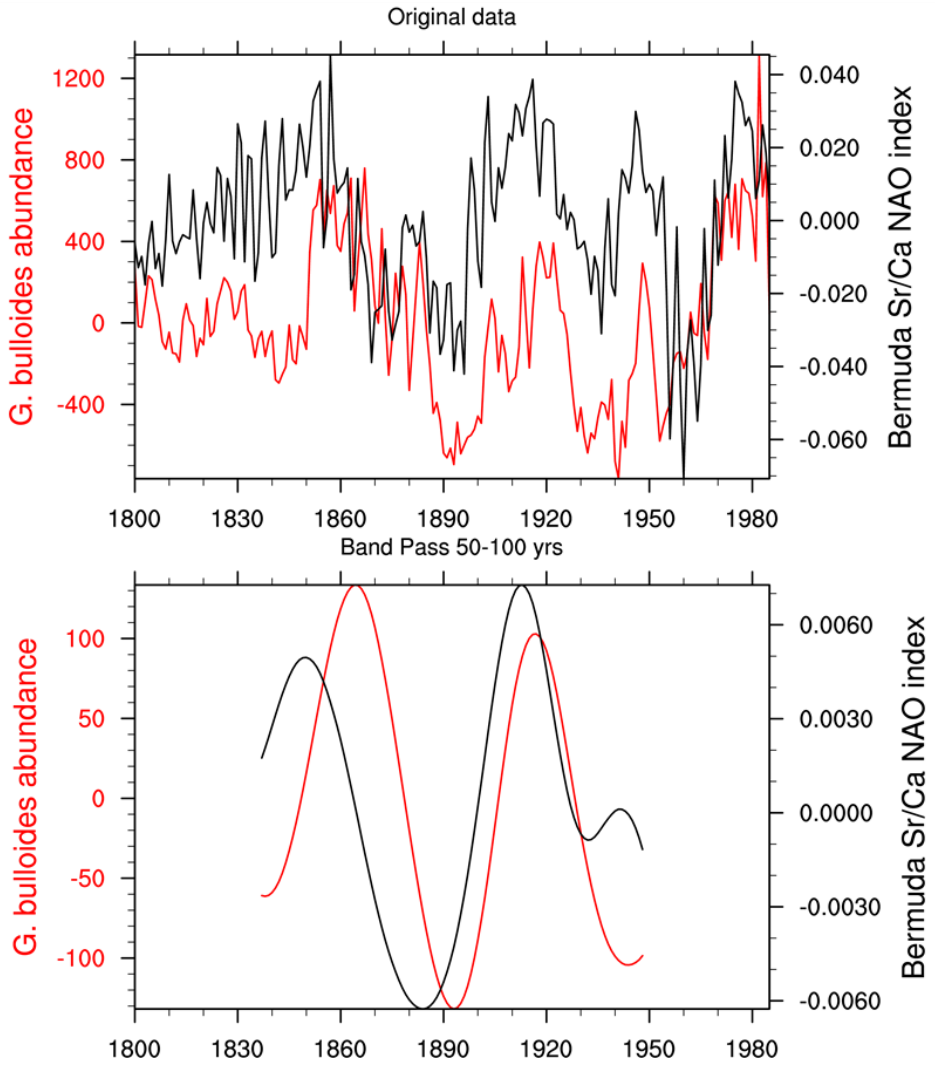

Figure 4-17. Comparison of G. bulloides abundance (red) and Bermuda Sr/Ca winter SST NAO index (black) with (upper) original time series, (lower) time series filtered by 50-100 years band pass filter.

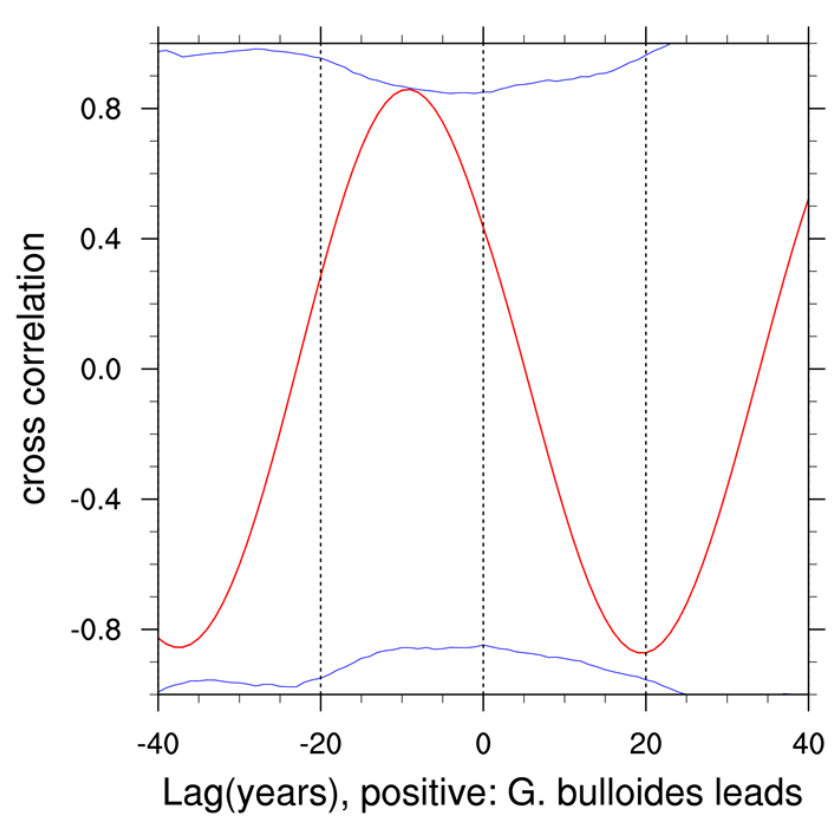

Figure 4-18. Same as Figure 4-7, except between 60-80 year band pass filtered G. bulloides abundance and Bermuda NAO reconstruction data.

Luterbacher [2002] extended earlier studies and reconstructed a monthly NAO index for 1659-2000 and seasonal NAO index for 1500-1658. We only calculate winter NAO and annual NAO index from their reconstruction and compare with relevant instrumental and paleoclimate data. This data has been used in many other research on NAO. Including it in our comparison may provide us opportunities to verify our results with other studies.

Shown in the Fig. 4-19 are 20 years running averages of all the data, except for NAO reconstruction from *Goodkin et al.* [2008a]. As *Goodkin et al.* [2008a] provided the 20-100 year NAO index, we use it directly as the low-frequency time series. The multidecadal NAO index

has an antiphase relationship with Bermuda SST, the Y-axis of this time series is reversed. Both of the winter and annual index are consistent with the *Goodkin et al.* [2008a] reconstruction and instrumental Hurrell NAO index during their common period, with winter index bearing more resemblance with *Goodkin et al.* [2008a] reconstruction.

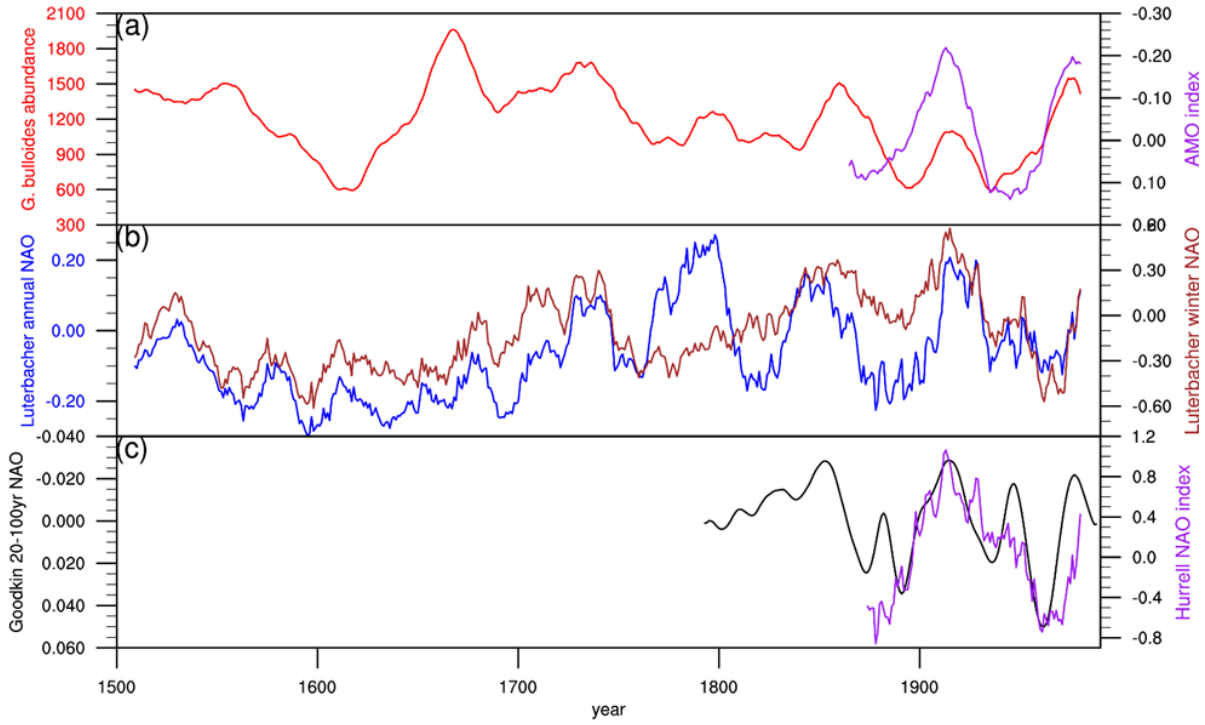

Figure 4-19. (a) 20 year running averages of 1500-1990 G. bulloides abundance (red) and 1856-1900 AMO index (purple, Y axis reversed); (b) 20 year running averages of annual NAO (blue) and winter NAO reconstruction (brown) in Luterbacher et al. [2002]; (c) 20-100 year NAO reconstruction in Goodkin et al. [2008] (black, Y axis reversed) and 20 year running averages of 1865-1990 Hurrell NAO index (purple)

As mentioned in the data description of this NAO reconstruction, the winter NAO index was shown to have the least uncertainties during the whole period. As meaningful estimates of NAO start in the 1720s for spring, summer, and autumn, the annual mean NAO index is also considered usable only after 1720s.

Also, as the data consists of two sections with different time resolution, there might be inconsistency between the two sections, such as in the magnitude and/or variance. In Fig. 4-19b, we can see that the time series for both of annual and winter NAO reconstructions show a diminished value and variance during the time period before 1650s. Thus, to avoid high uncertainty and potential inconsistency inside the reconstruction, we only use the later section of the winter NAO index, during 1659-2000, in the following multidecadal data comparison and correlation calculation.

Comparison of *G. bulloides* abundance and winter NAO reconstruction time series also indicates they have significant correlation at multidecadal timescales, with slight shift (Figs. 4-20, 4-21). We can see that the two time series in Fig. 4-20 (bottom) also display a same-sign relationship. By comparing Fig. 4-20 (bottom) with Fig. 4-17 (bottom), relationship between *G. bulloides* abundance and these two NAO reconstructions is found to be highly consistent with each other during their overlapped period, 1830-1950.

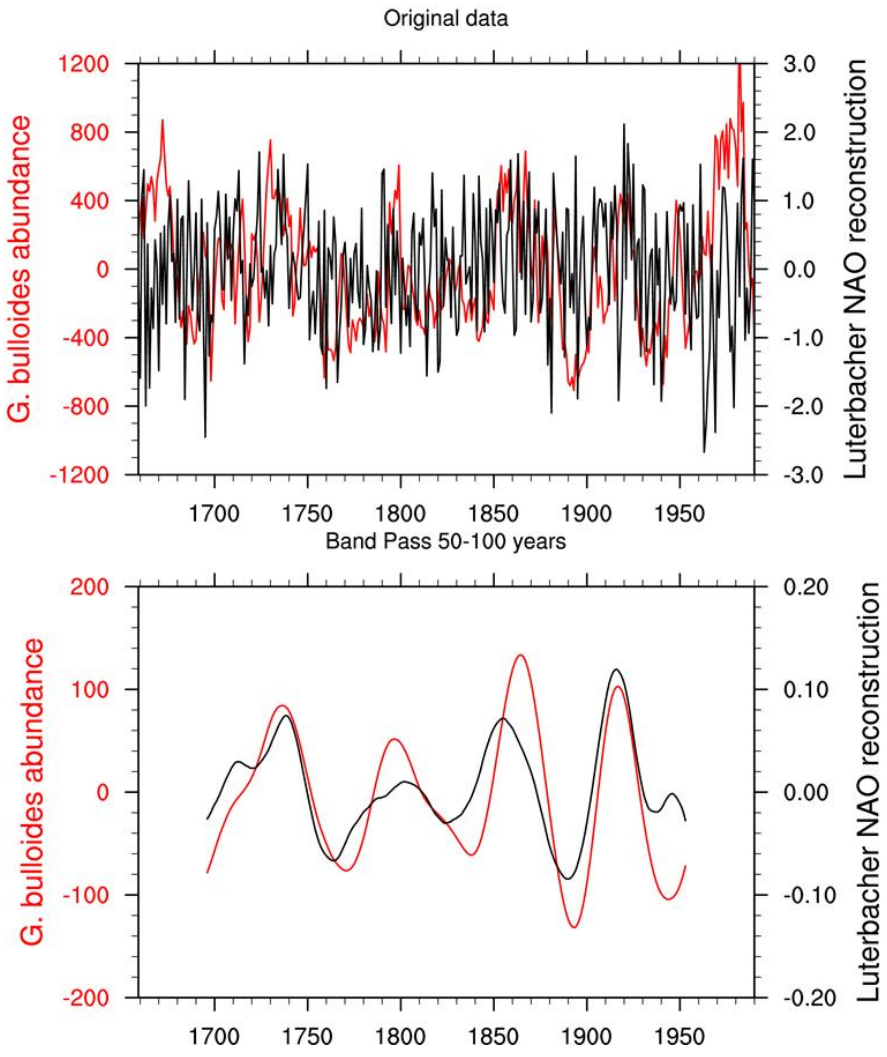

Figure 4-20. Comparison of G. bulloides abundance (red) and winter NAO reconstruction (black) with (upper) original time series, (lower) time series filtered by 50-100 years band pass filter.

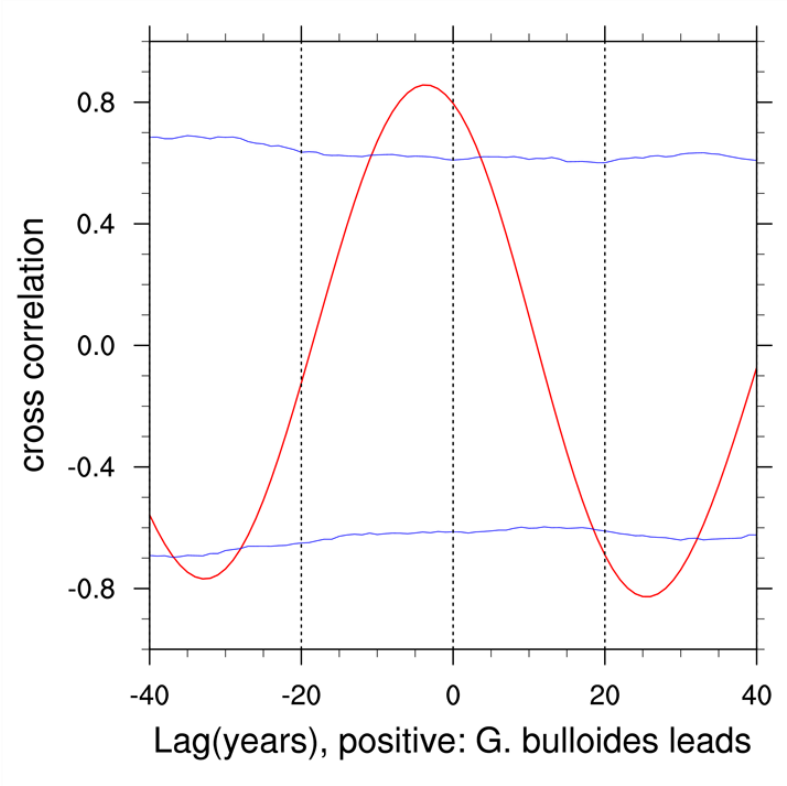

Figure 4-21. Same as Figure 4-7, except between 60-80 year band pass filtered G. bulloides abundance and Luterbacher winter NAO reconstruction.

Their lag-lead relationship of *G. bulloides* abundance and Luterbacher's winter NAO reconstruction is shown in Fig. 4-21. In this figure, we can see that when the low-frequency time series of NAO reconstruction leads for 4 years, their correlation is the largest and significant (r = 0.86). Peaks of NAO are considered coincide with the peaks of *G. bulloides* abundance, indicating an opposite-sign relationship between the multidecadal NAO and AMO during this period of time. These comparison results based on two different NAO reconstructions further confirms that the multidecadal variation signal contained in *G. bulloides* data is related to large circulation at Atlantic basin and Atlantic climate has multidecadal variability before industrialization.

4.4. Discussion of Cariaco Basin *Globigerina bulloides* abundance variation mechanism at longer timescales

In the comparison of the original unsmoothed, non-detrended *G. bulloides* abundance data and other paleoclimate data, we found that the opposite-sign relationship between multidecadal variabilities of *G. bulloides* and AMO may not be able to explain *G. bulloides* data at longer timescales. To discuss its longer term variations, we compared it with three other Cariaco Basin paleoclimate data that display significant lower frequent variabilities.

In Fig. 4-22, we show the original and 10-year-running-mean time series of *G. bulloides* abundance (Fig. 4-22 upper), winter/spring SST reconstruction based on *G. bulloides* Mg/Ca ratio and summer/fall SST based on *G. ruber* (pink) Mg/Ca ratio (Fig. 4-22 middle), and Ti concentration (%) data that indicates local watershed rainfall variations and ITCZ south-north shift [*Haug et al.*, 2001; *Kennett et al.*, 2012] (Fig. 4-22 lower).

The spectral analysis and wavelet analysis indicate that these Cariaco Basin SSTs do not have significant multidecadal variabilities. They do not bear similarities with AMO index during the instrumental period either (not shown). Also, multidecadal *G. bulloides* data does not have significant correlation with these SST reconstructions, filtered by 50-100 year band pass filter.

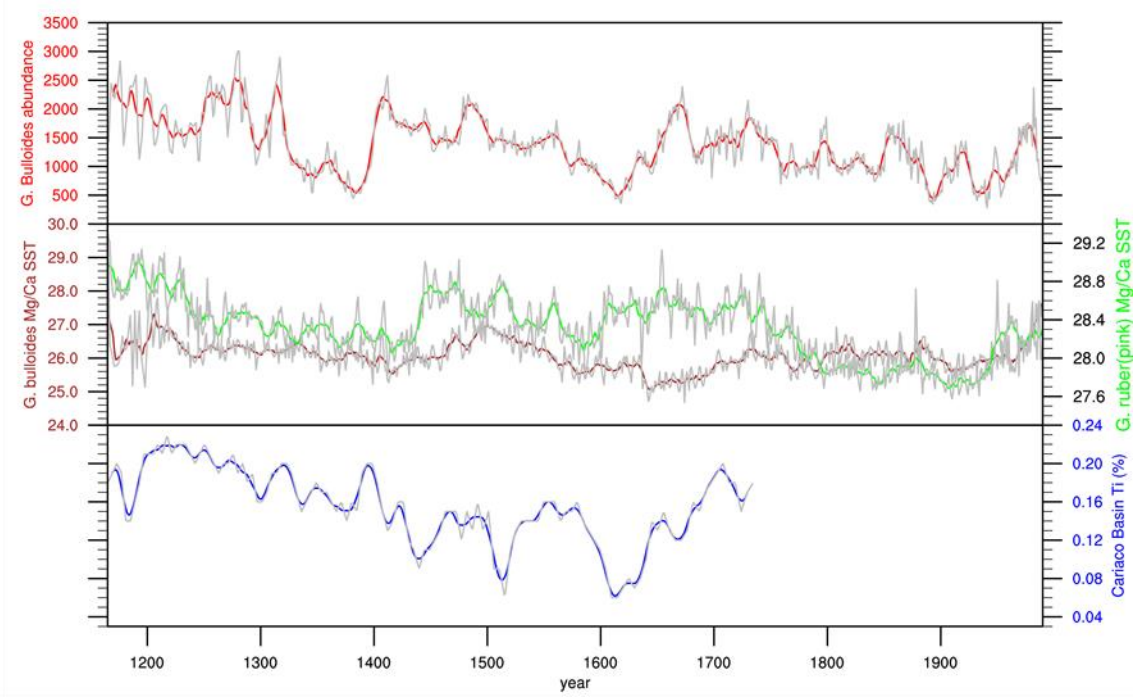

Figure 4-22. Original data (gray) and 10 year running averages (other colors) of 1165-1990 G. bulloides abundance (red), G. bulloides Mg/Ca SST (brown), G. ruber (p) Mg/Ca SST (green), and Cariaco Basin Ti% (blue).

On the other hand, these two SST reconstructions have peak variances at periodicities longer than 150 year. Not as for the multidecadal variabilities, the SSTs' variations at these timescales show in-phase relationship with *G. bulloides* abundance. It means that the larger *G. bulloides* abundance corresponds to higher local SST. The comparison of the two time series in Fig. 4-23 can illustrate this relationship. However, the correlation between this summer/fall SST reconstruction and *G. bulloides* abundance is not significant.

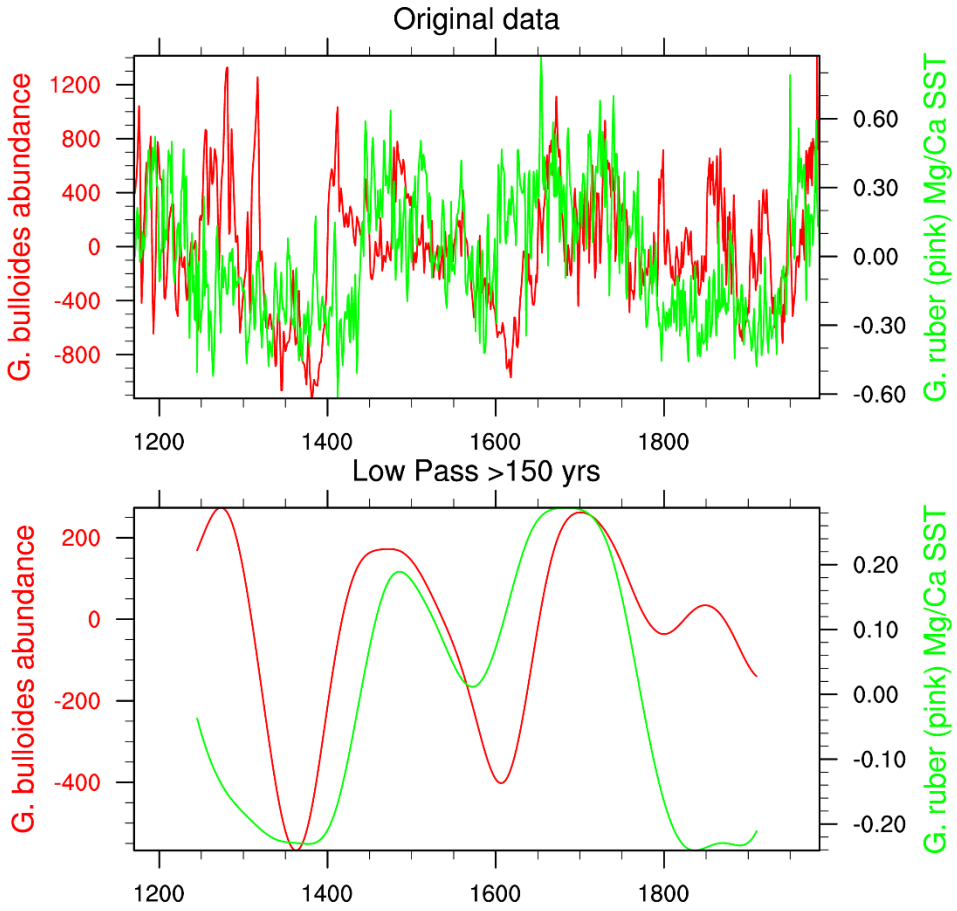

Figure 4-23. Comparison of G. bulloides abundance (red) and G. ruber(p) SST index (green) with (upper) original time series, (lower) time series filtered by 150 year low pass filter.

Correlation values of *G. bulloides* abundance data and the Ti% data are not significant at multidecadal or centennial timescales. Considering the large error of the age model of Ti% data, it is also not suitable to be used in analyses at these timescales. Nevertheless, in Fig. 4-22, we can see both of *G. bulloides* abundance data and the Ti% time series have a decreasing trend before about early 17th century and an increasing trend from the early 17th century to the middle 18th century.

As mentioned previously, nutrients from trade wind driven upwelling, Cariaco Basin watershed rainfall driven riverine inputs, and easterly wind transported African dust can influence Cariaco Basin *G. bulloides* abundance variation. It is possible that the local rainfall effect may dominate the mechanism of the *G. bulloides* production variation at millennial timescales and/or above. When annual mean ITCZ position shift to north, Cariaco Basin and Sahel rainfall increases while local coastal zonal wind decreases, suppressing both of the upwelling and dust source of nutrients. However, these time series are too short to see such a long term variability.

Previous studies on the relationship between cross-equatorial SST gradient and ITCZ mean position shifting suggests that when the tropical North Atlantic SST increases, North-to-South SST gradient decreases and ITCZ moves to the north. Thus, we suspected that the concurrence of high Cariaco Basin SST and *G. bulloides* abundance at centennial timescales shown in Fig. 4-23 (bottom) can also be explained by the rainfall domination effect. However, by comparing the SST reconstructions to the Ti% data, we cannot find association between high Cariaco Basin SST with large local precipitation or with northward movement of ITCZ mean position at this timescale. More studies are needed to explain the mechanism of *G. bulloides* abundance variation at this timescale. In the future studies, the relationship between Cariaco Basin local SST with local precipitation, tropical North Atlantic SST and ITCZ movement will also be examined.

4.5. Summary

Multidecadal variation of *G. bulloides* abundance in the last 800 years is shown to be consistent with the SST variability at Eastern Tropical Atlantic [*Kuhnert and Mulitza*, 2011] and Puerto Rico [*Kilbourne et al.*, 2008], at the same timescales as what was found in Chapter 3 based on reanalysis data in the last century. This result suggests the natural variability of AMO and its spatial pattern, at least at low latitudes, exist before the instrumental period. It also indicates that multidecadal *G. bulloides* abundance can reflect the AMO during its whole time span.

Globigerina bulloides abundance at this timescale also displays a same-sign relationship with multidecadal variabilities of the NAO reconstructions that are based on Bermuda [*Goodkin et al.*, 2008a] and based on northeastern North Atlantic to Europe [*Luterbacher*, 2002]. This result is consistent with the out-of-phase relationship between multidecadal NAO and AMO, shown in previous studies. The results derived from both of the two NAO reconstructions shows consistency during their overlapping periods.

Chapter 5. Evaluation of Atlantic Multidecadal Variability in CMIP5 models

After the relationship is established between *G. bulloides* data and North Atlantic SST variability during the past century based on observation and reanalysis data, and during the past millennium based on paleoclimate data, we would like to evaluate if the models can capture the observed SST variability in the historical and last millennium simulations.

Previously, several studies have already assessed the performance of CMIP5 models on simulating Atlantic Multidecadal Variability in historical simulations [*Zhang and Wang*, 2013; *Martin et al.*, 2014] and in last millennium runs [*Landrum et al.*, 2013; *Zanchettin et al.*, 2013]. The assessment works are done in many aspects, including the variability and magnitude of the AMV, relationship between AMO and AMOC, AMV's sensitivity to external forcing, teleconnection between AMV and Sahel rainfall, etc.

Although we have not done analyses on the relationship between AMO and AMOC, the five models we will compare in this study fall into all of the four categories based on AMOC-AMO relationship [*Zhang and Wang*, 2013]. All the five models can generally capture the AMOC structure in their comparison work, but show large differences in simulating AMO amplitudes and phases.

The MPI-ESM-P belongs to Category I, which simulates a positive correlation between AMOC and AMO when the AMOC leads the AMO and a negative correlation when the AMO

leads the AMOC. It means that when the AMOC leads the AMO, enhanced AMOC increases heat transport convergence in the North Atlantic, which induces AMO warm phase. And after a while, the AMO warm phase warms the mid- and high-latitudes, reduces the North Atlantic meridional density gradient, and thus leads to a weakening of the AMOC. This relationship is consistent with the AMOC mechanism proposed by *Lee and Wang*, 2010, the delayed advective oscillation mechanism.

CCSM4 and FGOALS models are in Category II, which simulate negative correlation between AMOC and AMO, no matter when the AMOC leads or lags the AMO. Similarly, MRI-CGCM3 is in Category III, simulating uniformly positive correlations. This indicates that there is positive feedback between AMOC and AMO, and they will not oscillate unless other feedbacks, such as external forcing, are involved.

And the fourth category includes BCC-CSM 1-1. Models in this category show a complicated correlation between the AMO and AMOC.

The evaluation work we do here is to compare historical and last millennium AMV simulations in these five models based on the analyses in Chapter 3 and Chapter 4, as well as in the context of previous works.

5.1. Evaluation using the 20th century reanalysis data

The aim of this section is to compare the performance between the models during the instrumental period, which we have the observation and reanalysis data as reference. Providing the observation reference, the three leading significant components of the EOF (Empirical Orthogonal Function) analysis of ERA-20C reanalysis North Atlantic SST variability are shown in Fig. 5-1, which together explain 56.6% of the variability.

The EOF 1 shows a same-sign spatial pattern for the entire North Atlantic, and the first principal component (PC 1) indicates an evident multidecadal variability. This spatial-temporal feature of SST is AMV-like. Similar to the method in *Martin et al.*, 2014, we will use the North Atlantic SST PC1 time series to represent an AMV index, which is almost identical to the AMO index we used in the Chapter 3 [*Enfield et al.*, 2001]. Using this AMV index, we will be able to compare structures of and responses to the AMV in models to observations and reanalysis. EOF 1 explains 34.3% of the North Atlantic SST variance.

The EOF 2 presents a familiar tripole pattern of SST, with the SST anomaly along latitudes of Gulf Stream being opposite-sign to the other regions in North Atlantic. It explains 13.7% of the SST variance. The EOF 3 pattern looks like EOF 2 with a latitudinal shift. Both of PC 2 and PC 3 have shown multidecadal temporal variability, as well as variations at higher frequencies. These patterns will be compared by the same analyses of the SST field from historical simulation of the five CMIP5 models described in Table 2-1.

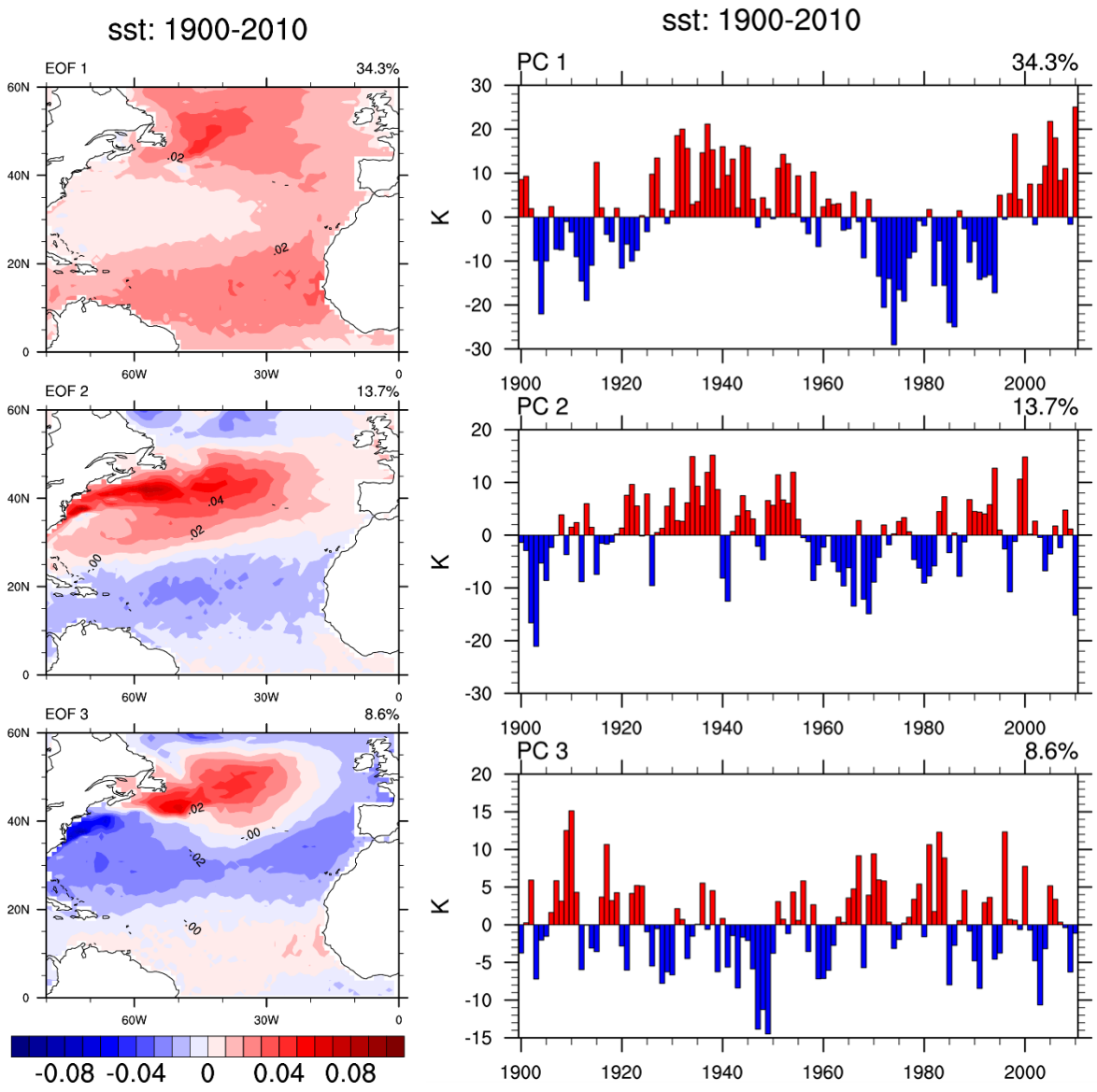

Figure 5-1. (Left) Spatial pattern and (Right) Principal components (PC) time series of the three leading EOFs of North Atlantic SST in the region of (0°-60°N, 0°-80°W), derived from 1900-2010 ERA-20C reanalysis data.

Compared to the reanalysis in Fig. 5-1, the EOF analysis of BCC-CSM 1.1 SSTs (Fig. 5-2) indicates that the model cannot capture the three leading modes of the SST variability in North Atlantic. Both of the spatial pattern and temporal variation of the first mode do not reflect the observed phenomenon. The EOF 2 is similar to EOF 1 of ERA-20C reanalysis SST, but it only explains 14.4% of the variability. There is resemblance between the spatial pattern of EOF 3 of the simulated SST and EOF 2 of the reanalysis data, but the temporal variation of EOF 3 is with much higher frequencies.

The FGOALS-s2 (Fig. 5-3) does a better job in the first mode, as it captures the same-sign spatial pattern and multidecadal variability of PC 1 during most of the period. However, its EOF 1 shows a clear center at mid-latitude, rather than the horseshoe pattern in reanalysis data. The low-latitude arm of the AMO pattern is missing. The EOF 2 is not similar to the observed leading modes. As for its third mode, a tripole mode similar to the one with reanalysis data is captured, with similar multidecadal variability in the corresponding PC. However, due to the performance of the first two modes, it is not considered very effective.

Same analysis of CCSM4 simulation (Fig. 5-4) finds more consistent patterns with the reanalysis. The first mode bears much resemblance with the EOF 1 in Fig. 5-1, with relative lower similarity over higher latitudes. PC 1 shows multidecadal variations, but also higher frequency variabilities. The EOF 2 also captures the tripole pattern, with a larger center over the latitudes of Gulf Stream. The third mode is also like shifting the second mode north. PC 2 and PC 3 contain multidecadal variabilities as observed.

The analysis of MPI-ESM-P outputs (Fig. 5-5) gives a horseshoe spatial pattern for EOF 1, which is similar to the reanalysis pattern, including in the higher latitudes. PC 1 shows multidecadal and lower-frequency variations. The EOF 2 pattern has a concentrated center over the latitudes of Gulf Stream. And third mode shows a dipole between low and high latitude.

MRI-CGCM3's EOF 1 pattern (Fig. 5-6) is similar to MPI-ESM-P, but with a rather intense center to a more eastern position at high latitude. This pattern is not considered quite consistent with the reanalysis results, as it shows a too large zonal SST gradient in the higher latitude. Its second and third modes of EOF analysis do not capture the reanalysis patterns. All of the three PCs have relatively higher frequency variations too.

From the EOF analysis, we can see that only CCSM4 and MPI-ESM-P model captured the similar patterns of the first mode of North Atlantic SST as in the reanalysis data. Also, these two models captured the tripole SST mode in the second EOF. However, they also have discrepancies compared to the reanalysis pattern, and their EOF 1 explain less variance of North Atlantic SST. To further investigate the performance of these models in capturing the relationship between the North Atlantic SST and other variables shown in Chapter 3, we compare the same regression maps using reanalysis data (Fig. 5-7) to the ones using model simulations (Fig. 5-8, 5-9).

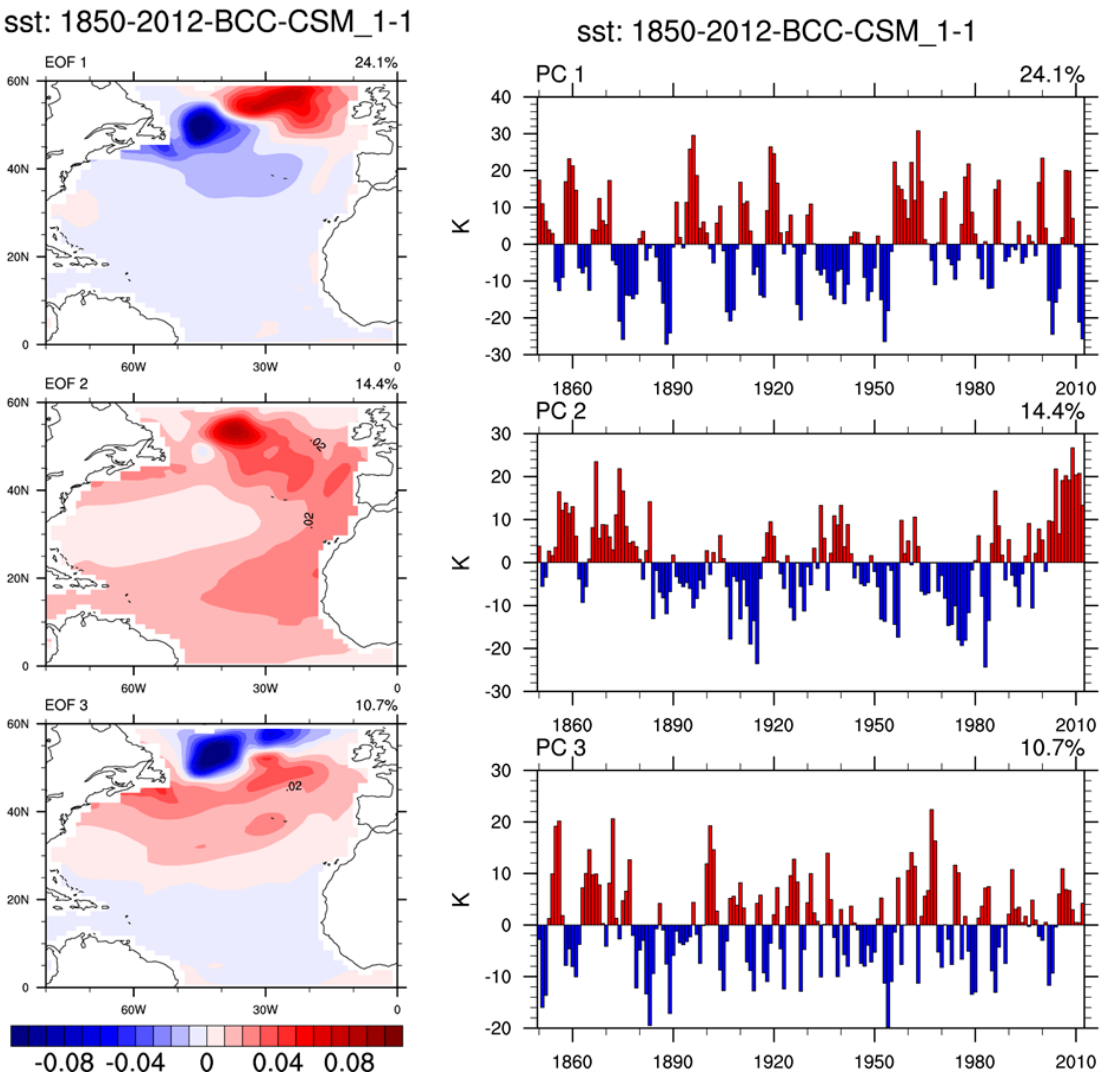

Figure 5-2. (Left) Spatial pattern and (Right) PC time series of the three leading EOFs of North Atlantic SST in the region of (0°-60°N, 0°-80°W), derived from the historical simulation outputs (1850-2005) of model BCC-CSM 1.1.

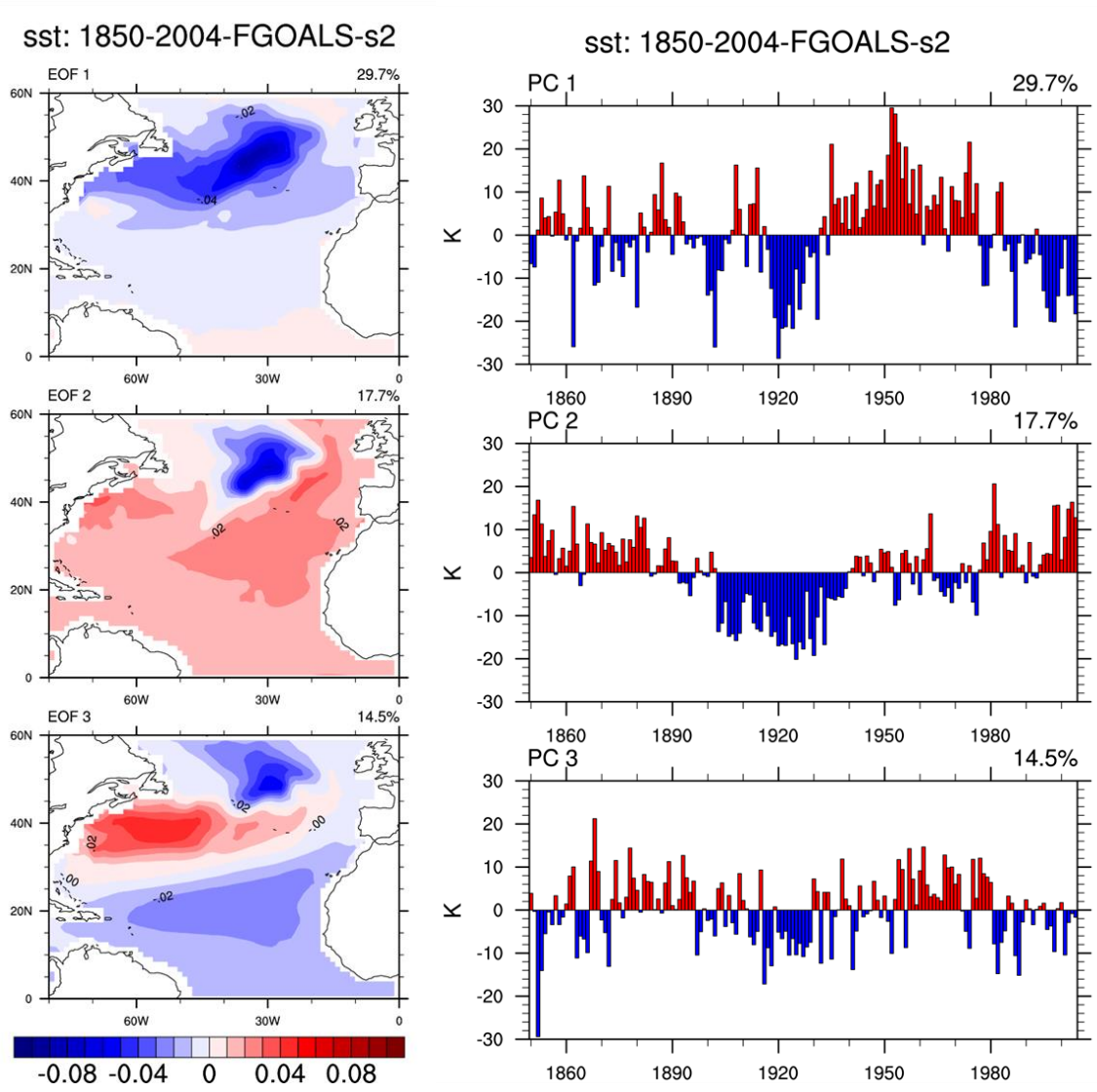

Figure 5-3. (Left) Spatial pattern and (Right) PC time series of the three leading EOFs of North Atlantic SST in the region of (0°-60°N, 0°-80°W), derived from the historical simulation outputs (1850-2005) of model FGOALS-s2.

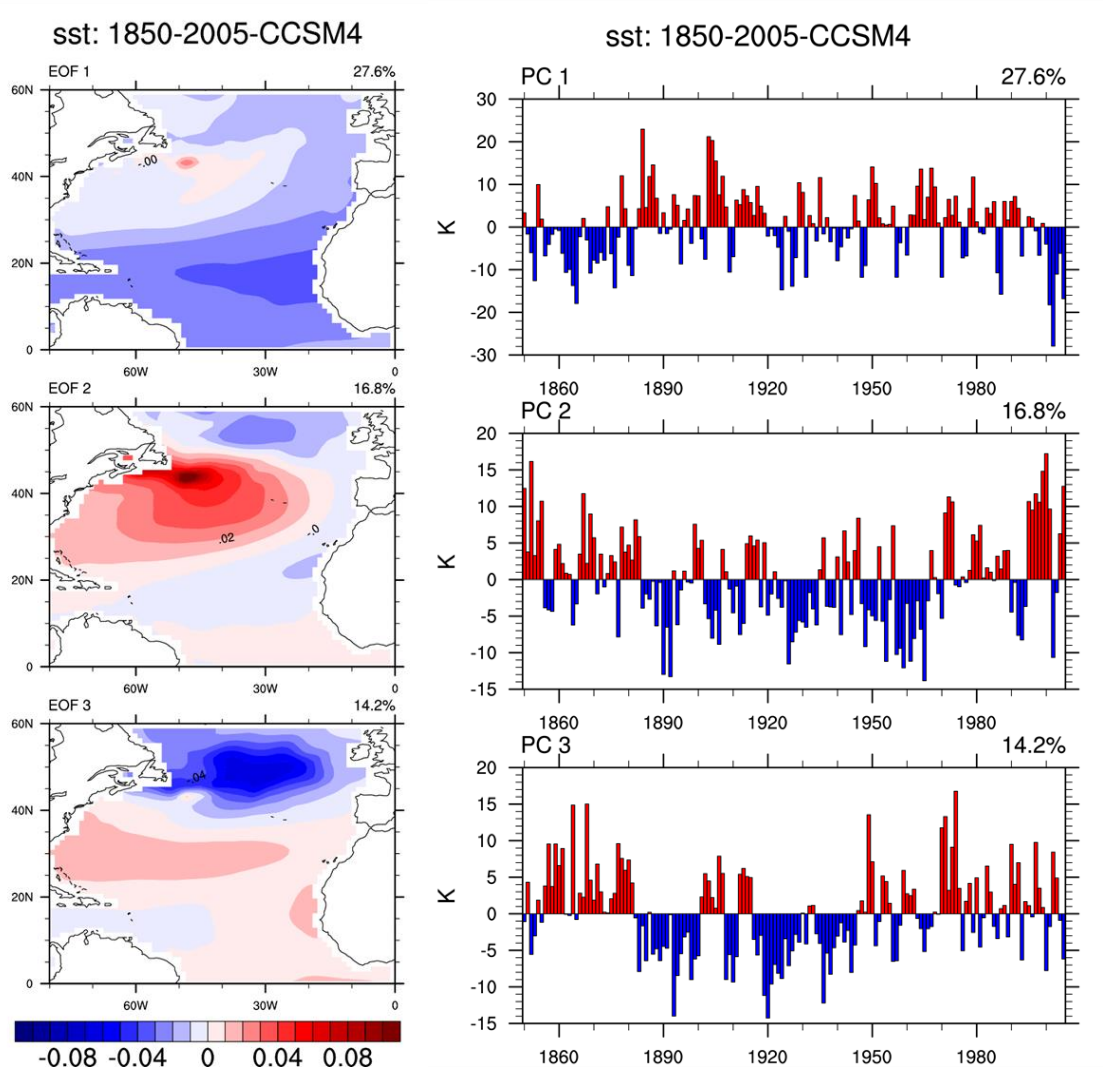

Figure 5-4. (Left) Spatial pattern and (Right) PC time series of the three leading EOFs of North Atlantic SST in the region of (0°-60°N, 0°-80°W), derived from the historical simulation outputs (1850-2005) of model CCSM4.

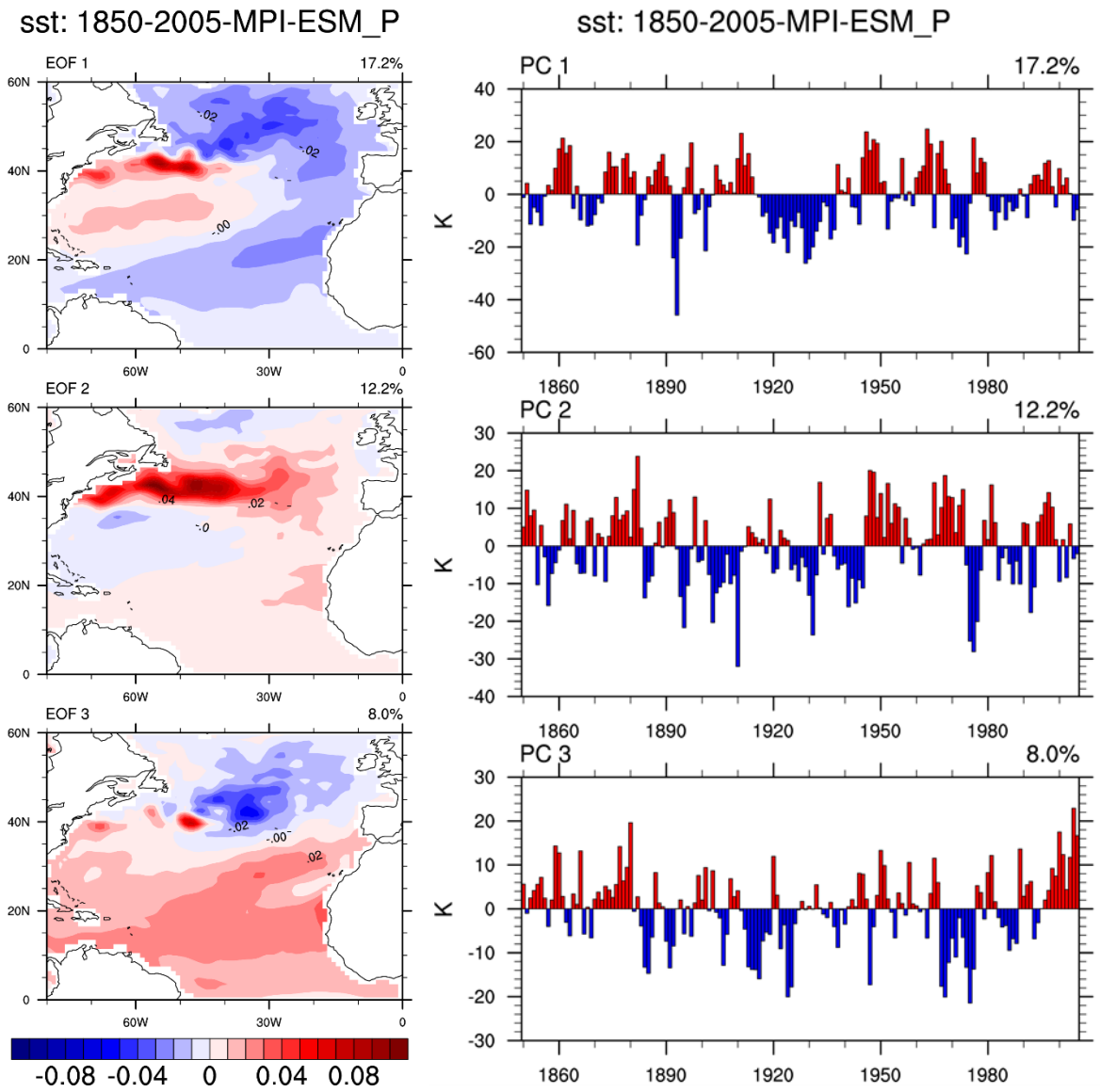

Figure 5-5. (Left) Spatial pattern and (Right) PC time series of the three leading EOFs of North Atlantic SST in the region of (0°-60°N, 0°-80°W), derived from the historical simulation outputs (1850-2005) of model MPI-ESM-P.

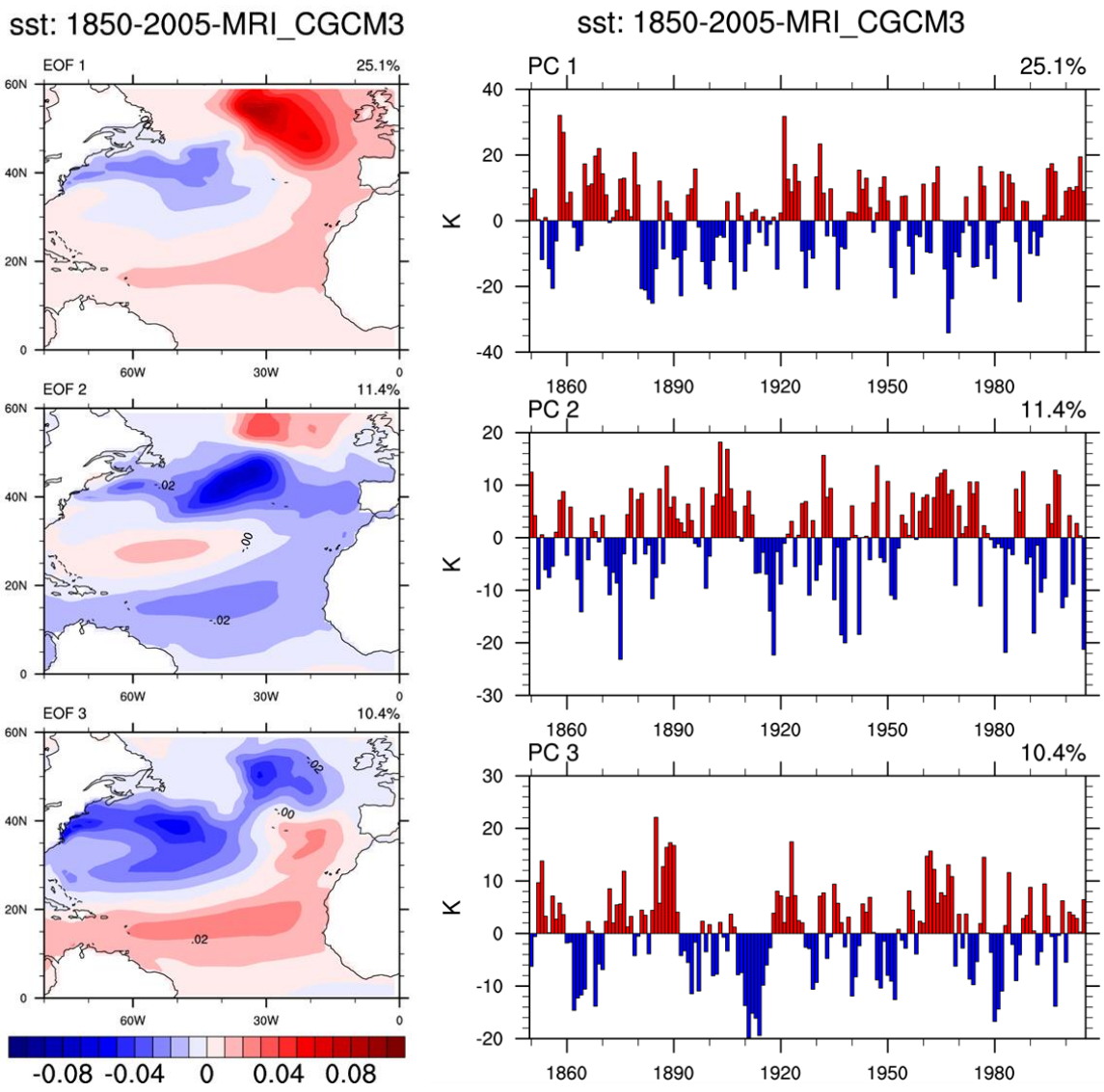

Figure 5-6. (Left) Spatial pattern and (Right) PC time series of the three leading EOFs of North Atlantic SST in the region of (0°-60°N, 0°-80°W), derived from the historical simulation outputs (1850-2005) of model MRI-CGCM3.

To complement the regression analysis in Chapter 3 using indices, the regression coefficient patterns of SST, SLP, surface wind, and precipitation against North Atlantic SST PC1 (the AMO index) using annual time series (Fig. 5-7a) and filtered time series (Fig. 5-7b) are presented for the ERA-20C reanalysis. Comparison of Fig. 5-7a and Fig. 3-2b indicates that the

annual reanalysis SST PC1 well-captured the AMO variability in the observation during the past century and the relationship between the other fields with AMO. And the plot with low-frequent time series (Fig. 5-7b) is also showing similar patterns as in Fig. 3-3b. From these figures, we can see the consistent relationship between colder North Atlantic SST, higher Azores High pressure, and more intense easterly trade wind.

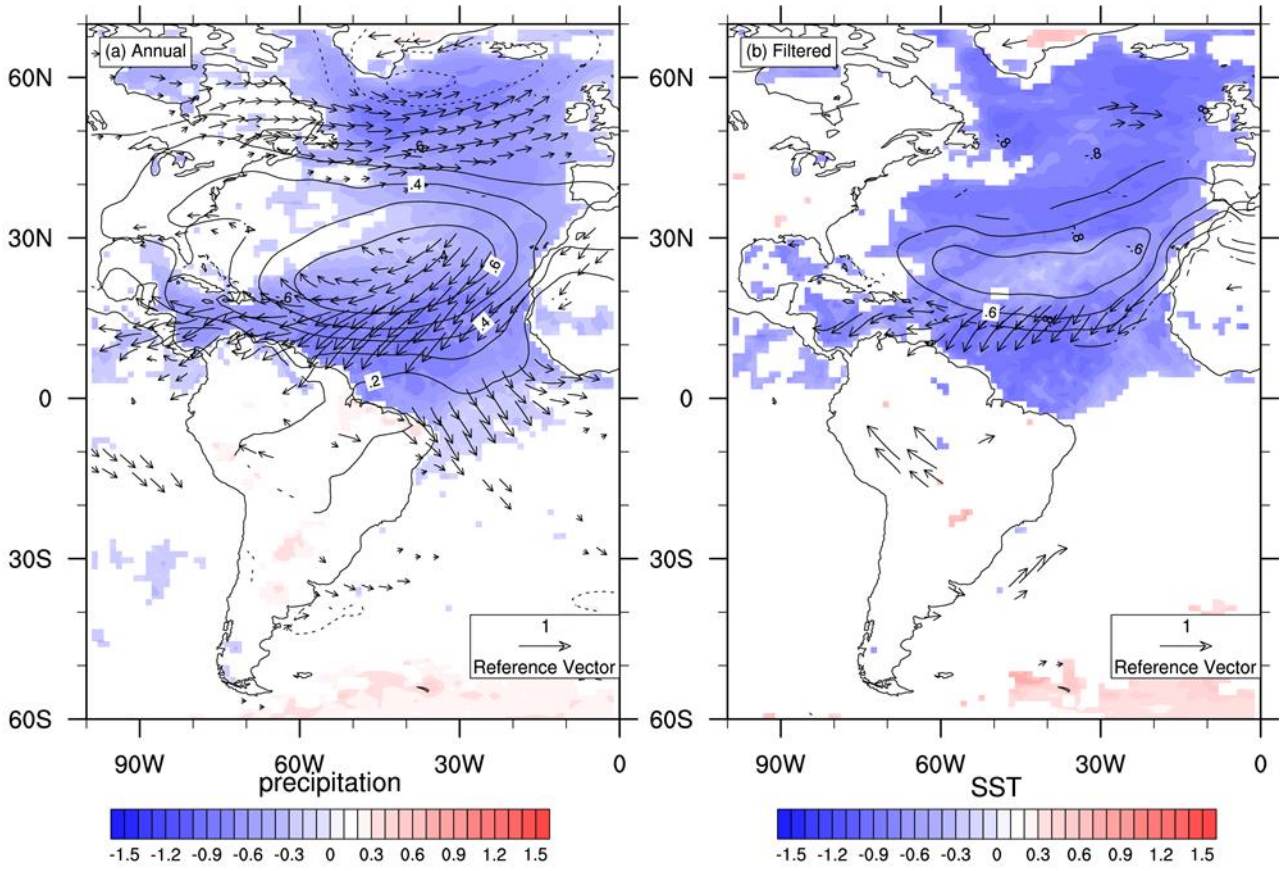

Figure 5-7. 1901-2010 de-trended standardized (a) annual mean precipitation (color shades over land), SST (color shades over ocean), Sea level pressure (contours over ocean), and Surface wind (vectors) regression coefficients against de-trended standardized PC1 of North Atlantic SST from ERA-20C reanalysis; (b) the same as (a) except using filtered data.

Similar regression maps based on CCSM4 historical simulation data are shown in Fig. 5-8. The spatial distribution of coefficients for SST shows similar pattern as in Fig. 5-7a in the

North Atlantic, while the corresponding part for SLP shows a center shifting much too west in Fig. 5-8a. The patterns for wind display a similar shift, but mostly captured the observed relationship between 10°-20°N. However, the significant correlation between the AMO and Sahel rainfall is not shown in this map, probably due to the western shift of subtropical High center. Besides, the plot with filtered data (Fig. 5-8b) is quite different from Fig. 5-7b. The relationship between the SST and other variables are generally disappears, which imply that the relationship between the low-frequency variables are not well simulated.

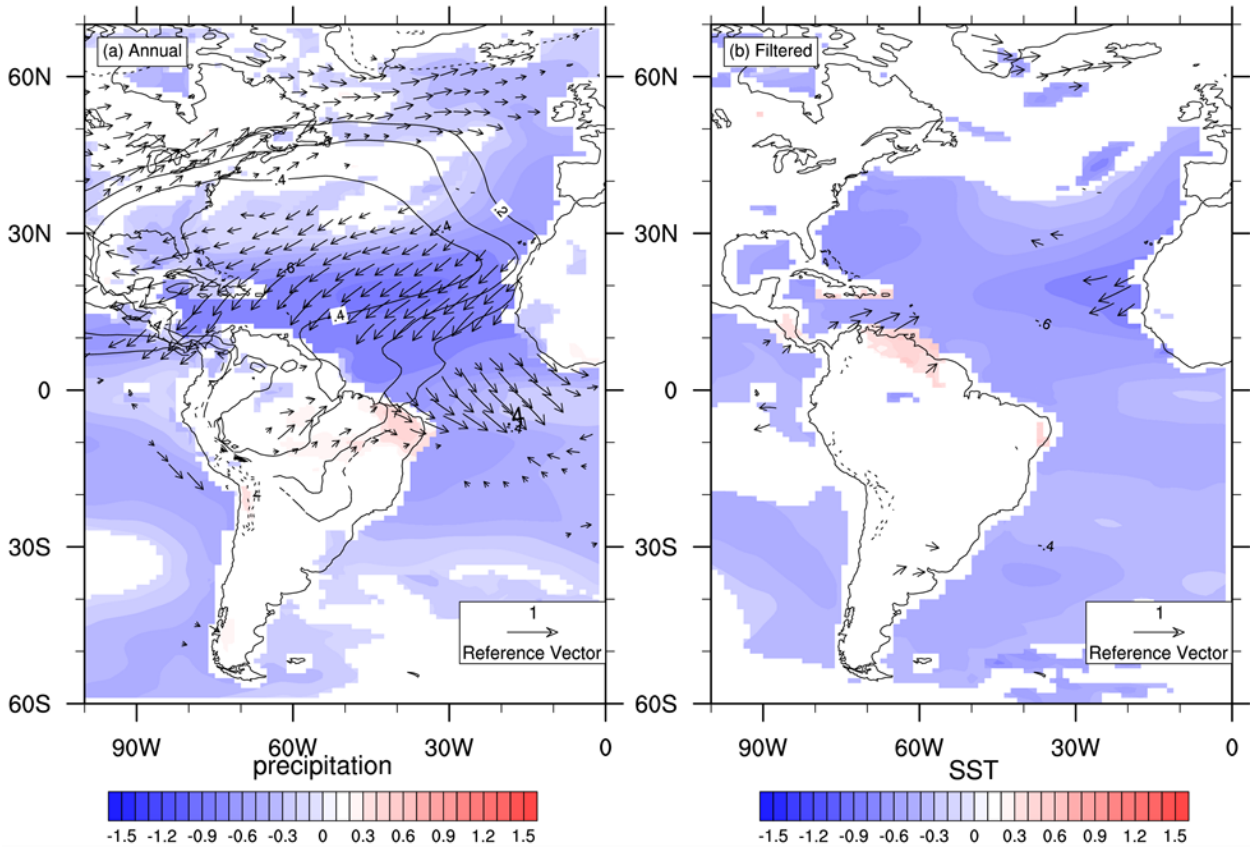

Figure 5-8. Same as Figure 5-10, except for using CCSM4 historical simulation outputs, 1850-2005.

The same analysis based on MPI-ESM-P historical simulation are shown in Fig. 5-9. The regression coefficients for SLP and surface winds in Fig. 5-9a display similar patterns in the North Atlantic as in Fig. 5-7a. Nonetheless, the regression maps with filtered data (Fig. 5-12b) also shows large discrepancy from Fig. 5-7b, displaying almost no significant relationship between the AMO and other variables.

However, there is a discrepancy between the CCSM4 and MPI-ESM-P simulations lies in these regression patterns. The regression maps of CCSM4 (Fig. 5-8a and 5-8b) show similar, same sign, regression coefficients of SST for the whole Atlantic Basin and (tropical) eastern Pacific. This is not shown in the same maps based on reanalysis data (Fig. 5-7a and 5-7b) or MPI-ESM-P simulations (Figs 5-9a and 5-9b). The interhemispheric contrast of SST is a fingerprint of the AMOC activity [*Zhang*, 2008]. Previous studies showed that both of the CCSM4 and MPI-ESM-P can generally capture the AMOC structure correctly, but the representation of AMOC-AMO relationship in these two models are different [*Zhang and Wang*, 2013]. This discrepancy may come from this difference. As mentioned earlier this Chapter, The AMOC-AMO relationship in MPI-ESM-P is consistent with the delayed advective oscillation mechanism [*Lee and Wang*, 2010], while CCSM4 AMO oscillation suggests no internal oscillation mechanism. Thus, the CCSM4's whole basin same sign AMO patterns may reflect the global SST variation signal which may be induced by some external forcing, while the MPI-ESM-P can display some effect of the internal AMO variability.

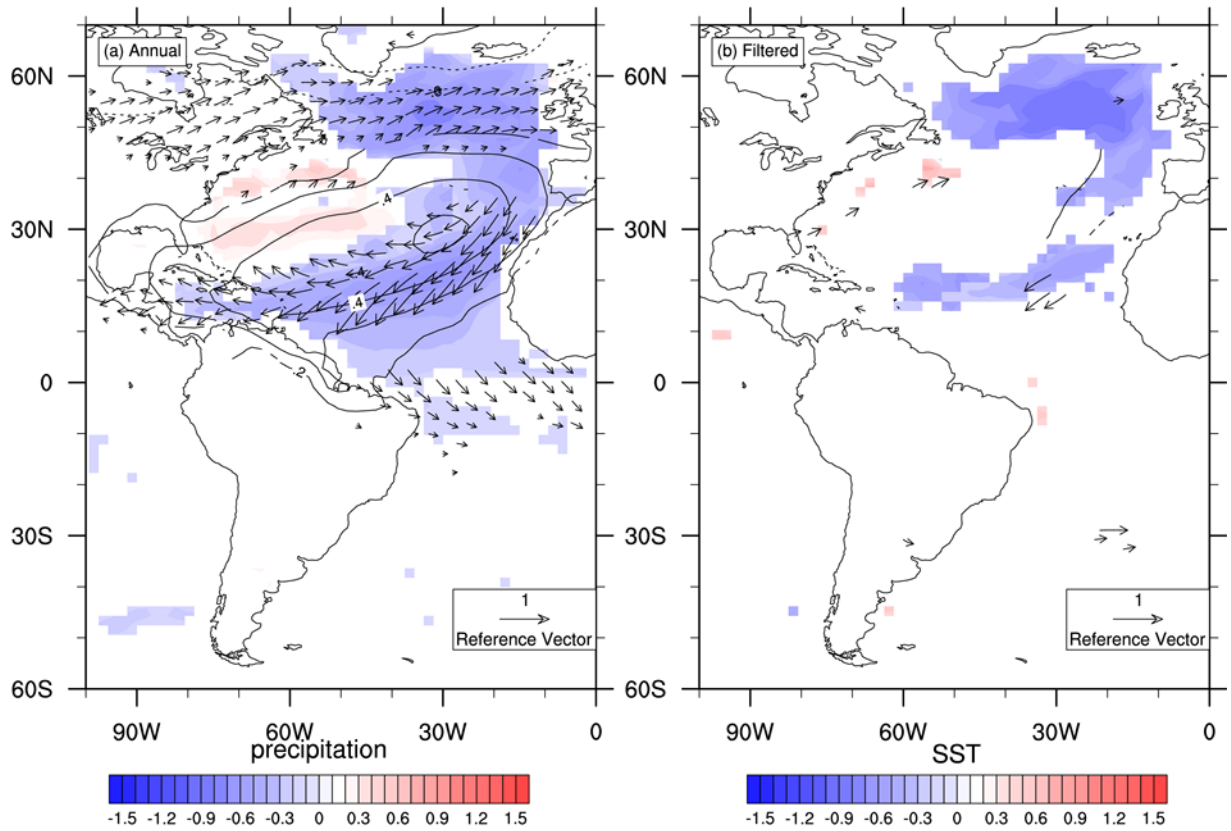

Figure 5-9. The same as Fig. 5-10, except for based on MPI-ESM-P historical simulation, 1850-2005.

5.2. Evaluation based on proxy data comparison

The results in Chapter 4 imply that the Atlantic multidecadal variability exists before instrumental period. Based on this finding, we compare the CMIP5 modeling of the North Atlantic SST pattern again, using the last millennium simulations (850-1850) in this section. The results of the EOF analyses of North Atlantic SSTs from this long term simulations of the five models are displayed in Figs. 5-10 to 5-14.

The EOFs of the modeled North Atlantic SST from last millennium simulations of the five models show similar spatial patterns as their counterparts using historical runs (Figs. 5-2 to 5-6). The EOF 1 of CCSM4 (Fig. 5-12) and of MPI-ESM-P SSTs (Fig. 5-13) have same sign over the North Atlantic basin, and are most similar to the EOF 1 of reanalysis SST in Fig. 5-1.

To investigate the stationarity of this spatial pattern, we obtained 20 random samples of consecutive 91-year North Atlantic SST field from the 1000 year simulation of each model, by applying a 91-year moving-blocks bootstrap sampling method. By comparing the EOF 1 of the 20 samples from each model, we found that the MPI-ESM-P gives AMO-like patterns in most of its samples, while CCSM4 shows less stationarity. For CCSM4, the EOF 1 spatial pattern demonstrates an alternation between its EOF 1 and EOF 2 patterns of the historical run (as in Fig. 5-4), during the 1000 year period.

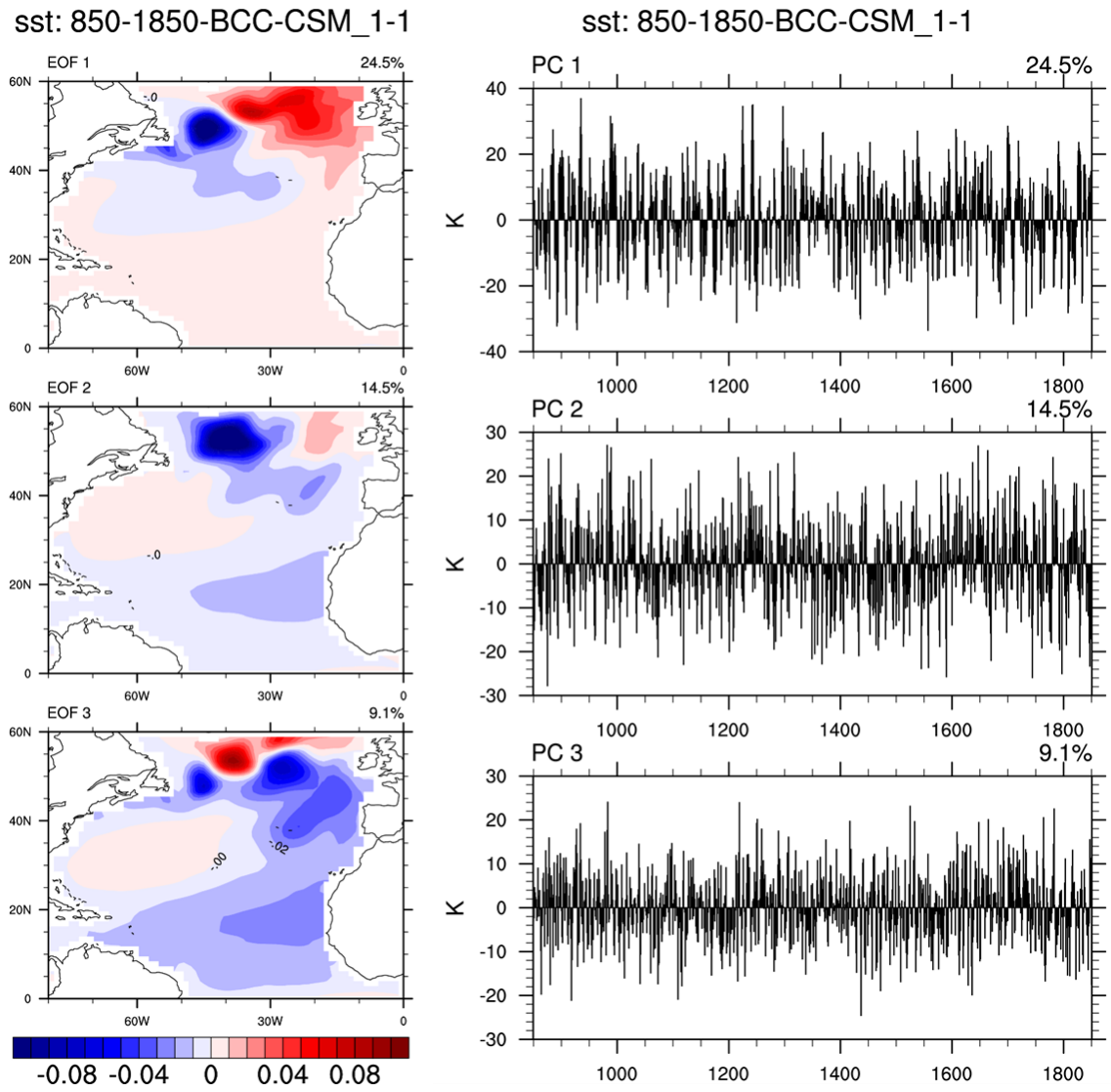

Figure 5-10. (Left) Spatial pattern and (Right) PC time series of the three leading EOFs of North Atlantic SST in the region of (0°-60°N, 0°-80°W), derived from the past millennium simulation outputs (850-1850) of model BCC-CSM 1.1.

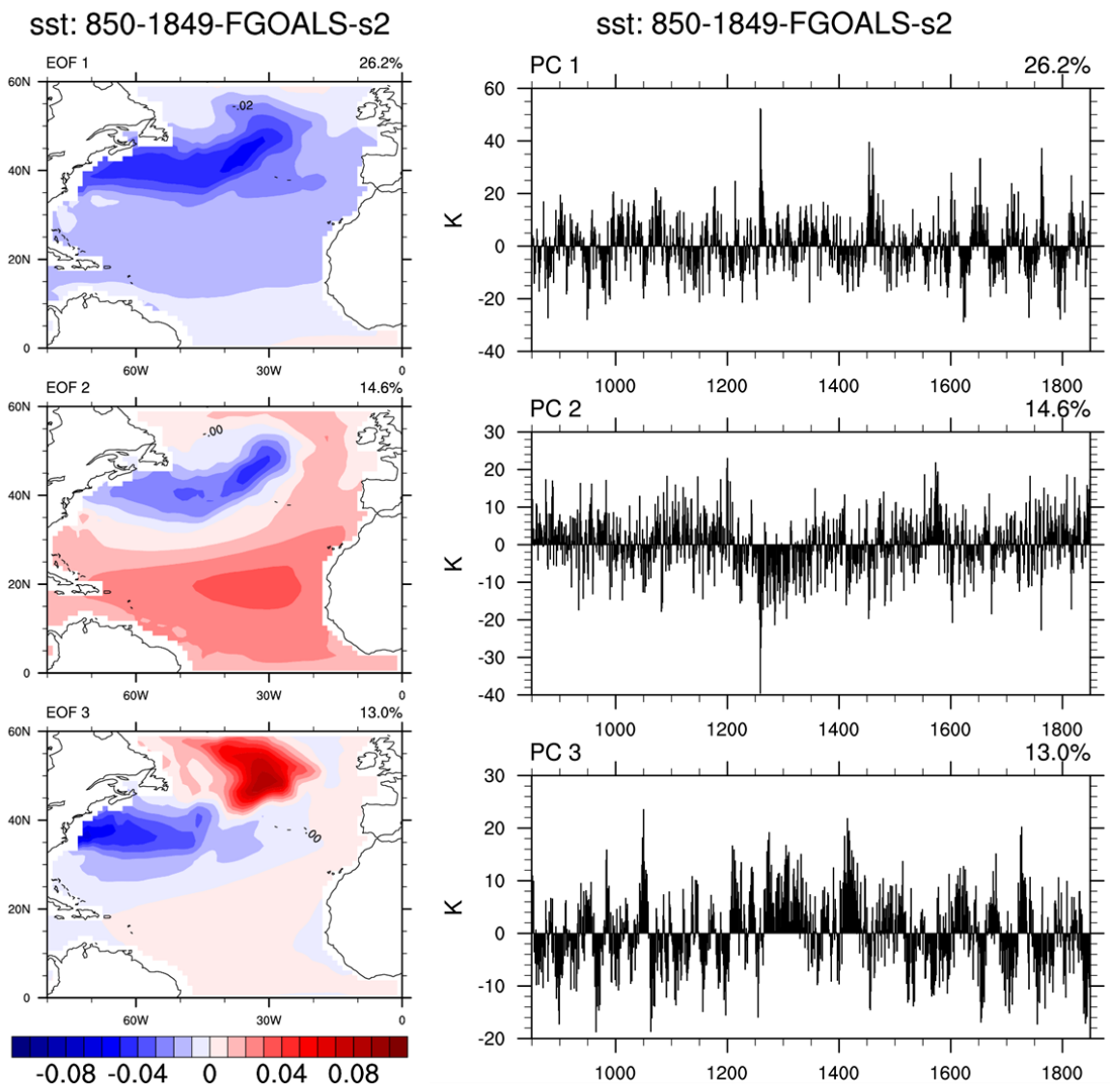

Figure 5-11. (Left) Spatial pattern and (Right) PC time series of the three leading EOFs of North Atlantic SST in the region of (0°-60°N, 0°-80°W), derived from the past millennium simulation outputs (850-1849) of model FGOALS-s2.

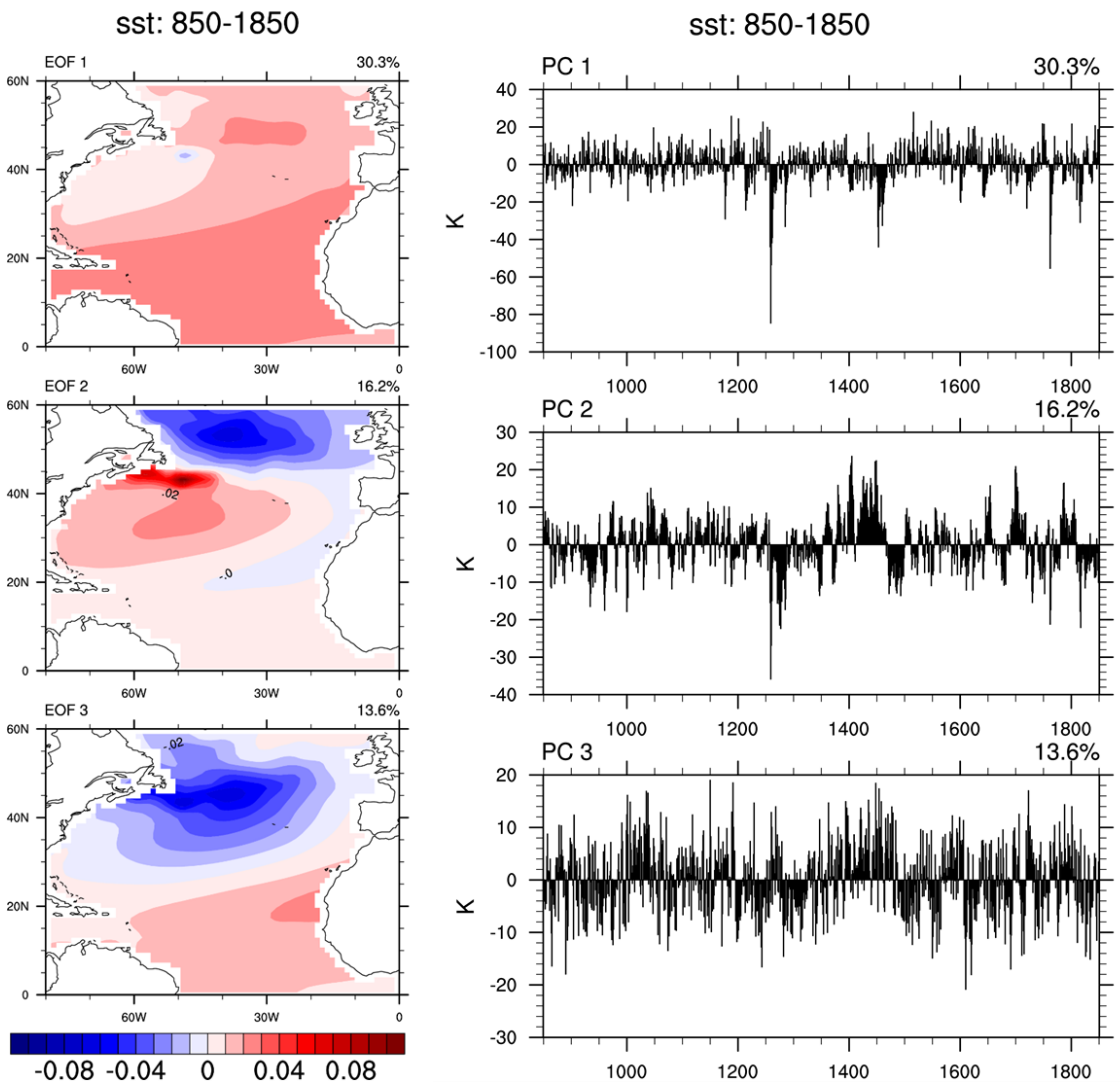

Figure 5-12. (Left) Spatial pattern and (Right) PC time series of the three leading EOFs of North Atlantic SST in the region of (0°-60°N, 0°-80°W), derived from the past millennium simulation outputs (850-1850) of model CCSM4

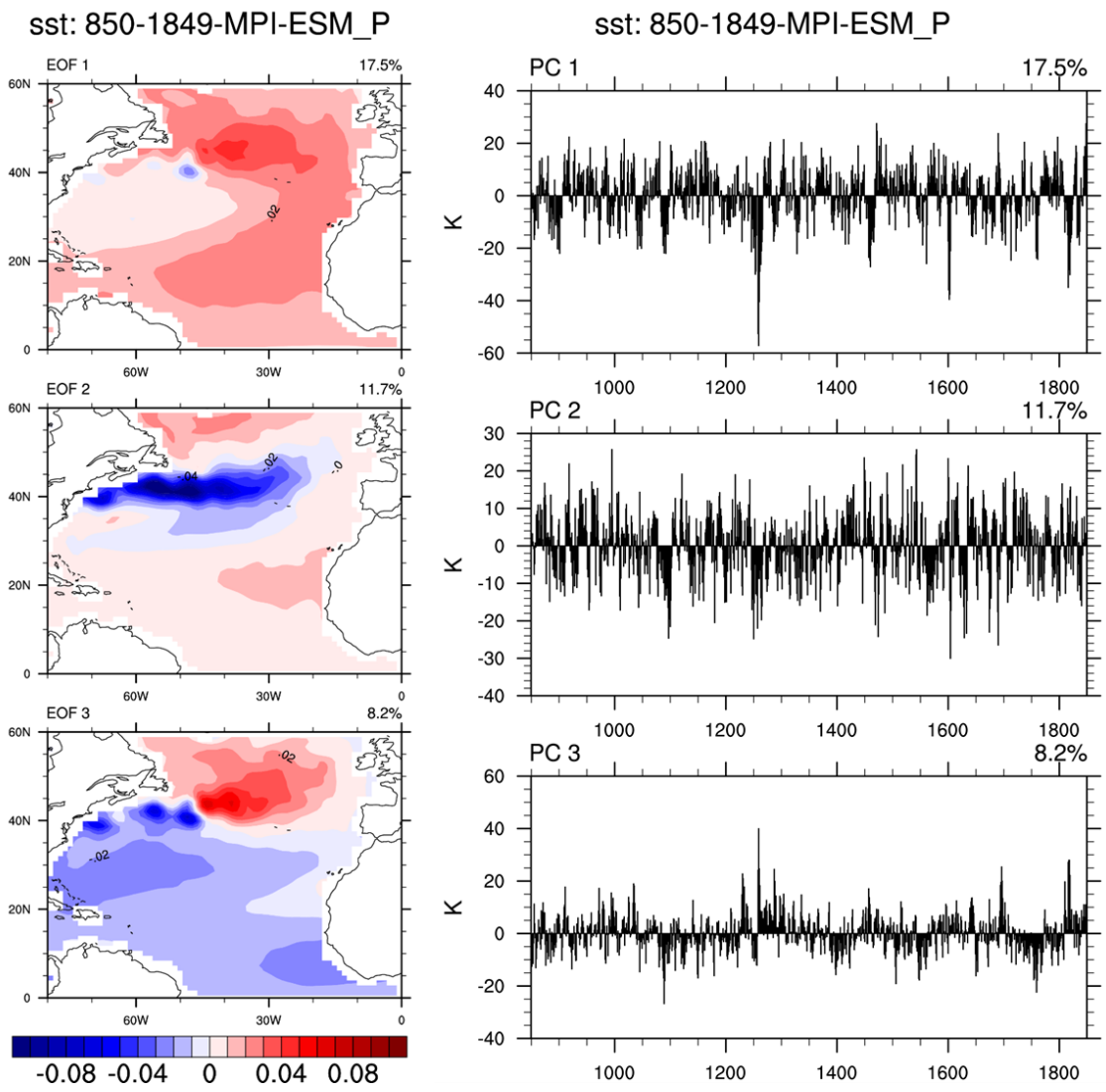

Figure 5-13. (Left) Spatial pattern and (Right) PC time series of the three leading EOFs of North Atlantic SST in the region of (0°-60°N, 0°-80°W), derived from the past millennium simulation outputs (850-1849) of model MPI-ESM-P.

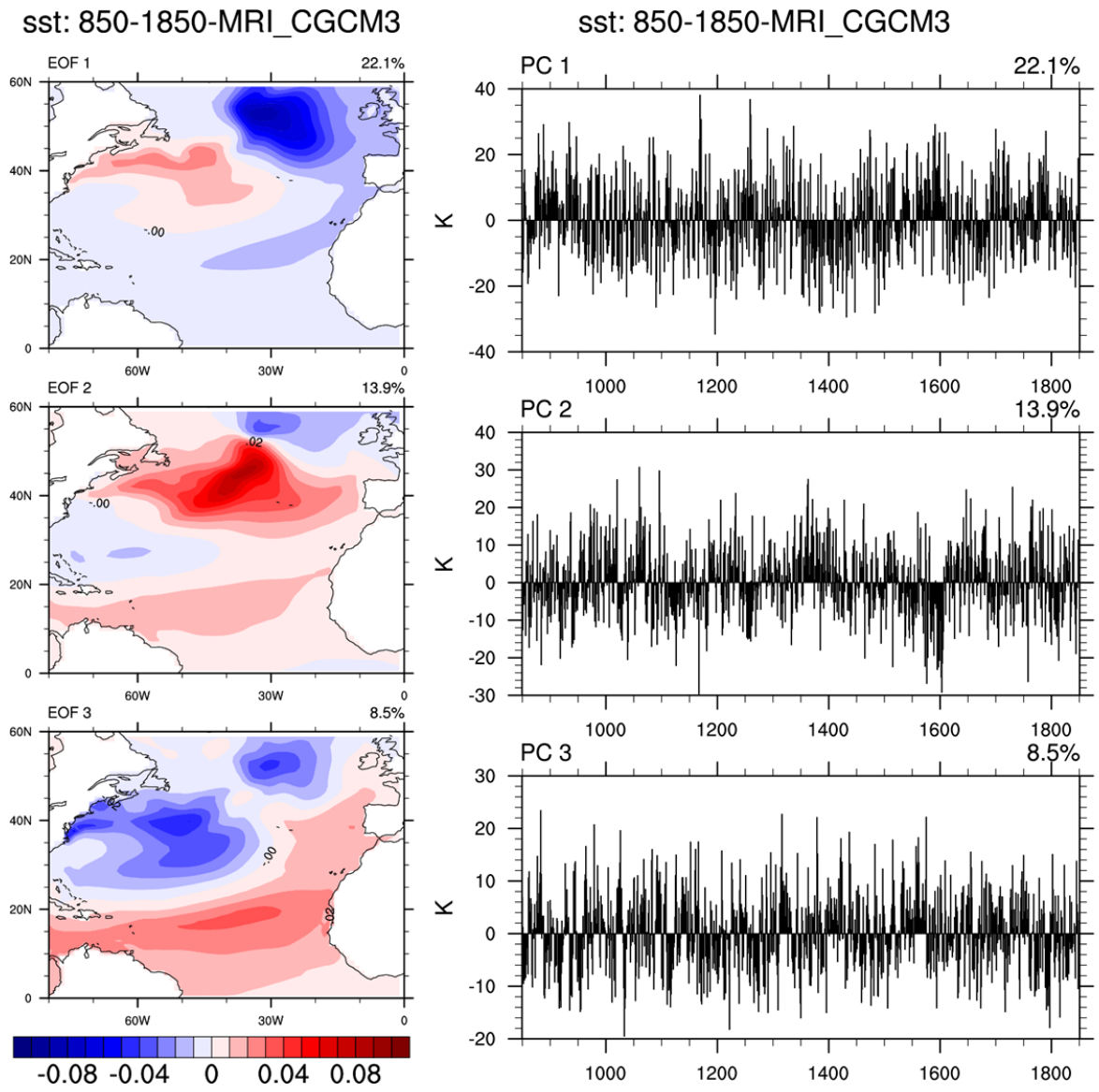

Figure 5-14. (Left) Spatial pattern and (Right) PC time series of the three leading EOFs of North Atlantic SST in the region of (0°-60°N, 0°-80°W), derived from the past millennium simulation outputs (850-1850) of model MRI-CGCM3

The wavelet analyses of the AMO index (PC 1 time series) from the last millennium simulations of the two models also show this difference in the stationarity of multidecadal variabilities. Wavelet analysis of CCSM4 displays a primary peak of variance around AD 1200 at 20-100 year periodicities (Fig. 5-15, bottom), but the variance at these multidecadal periodicities disappears before AD 1100. The same analysis of the PC 1 time series from MPI-ESM-P shows a more persistent active multidecadal variability throughout the 1000 years, with the same largest peak near 1200 (Fig. 5-16, bottom). Both of the two model simulations three AMO variance peaks, near AD 1200, AD 1400, and AD 1800, respectively. These peaks are concurrent with the reconstructed occurrence of major tropical strong volcanic eruptions (SVEs) [*Crowley*, 2000].

In *Zanchettin et al.*, 2013, unforced, naturally-forced, and anthropogenically-forced experiments of simulating multidecadal-to-centennial SST variability are performed, using MPI-ESM-P model for the last millennium. Among other conclusions, they found that bidecadal and near-centennial North Atlantic SST variabilities are sensitive to natural forcing, especially to SVEs. During periods dominated by external forcing, the AMO simulation among ensemble members are more coherent.

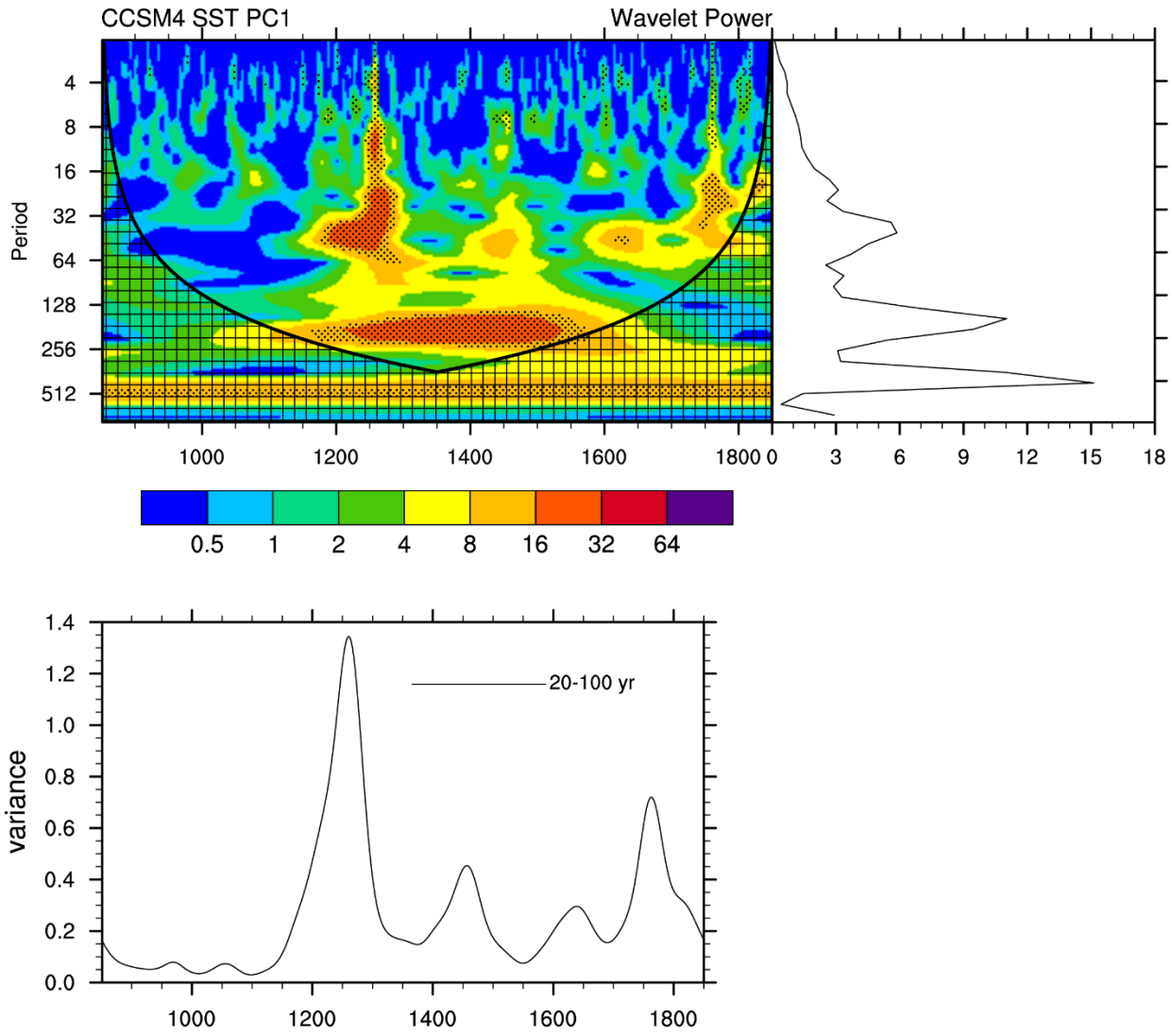

Figure 5-15. Same as Fig. 4-1 except using the PC1 of North Atlantic SST from the past millennium simulation outputs (850-1850) of model CCSM4

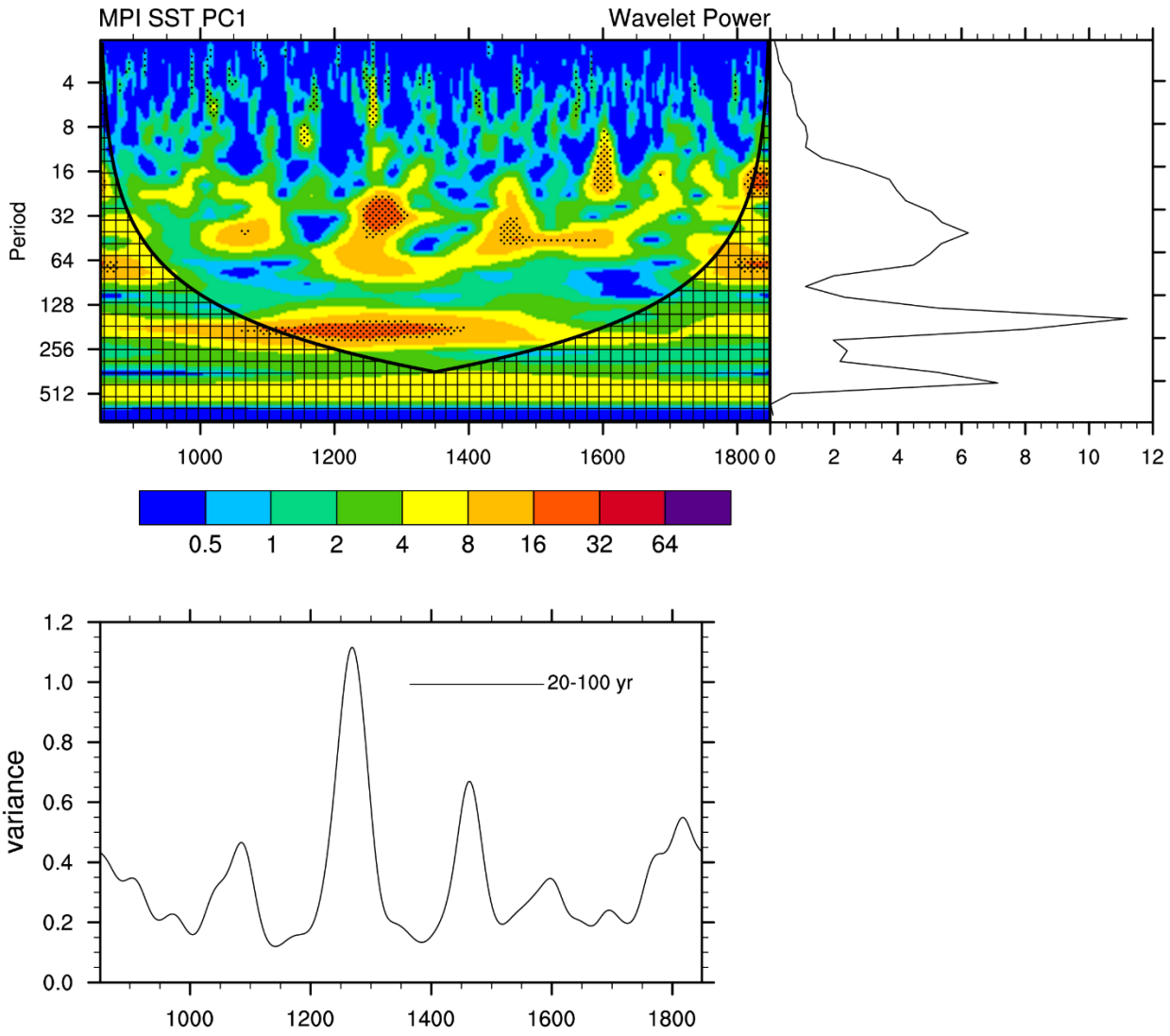

Figure 5-16. Same as Fig. 4-1 except using the PC1 of North Atlantic SST from the past millennium simulation outputs (850-1850) of model MPI-ESM-P

The regression maps derived from MPI-ESM-P past millennium simulation data are given in Fig. 5-17. All the variables used in Fig. 5-24b are filtered by a 50-100 year Lanczos band pass filter. The regression coefficients of annual North Atlantic SST, SLP and near-surface wind on the North Atlantic SST PC1 (Fig. 5-17a) display similar patterns as in reanalysis during the past century (as in Fig. 5-7a). However, the spatial patterns of the regression derived from filtered data can only indicate that simulated negative AMO index corresponds to cold North Atlantic SST.

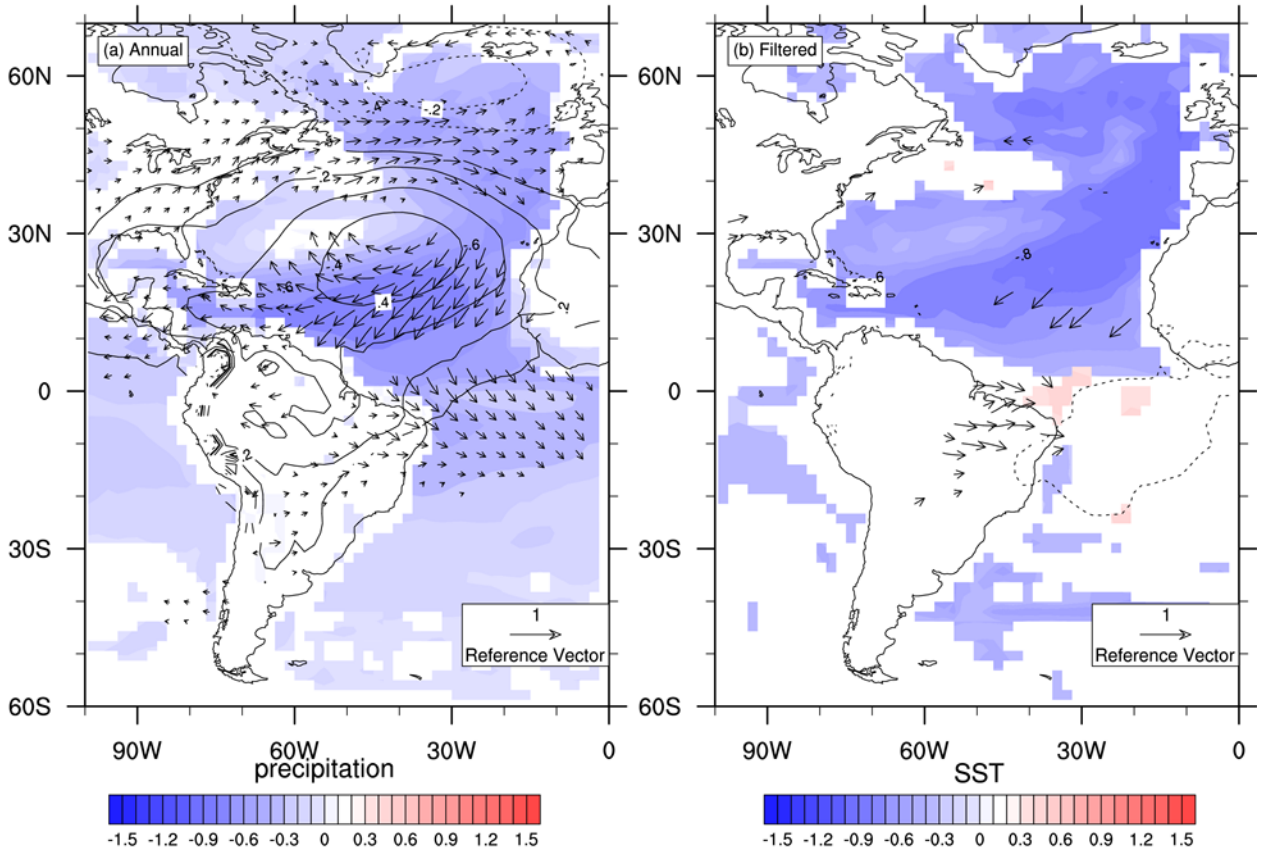

Figure 5-17. MPI-ESM-P past millennium simulation (850-1849) derived de-trended standardized (a) annual mean precipitation (color shades over land), SST (color shades over ocean), Sea level pressure (contours over ocean), and Surface wind (vectors) regression coefficients against de-trended standardized PC1 of North Atlantic SST; (b) the same as (a) except using 50-100 year band pass filtered data.

As in Chapter 3, we also regress the JAS season variables on this PCA-based AMO index (Fig. 5-18). Comparing Fig. 5-18a with Fig. 3-4b and Fig. 5-18b with Fig. 3-8b, we found that the regression patterns derived from both of the unsmoothed and filtered data indicate that in JAS season, colder SSTs associate with higher Azores High pressure and stronger easterly trade winds at tropical North Atlantic Ocean.

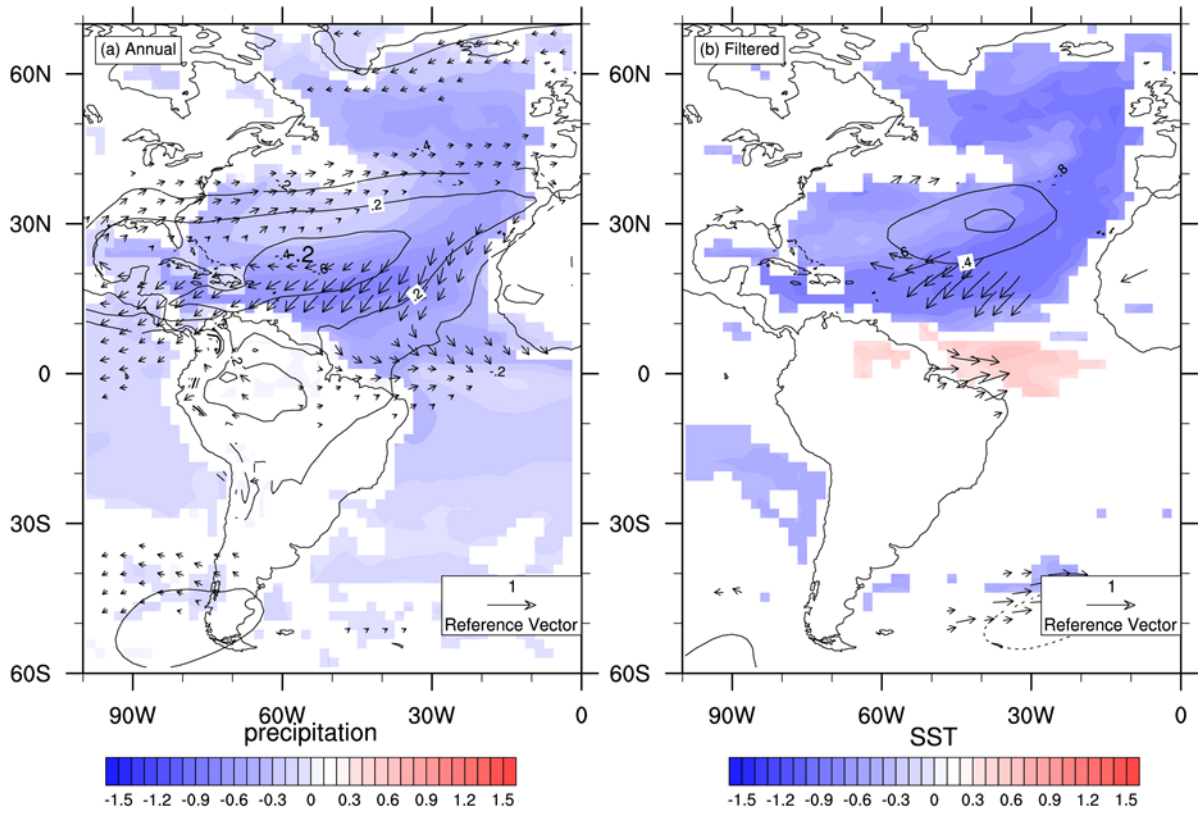

Figure 5-18. the same as Figure 5-17 except for using JAS mean data instead of annual mean.

The variability of AMO has important impacts on low latitude circum-Atlantic climate in summer/fall season. One of the examples is that it can influence summer/fall Sahel rainfall, at multidecadal timescales. Cold AMO phase is associated with reduced summer/fall Sahel rainfall and increased atmospheric dust. And the trade wind can bring the positive anomaly of dust

across tropical Atlantic, which can also influence Atlantic SST by altering the radiation factors. CMIP5 model performance in simulating this AMV-Sahel rainfall teleconnection is also evaluated in a previous study [*Martin and Thorncroft*, 2014]. However, the relationship between AMV and Sahel rainfall is not well simulated in MPI-ESM-P.

5.3. Discussion of a model SST projected *Globigerina bulloides* index

Considering the *G. bulloides*-North Atlantic SST relationship established in the observation, we would like to see how much of the variance of *G. bulloides* abundance in the past can be explained by a *G. bulloides* abundance index projected from MPI-ESM-P North Atlantic SST field based on this relationship. We applied a stepwise regression model in *Kim et al.* [2014] to do the projection, which is detailed as follows.

Firstly, we consider *G. bulloides* abundance as the predictand ($Gb(t)$) and North Atlantic SST as the predictor ($SST(x,t)$). The spatial grids are denoted as x, and the temporal points are indicated by t. During the training period (K), 1900 to 1990, the covariance pattern $Cov(x)$ between *G. bulloides* abundance and reanalysis North Atlantic SST field in a domain D is calculated as:

$$Cov(x) = \frac{1}{K}\sum_{t}^{K} Gb(t)SST(x,t). \qquad (5.1)$$

The domain D is defined by the grids (x) on which the correlation between the $SST(x,t)$ and $Gb(t)$ are significant over the training period.

Then, the predictor field $SST(x,t)$ is projected onto the covariance pattern to get a time series P(t):

$$\mathrm{P(t)} = \sum_{x}^{D} Cov(x)SST(x,t). \qquad (5.2)$$

The regression coefficient α is computed during the training period (K), based on the time series P(t) and the predictand $Gb(t)$:

$$\alpha = \frac{\sum_t^K Gb(t)P(t)}{\sum_t^K P(t)^2}. \qquad (5.3)$$

To use cross-validation to compute an approximation to the variance of the residual term ε in the model, $Gb(t) \sim \alpha P(t) + \epsilon$, we do the leave-one-out validation on the 91-year training sets $Gb(t)$. In detail, for each i from 1 to N (N = 91 in our training data), compute the corresponding α and $P(t)$, denoted by α_i and $P_i(t)$, as in (5.2) and (5.3), using the values of $Gb(t)$ and $SST(x,t)$ for $t \neq t_i$. Then the prediction of $Gb(t_i)$ is given by $\alpha_i P_i(t_i)$. The correlation between the series $Gb(t)$ and the predictions is as high as 0.63.

Our estimate of the expected variance of the residual is given by

$$MSE = \frac{1}{N}\sum_{i=1}^{N}[Gb(t_i) - \alpha_i P_i(t_i)]^2 . \qquad (5.4)$$

MSE is computed to be 87946.87. As the variance of the series $Gb(t)$ is 146470.2, the fraction of variance unexplained is 0.6.

Then, by projecting the predictor field $SST(x, t_f)$ in the simulation period t_f (850-1849 for last millennium simulation, 1861-2005 for historical simulation) onto the covariance pattern obtained from the training period ($Cov(x)$), predicted value $P(t_f)$ is derived as:

$$\mathrm{P}(t_f) = \sum_{x}^{D} Cov(x) SST\big(x, t_f\big). \qquad (5.5)$$

By multiplying the predicted time series $P(t_f)$ by the regression coefficient α, the predicted anomalous abundance of *G. bulloides* during the simulation period $Gb(t_f)$ can be calculated as:

$$\mathrm{Gb}\big(t_f\big) = \alpha \mathrm{P}(t_f). \qquad (5.6)$$

Finally, the average abundance of *G. bulloides* over the training period is added to the anomaly to obtain the projected index.

This projected index using the MPI-ESM-P historical simulation of SST is shown in Fig. 5-19, together with the *G. bulloides* abundance data during 1900-1990, the same time span as the training period. During this time period, the variance of the projected index is 36423, and the variance of *G. bulloides* abundance data is 146470. The fraction of variance unexplained by the index is 0.75.

And the projected index using MPI-ESM-P last millennium simulation SST is displayed in Fig. 5-20 with *G. bulloides* abundance data during 1165-1849. During this time period, the variance of the projected index is 53645.7, and the variance of *G. bulloides* abundance data is 210986. The fraction of variance unexplained by the index is also 0.75.

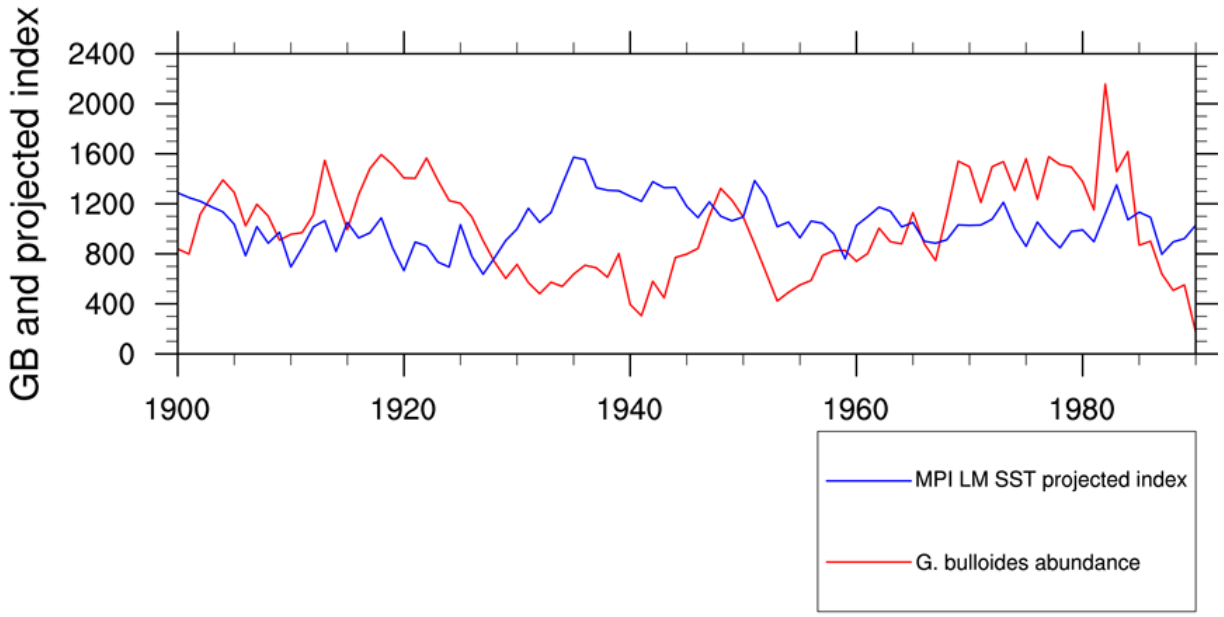

Figure 5-19. Comparison of G. bulloides abundance data (red) and the index projected from MPI-ESM-P historical simulation of SST (blue) during 1900-1990.

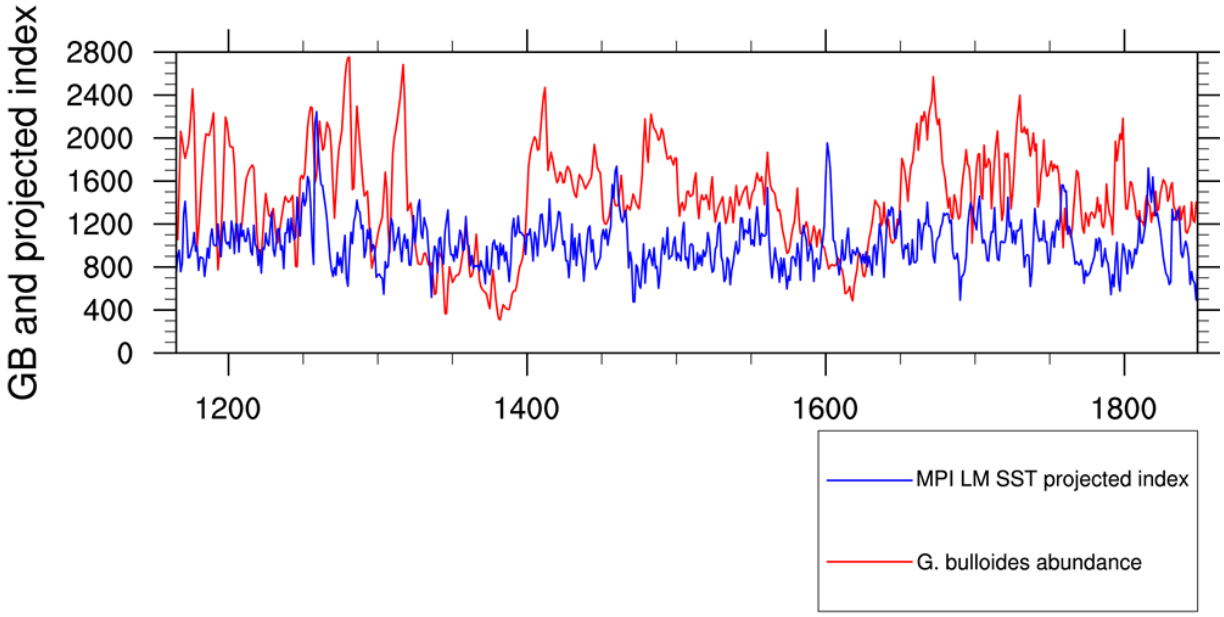

Figure 5-20. Comparison of G. bulloides abundance data (red) and the index projected from MPI-ESM-P last millennium simulation of SST (blue) during 1165-1850.

The regression model has a fraction of variance unexplained (FVU) of 0.6, using training set of data in the cross-validation. The projected *G. bulloides* abundance index captured about one fourth of the variance of the *G. bulloides* abundance data, using historical simulation or last millennium simulation SST from MPI-ESM-P model. In previous study, the discrepancies in SST variability between General circulation model simulations and proxy data are found to be large [*Laepple and Huybers,* 2014]. When we use the last millennium simulation data as test data, we should be aware of possible variance reduction due to model's potential underestimation of paleoclimate SST. However, in this calculation, the unexplained fraction of variance does not increase as the length of test data extends back from about a hundred years to a thousand years long. In this case, maybe the smoothing by the regression model plays the primary role in the variance difference between projected index and the paleoclimate data, while the model-proxy data difference does not influence the result too much.

5.4. Summary

Among the five models in comparison, the MPI-ESM-P and CCSM4 historical simulations can better capture the AMO-like leading EOF of North Atlantic SST. The EOF analysis of SST and SLP from the past millennium simulations of each model gives similar patterns as its counterpart from the historical run. MPI-ESM-P simulates rather stationary AMV during the past 1000 years. It also simulates similar relationship between summer/fall North Atlantic SST, Azores High pressure, and trade wind as what is observed during the recent century.

Chapter 6. Conclusion and Discussion

6.1. Conclusions

In this research, we used the reanalysis data, paleoclimate proxies, and model simulation outputs to study the Atlantic multidecadal variabilities (AMV) in the past millennium. Cariaco Basin *G. bulloides* abundance data is the focus in the study, due to its high temporal resolution, geographic location, marine-based data source, and evident covariation with the North Atlantic SST multidecadal variability in the past century. We suspected that it contains the AMV signal, and tested this hypothesis with observation, reanalysis and other paleoclimate data.

The relationship of the *G. bulloides* abundance data with Atlantic climate variability in the past century is established based on the instrumental observation and reanalysis. The interannual and multidecadal variations of Cariaco Basin *G. bulloides* are both associated with lower North Atlantic SST, higher subtropical pressure, stronger tropical North Atlantic easterly zonal wind, and reduced Sahel rainfall. This relationship is shown to be robust during the summer/fall seasons also, which establishes a connection between Cariaco Basin *G. bulloides* abundance data and Sahel summer/fall precipitation. Moreover, the seasonal analysis also provides a possibility to compare this data with proxies reflecting summer/fall climate variabilities.

The AMO index has association with the Cariaco Basin *G. bulloides* abundance data. Other than enhanced upwelling at Cariaco Basin, the cold phase of AMO is also related to more

Sahel dust and stronger low level easterly wind across the tropical North Atlantic. The easterly wind can bring the anomalous dust to Cariaco Basin sea surface and contribute to the *G. bulloides* production boost. Considering the relationship established between the AMO and Cariaco Basin *G. bulloides* abundance data using observation and reanalysis data, we consider that this paleoclimate data is able to reflect the AMO in the past century.

Putting the *G. bulloides* abundance data in the context of other North Atlantic paleoclimate data sets, we found that its multidecadal variations is consistent with the SST reconstruction at Eastern Tropical Atlantic [*Kuhnert and Mulitza*, 2011] and Puerto Rico [*Kilbourne et al.*, 2008], at the same timescales. In addition, multidecadal variability of *G. bulloides* abundance has a same-sign relationship with NAO reconstructions that are based on Bermuda [*Goodkin et al.*, 2008a] and based on northeastern North Atlantic to Europe [*Luterbacher*, 2002] at the same multidecadal timescales. These results attest that AMV exists before industrialized era, rather than being anthropogenic forced. They also indicate that multidecadal *G. bulloides* abundance can reflect the AMO during its whole time span.

Five CMIP5 models are compared in simulating the AMV in the past century, based on the relationship established with reanalysis data. MPI-ESM-P stands out in the comparison with better performance in capturing the AMO-like pattern of North Atlantic SST variability. As the Atlantic multidecadal variability is found to exist before instrumental period, we also compared the past millennium simulations (850-1850) of the CMIP5 models. MPI-ESM-P simulates AMV throughout most of the past 1000 years, as well as observed relationship between summer/fall North Atlantic SST, Azores High pressure, and trade wind during the past century.

6.2. Discussion and future work

This study is mainly focused on AMV at low-latitude during the past millennium. As we were establishing the relationship between the AMV with the paleoclimate data, as well as with other climate variabilities, we confined the study area to Atlantic Ocean. This choice is valid in this study as our goal is to find out the spatial characteristics of the low-latitude AMV. However, as we proceed to in-depth study of the mechanisms, global perspective is need. In the next step, we plan to firstly examine the connection between AMV and another two important oceanic climate variabilities, the Pacific Decadal Oscillation (PDO) and El Niño-Southern Oscillation (ENSO). And we will also expand our paleoclimate data comparison accordingly, both in terms of locations and variables. A more comprehensive picture of the past North Atlantic climate variability should be formed in the context of the global climate change.

As for the model evaluation, the intercomparison work is aimed at finding out a model that is able to capture the AMV. In the short periods, such as in the last century, de-trending is considered to be enough to remove the external forcing. However, other methods should be applied to differentiate the internal variability from the external forcing in longer time series. Currently, we are using moving-block bootstrapping to sample short time periods to compare the piece-wise variabilities. But a better approach could be to include a long pre-industrial control experiment in the comparison. This will be done in the future study. After we include more models in the comparison and find a best performed one in simulating the AMV, we would also like to use it to study the mechanisms of the AMV by executing proper experiments.

Reference

Anand, P., H. Elderfield, and M. H. Conte (2003), Calibration of Mg/Ca thermometry in planktonic foraminifera from a sediment trap time series, *Paleoceanography*, *18*(2), 1050 2002PA000846, doi:10.1029/2002PA000846.

Appenzeller, C., T. F. Stocker, and M. Anklin (1998), North Atlantic oscillation dynamics recorded in Greenland ice cores, *Science (80-.).*, *282*(5388), 446–449, doi:10.1126/science.282.5388.446.

Bao, Q. et al. (2013), The Flexible Global Ocean-Atmosphere-Land system model, Spectral Version 2: FGOALS-s2, *Adv. Atmos. Sci.*, *30*(3), 561–576, doi:10.1007/s00376-012-2113-9.

Black, D. E., L. C. Peterson, J. T. Overpeck, A. Kaplan, M. E. Evans, and M. Kashgarian (1999), Eight Centuries of North Atlantic Ocean Atmosphere Variability, *Science (80-.).*, *286*(5445), 1709–1713, doi:10.1126/science.286.5445.1709.

Black, D. E., M. A. Abahazi, R. C. Thunell, A. Kaplan, E. J. Tappa, and L. C. Peterson (2007), An 8-century tropical Atlantic SST record from the Cariaco Basin: Baseline variability, twentieth-century warming, and Atlantic hurricane frequency, *Paleoceanography*, *22*(4), doi:10.1029/2007PA001427.

Chiang, J. C. H., Y. Kushnir, and A. Giannini (2002), Deconstructing Atlantic Intertropical Convergence Zone variability : Influence of the local cross-equatorial sea surface temperature gradient and remote forcing from the eastern equatorial Pacific, *J. Geophys. Res.*, *107*(D1), 4004, doi:10.1029/2000JD000307.

Compo, G. P. et al. (2011), The Twentieth Century Reanalysis Project, *Q. J. R. Meteorol. Soc.*, *137*(654), 1–28, doi:10.1002/qj.776.

Cook, E. R., R. D. DArrigo, and K. R. Briffa (1998), A reconstruction of the North Atlantic Oscillation using tree-ring chronologies from North Americ and Europe, *The Holocene*, *8*, 9–17, doi:10.1191/095968398677793725.

Cook, E. R., R. D. D'Arrigo, and M. E. Mann (2002), A well-verified, multiproxy reconstruction of the winter North Atlantic Oscillation index since A.D. 1400, *J. Clim.*, *15*(13), 1754–1764, doi:Article.

Crowley, T. J. (2000), Causes of climate change over the past 1000 years, *Science (80-.).*, *289*(5477), 270–277, doi:10.1126/science.289.5477.270.

Cullen, H. M., R. D. D'Arrigo, E. R. Cook, and M. E. Mann (2001), Multiproxy reconstructions of the North Atlantic oscillation, *Paleoceanography*, *16*(1), 27–39, doi:10.1029/1999PA000434.

Delworth, T. L., and M. E. Mann (2000), Observed and simulated multidecadal variability in the Northern Hemisphere, *Clim. Dyn.*, *16*(9), 661–676, doi:10.1007/s003820000075.

Duchon, C. E. (1979), Lanczos Filtering in One and Two Dimensions, *J. Appl. Meteorol.*, *18*(8), 1016–1022, doi:10.1175/1520-0450(1979)018<1016:LFIOAT>2.0.CO;2.

Eden, C., and T. Jung (2001), North Atlantic interdecadal variability: Oceanic response to the

North Atlantic oscillation (1865-1997), *J. Clim.*, *14*(5), 676–691, doi:10.1175/1520-0442(2001)014<0676:NAIVOR>2.0.CO;2.

Eden, C., and J. Willebrand (2001), Mechanism of interannual to decadal variability of the North Atlantic circulation, *J. Clim.*, *14*(10), 2266–2280, doi:10.1175/1520-0442(2001)014<2266:MOITDV>2.0.CO;2.

Enfield, D. B., A. M. Mestas-Nuñez, and P. J. Trimble (2001), The Atlantic multidecadal oscillation and its relation to rainfall and river flows in the continental U.S, *Geophys. Res. Lett.*, *28*(10), 2077–2080, doi:10.1029/2000GL012745.

Gent, P. R. et al. (2011), The community climate system model version 4, *J. Clim.*, *24*(19), 4973–4991, doi:10.1175/2011JCLI4083.1.

Giorgetta, M. A. et al. (2013), Climate and carbon cycle changes from 1850 to 2100 in MPI-ESM simulations for the coupled model intercomparison project phase 5, *J. Adv. Model. Earth Syst.*, *5*(3), 572–597, doi:10.1002/jame.20038.

Glueck, M. F., and C. W. Stockton (2001), Reconstruction of the North Atlantic Oscillation, 1429-1983, *Int. J. Climatol.*, *21*(12), 1453–1465, doi:10.1002/joc.684.

Goodkin, N. F., K. A. Hughen, A. L. Cohen, and S. R. Smith (2005), Record of Little Ice Age sea surface temperatures at Bermuda using a growth-dependent calibration of coral Sr/Ca, *Paleoceanography*, *20*(4), 1–9, doi:10.1029/2005PA001140.

Goodkin, N. F., K. a. Hughen, S. C. Doney, and W. B. Curry (2008a), Increased multidecadal variability of the North Atlantic Oscillation since 1781, *Nat. Geosci.*, *1*(12), 844–848, doi:10.1038/ngeo352.

Goodkin, N. F., K. A. Hughen, W. B. Curry, S. C. Doney, and D. R. Ostermann (2008b), Sea surface temperature and salinity variability at Bermuda during the end of the Little Ice Age, *Paleoceanography*, *23*(3), 1–13, doi:10.1029/2007PA001532.

Gray, S. T., L. J. Graumlich, J. L. Betancourt, and G. T. Pederson (2004), A tree-ring based reconstruction of the Atlantic Multidecadal Oscillation since 1567 A.D, *Geophys. Res. Lett.*, *31*(12), 2–5, doi:10.1029/2004GL019932.

Hameed, S., and N. Riemer (2012), Relationship of sahel precipitation and atmospheric centers of action, *Adv. Meteorol.*, *2012*, doi:10.1155/2012/953853.

Haug, G. H. (2001), Southward Migration of the Intertropical Convergence Zone Through the Holocene, *Science (80-.).*, *293*(5533), 1304–1308, doi:10.1126/science.1059725.

Haug, G. H., K. a Hughen, D. M. Sigman, L. C. Peterson, and U. Röhl (2001), Southward migration of the intertropical convergence zone through the Holocene., *Science*, *293*(5533), 1304–1308, doi:10.1126/science.1059725.

Haug, G. H. et al. (2003), Climate and the collapse of Maya civilization., *Science*, *299*(5613), 1731–5, doi:10.1126/science.1080444.

Hughen, K., J. Southon, S. Lehman, C. Bertrand, and J. Turnbull (2006), Marine-derived 14C calibration and activity record for the past 50,000 years updated from the Cariaco Basin, *Quat. Sci. Rev.*, *25*(23-24), 3216–3227, doi:10.1016/j.quascirev.2006.03.014.

Hurrell, J. W. (1995), Decadal trends in the north atlantic oscillation: regional temperatures and

precipitation., *Science*, *269*(5224), 676–9, doi:10.1126/science.269.5224.676.

Jones, P. D. et al. (1999), Monthly mean pressure reconstructions for Europe for the 1780-1995 period, *Int. J. Climatol.*, *19*(4), 347–364, doi:10.1002/(SICI)1097-0088(19990330)19:4<347::AID-JOC363>3.0.CO;2-S.

Kennett, D. J. et al. (2012a), Development and disintegration of Maya political systems in response to climate change., *Science*, *338*(6108), 788–91, doi:10.1126/science.1226299.

Kennett, D. J. et al. (2012b), Development and disintegration of Maya political systems in response to climate change., *Science*, *338*(November), 788, doi:10.1126/science.1226299.

Kilbourne, K. H., T. M. Quinn, R. Webb, T. Guilderson, J. Nyberg, and A. Winter (2008), Paleoclimate proxy perspective on Caribbean climate since the year 1751: Evidence of cooler temperatures and multidecadal variability, *Paleoceanography*, *23*(3), 1–14, doi:10.1029/2008PA001598.

Kim, H.-M., E. K. M. Chang, and M. Zhang (2014), Statistical-dynamical seasonal forecast for tropical cyclones affecting New York State, *Weather Forecast.*, 141230123738002, doi:10.1175/WAF-D-14-00089.1.

Knight, J. R., R. J. Allan, C. K. Folland, M. Vellinga, and M. E. Mann (2005), A signature of persistent natural thermohaline circulation cycles in observed climate, *Geophys. Res. Lett.*, *32*(20), 1–4, doi:10.1029/2005GL024233.

Knight, J. R., C. K. Folland, and A. A. Scaife (2006), Climate impacts of the Atlantic multidecadal oscillation, *Geophys. Res. Lett.*, *33*(17), doi:10.1029/2006GL026242.

Kobayashi, S. et al. (2015), The JRA-55 Reanalysis: General Specifications and Basic Characteristics, *J. Meteorol. Soc. Japan. Ser. II*, *93*(1), 5–48, doi:10.2151/jmsj.2015-001.

Kuhnert, H., and S. Mulitza (2011), Multidecadal variability and late medieval cooling of near-coastal sea surface temperatures in the eastern tropical North Atlantic, *Paleoceanography*, *26*(4), 1–11, doi:10.1029/2011PA002130.

Kuhnert, H., T. Crüger, and J. Pätzold (2005), NAO signature in a Bermuda coral Sr/Ca record, *Geochemistry, Geophys. Geosystems*, *6*(4), doi:10.1029/2004GC000786.

Laepple, T., and P. Huybers (2014), Ocean surface temperature variability: large model-data differences at decadal and longer periods., *Proc. Natl. Acad. Sci. U. S. A.*, *111*(47), 16682–16687, doi:10.1073/pnas.1412077111.

Landrum, L., B. L. Otto-Bliesner, E. R. Wahl, A. Conley, P. J. Lawrence, N. Rosenbloom, and H. Teng (2013), Last millennium climate and its variability in CCSM4, *J. Clim.*, *26*(4), 1085–1111, doi:10.1175/JCLI-D-11-00326.1.

Latif, M., M. Collins, H. Pohlmann, and N. Keenlyside (2006a), A review of predictability studies of Atlantic sector climate on decadal time scales, *J. Clim.*, *19*(23), 5971–5987, doi:10.1175/JCLI3945.1.

Latif, M., C. B??ning, J. Willebrand, A. Biastoch, J. Dengg, N. Keenlyside, U. Schwecjendiek, and G. Madec (2006b), Is the thermohaline circulation changing?, *J. Clim.*, *19*(18), 4631–4637, doi:10.1175/JCLI3876.1.

Lee, S. K., and C. Wang (2010), Delayed advective oscillation of the Atlantic thermohaline

circulation, *J. Clim.*, *23*(5), 1254–1261, doi:10.1175/2009JCLI3339.1.

Li, J., C. Sun, and F. F. Jin (2013), NAO implicated as a predictor of Northern Hemisphere mean temperature multidecadal variability, *Geophys. Res. Lett.*, *40*(20), 5497–5502, doi:10.1002/2013GL057877.

Luterbacher, J., E. Xoplaki, D. Dietrich, R. Rickli, J. Jacobeit, C. Beck, D. Gyalistras, C. Schmutz, and H. Wanner (2002), Reconstruction of sea level pressure fields over the Eastern North Atlantic and Europe back to 1500, *Clim. Dyn.*, *18*(7), 545–561, doi:10.1007/s00382-001-0196-6.

Luterbacher, J. et al. (2002), Extending North Atlantic Oscillation reconstructions back to 1500, *Atmos. Sci. Lett.*, *2*(1-4), 114–124, doi:10.1006/asle.2001.0044.

Marshall, J. (2001), North Atlantic Climate Variability : Phenomena , Impacts and Mechanisms, , *1898*, 1863–1898.

Martin, E. R., and C. D. Thorncroft (2014), The impact of the AMO on the West African monsoon annual cycle, *Q. J. R. Meteorol. Soc.*, *140*(678), 31–46, doi:10.1002/qj.2107.

Martin, E. R., C. Thorncroft, and B. B. B. Booth (2014), The multidecadal atlantic SST-sahel rainfall teleconnection in CMIP5 simulations, *J. Clim.*, *27*(2), 784–806, doi:10.1175/JCLI-D-13-00242.1.

Martinez, N. C., R. W. Murray, R. C. Thunell, L. C. Peterson, F. Muller-Karger, Y. Astor, and R. Varela (2007), Modern climate forcing of terrigenous deposition in the tropics (Cariaco Basin, Venezuela), *Earth Planet. Sci. Lett.*, *264*(3-4), 438–451, doi:10.1016/j.epsl.2007.10.002.

Miettinen, A., D. Divine, N. Kocx, F. Godtliebsen, and I. R. Hall (2012), Multicentennial variability of the sea surface temperature gradient across the subpolar North Atlantic over the last 2.8 kyr, *J. Clim.*, *25*(12), 4205–4219, doi:10.1175/JCLI-D-11-00581.1.

Mulitza, S. et al. (2010), Increase in African dust flux at the onset of commercial agriculture in the Sahel region, *Nature*, *466*(7303), 226–228, doi:10.1038/nature09213.

Nye, J. A., M. R. Baker, R. Bell, A. Kenny, K. H. Kilbourne, K. D. Friedland, E. Martino, M. M. Stachura, K. S. Van Houtan, and R. Wood (2014), Ecosystem effects of the Atlantic Multidecadal Oscillation, *J. Mar. Syst.*, *133*, 103–116, doi:10.1016/j.jmarsys.2013.02.006.

Peings, Y., and G. Magnusdottir (2014), Forcing of the wintertime atmospheric circulation by the multidecadal fluctuations of the North Atlantic ocean, *Environ. Res. Lett.*, *9*(3), 034018, doi:10.1088/1748-9326/9/3/034018.

Peterson, L. C., J. T. Overpeck, N. G. Kipp, and J. Imbrie (1991), A high-resolution Late Quaternary upwelling record from the anoxic Cariaco Basin, Venezuela, *Paleoceanography*, *6*(1), 99, doi:10.1029/90PA02497.

Peterson, L. C., G. H. Haug, K. A. Hughen, and U. Röhl (2000), Rapid changes in the hydrologica cycle of the Tropical Atlantic during the Last Glacial, *Science (80-.).*, *290*(8 December), 1947–1951.

Proctor, C. J., a. Baker, W. L. Barnes, and M. a. Gilmour (2000), A thousand year speleothem proxy record of North Atlantic climate from Scotland, *Clim. Dyn.*, *16*(10-11), 815–820,

doi:10.1007/s003820000077.

Prospero, J. M., and P. J. Lamb (2003), African droughts and dust transport to the Caribbean: climate change implications., *Science*, *302*(5647), 1024–1027, doi:10.1126/science.1089915.

Rayner, N. A., D. E. Parker, E. B. Horton, C. K. Folland, L. V. Alexander, D. P. Rowell, E. C. Kent, and A. Kaplan (2003), Global analyses of sea surface temperature, sea ice, and night marine air temperature since the late nineteenth century, *J. Geophys. Res.*, *108*(D14), 4407, doi:10.1029/2002JD002670.

Robertson, A. W., C. R. Mechoso, and Y.-J. Kim (2000), The Influence of Atlantic Sea Surface Temperature Anomalies on the North Atlantic Oscillation*, *J. Clim.*, *13*(1), 122–138, doi:10.1175/1520-0442(2000)013<0122:TIOASS>2.0.CO;2.

Rodrigo, F. S., D. Pozo-Vázquez, M. J. Esteban-Parra, and Y. Castro-Díez (2001), A reconstruction of the winter North Atlantic Oscillation index back to A.D. 1501 using documentary data in southern Spain, *J. Geophys. Res.*, *106*(D14), 14805, doi:10.1029/2000JD900728.

Rodwell, M. J., D. P. Rowell, and C. K. Folland (1999), Oceanic forcing of the wintertime North Atlantic Oscillation and European climate, *Nature*, *398*(6725), 320–323, doi:10.1038/18648.

Rohling, E. J. (2007), Progress in paleosalinity: Overview and presentation of a new approach, *Paleoceanography*, *22*(3), doi:10.1029/2007PA001437.

Schlesinger, M. E., and N. Ramankutty (1994), An oscillation in the global climate system of period 65–70 years, *Nature*, *367*(6465), 723–726, doi:10.1038/367723a0.

Stuiver, M., P. J. Reimer, E. Bard, J. W. Beck, G. S. Burr, K. A. Hughen, B. Kromer, G. McCormac, J. Van Der Plicht, and M. Spurk (1998), INTCAL98 Radiocarbon Age Calibration, 24000-0 cal BP, *Radiocarbon*, *40*(3), 1041–1083, doi:10.2458/azu_js_rc.40.3781.

Sun, C., J. Li, and F. F. Jin (2015), A delayed oscillator model for the quasi-periodic multidecadal variability of the NAO, *Clim. Dyn.*, *45*(7-8), 2083–2099, doi:10.1007/s00382-014-2459-z.

Sutton, R. T., and D. L. R. Hodson (2005), Atlantic Ocean forcing of North American and European summer climate, *Science (80-.).*, *309*(5731), 115–118, doi:10.1126/science.1109496.

Tedesco, K., R. Thunell, Y. Astor, and F. Muller-Karger (2007), The oxygen isotope composition of planktonic foraminifera from the Cariaco Basin, Venezuela: Seasonal and interannual variations, *Mar. Micropaleontol.*, *62*(3), 180–193, doi:10.1016/j.marmicro.2006.08.002.

Torrence, C., and G. P. Compo (1998), A Practical Guide to Wavelet Analysis, *Bull. Am. Meteorol. Soc.*, *79*(1), doi:10.1175/1520-0477(1998)079<0061:APGTWA>2.0.CO;2.

Wang, C., S. Dong, A. T. Evan, G. R. Foltz, and S. K. Lee (2012), Multidecadal covariability of north atlantic sea surface temperature, African dust, Sahel Rainfall, and Atlantic hurricanes, *J. Clim.*, *25*(15), 5404–5415, doi:10.1175/JCLI-D-11-00413.1.

Wu, T. et al. (2013), An overview of BCC climate system model development and application for climate change studies, *J. Meteorol. Res.*, *28*(1), 34–56.

Wurtzel, J. B., D. E. Black, R. C. Thunell, L. C. Peterson, E. J. Tappa, and S. Rahman (2013), Mechanisms of southern Caribbean SST variability over the last two millennia, *Geophys. Res. Lett.*, *40*(22), 5954–5958, doi:10.1002/2013GL058458.

Xie, S. P. (1999), A dynamic ocean-atmosphere model of the tropical Atlantic decadal variability, *J. Clim.*, *12*(1), 64–70, doi:10.1175/1520-0442-12.1.64.

Yarincik, K. M., R. W. Murray, T. W. Lyons, L. C. Peterson, and G. H. Haug (2000), Oxygenation history of bottom waters in the Cariaco Basin, Venezuela, over the past 578,000 years: Results from redox-sensitive metals (Mo, V, Mn, and Fe), *Paleoceanography*, *15*(6), 593–604, doi:10.1029/1999PA000401.

Yoon, J. H., and N. Zeng (2010), An Atlantic influence on Amazon rainfall, *Clim. Dyn.*, *34*(2), 249–264, doi:10.1007/s00382-009-0551-6.

Yukimoto, S. et al. (2012), A New Global Climate Model of the Meteorological Research Institute: MRI-CGCM3 -Model Description and Basic Performance-, *J. Meteorol. Soc. Japan*, *90A*, 23–64, doi:10.2151/jmsj.2012-A02.

Zanchettin, D., A. Rubino, D. Matei, O. Bothe, and J. H. Jungclaus (2013), Multidecadal-to-centennial SST variability in the MPI-ESM simulation ensemble for the last millennium, *Clim. Dyn.*, *40*(5-6), 1301–1318, doi:10.1007/s00382-012-1361-9.

Zhang, L., and C. Wang (2013), Multidecadal North Atlantic sea surface temperature and Atlantic meridional overturning circulation variability in CMIP5 historical simulations, *J. Geophys. Res. Ocean.*, *118*(10), 5772–5791, doi:10.1002/jgrc.20390.

Zhang, R. (2008), Coherent surface-subsurface fingerprint of the Atlantic meridional overturning circulation, *Geophys. Res. Lett.*, *35*(20), doi:10.1029/2008GL035463.

Zhang, R., and T. L. Delworth (2006), Impact of Atlantic multidecadal oscillations on India/Sahel rainfall and Atlantic hurricanes, *Geophys. Res. Lett.*, *33*(17), doi:10.1029/2006GL026267.

Zhang, R., and G. K. Vallis (2006), Impact of great salinity anomalies on the low-frequency variability of the North Atlantic climate, *J. Clim.*, *19*(3), 470–482, doi:10.1175/JCLI3623.1.